1-1-2006

A study of the interaction of a travelling shock wave with a solid-propellant rocket motor head end

Robert Elian Feteanu
Ryerson University

A STUDY OF THE INTERACTION OF A TRAVELLING SHOCK WAVE WITH A SOLID-PROPELLANT ROCKET MOTOR HEAD END

by

Robert Elian Feteanu,
B.Eng. (Aerospace Engineering),
Bucharest Politechnic University, 1999

A thesis
presented to Ryerson University
in partial fulfillment of the
requirements for the degree of
Master of Applied Science
in the program of
Mechanical Engineering

Toronto, Ontario, Canada, 2006

Author's declaration

I hereby declare that I am the sole author of this thesis.

I authorize Ryerson University to lend this thesis to other institutions or individuals for the purpose of scholarly research.

Robert Elian Feteanu

I further authorize Ryerson University to reproduce this thesis by photocopying or by other means, in total or in part, at the request of other institutions or individuals for the purpose of scholarly research.

Robert Elian Feteanu

Borrower's page

Ryerson University requires the signatures of all persons using or photocopying this thesis. Please sign below, and give address and date.

Name	Address	Date

Abstract

A STUDY OF THE INTERACTION OF A TRAVELLING SHOCK WAVE WITH A SOLID-PROPELLANT ROCKET MOTOR HEAD END

© Robert Elian Feteanu, 2006
Master of Applied Science
in the program of
Mechanical Engineering
Ryerson University

Experimental and numerical studies have been undertaken to examine various aspects pertaining to the interaction of an incident travelling shock wave with a solid rocket motor's head end (forward section), in order to identify any potential gasdynamic mechanism of wave reinforcement pertinent to combustion instability behaviour in these motors.

A cold-flow experiment, based on a shock tube scheme tailored to the present application, has proved to be useful in providing information surrounding the interaction process. Both experimental and numerical results (CFD simulations) confirm the existence of substantial transient radial wave development superimposed on the base reflected axial shock wave.

These results illustrate the potential weakness of one-dimensional flow models for certain engineering applications, where important multidimensional phenomena, such as those observed in this work, may not be captured. By analogy to actual propulsion system combustion chambers, the transverse wave activity is potentially a factor in supporting an augmentation of the local combustion rate in the head-end region of a rocket motor combustor.

Acknowledgements

I wish to express my sincere gratitude to Dr. David Greatrix (thesis supervisor) for his continuous guidance throughout my graduate studies. Patience and devotion shown by my supervisor towards helping me complete my thesis cannot be expressed in words. It was indeed a pleasure to work under his supervision.

Special thanks are owed to Jerry Karpynczyk for helping me in conducting various calibrations and experiments.

Financial aid in the form of a graduate stipend provided through the Natural Sciences and Engineering Research Council of Canada (NSERC) is acknowledged here with thanks.

Table of Contents

Nomenclature

Arabic

a	local gas speed of sound
A	local cross-sectional area of the channel
c_p	specific heat at constant pressure
d	local diameter of the channel
f_{1R}	oscillation frequency of the radial pressure wave
H_2	hydrogen (diatomic)
He	helium
h	local gas enthalpy
l	length of the driven channel
M	local Mach number
M_R	reflected shock wave Mach number
M_R^*	reflected shock wave reference Mach number
M_S	incident shock wave Mach number
M_S^*	incident shock wave reference Mach number
p	local gas static pressure
p_{atm}	atmospheric pressure
p_c	combustion chamber pressure
R	specific gas constant
t	flow time
T	local gas absolute temperature
u	local flow velocity
V_S	velocity of the incident shock wave
V_S^*	incident shock wave reference velocity
V_R	velocity of the reflected shock wave
x	local distance along the axis of the shock tube

Greek

γ local gas specific heat ratio

ρ local gas density

Chapter 1. Introduction

1.1 Background

Combustion instability occurring in the combustion chamber of a solid-propellant rocket motor (SRM) is a continuing problem in the design, development, production, and long-term retention of these motors.[1,2,3,4,5] There seem to be two types of combustion instability:[6,7,8] a set of acoustic resonances or pressure oscillations, which can occur with any rocket motor, and a vortex shedding phenomenon, which occurs only with particular types of segmented propellant grains. Combustion instability can be spontaneous, it is often generated at some particular time during the motor burn period, and it is usually repeatable in identical motors. Both axial waves and transverse (radial and/or tangential) waves can occur. Figure 1.1 shows a pressure-time profile with typical instability symptoms (pressure oscillations accompanied in this example with a base pressure rise, also known as a dc shift). Instability is a condition that should be avoided, and must be carefully investigated and remedied if it is identified during the motor development program.

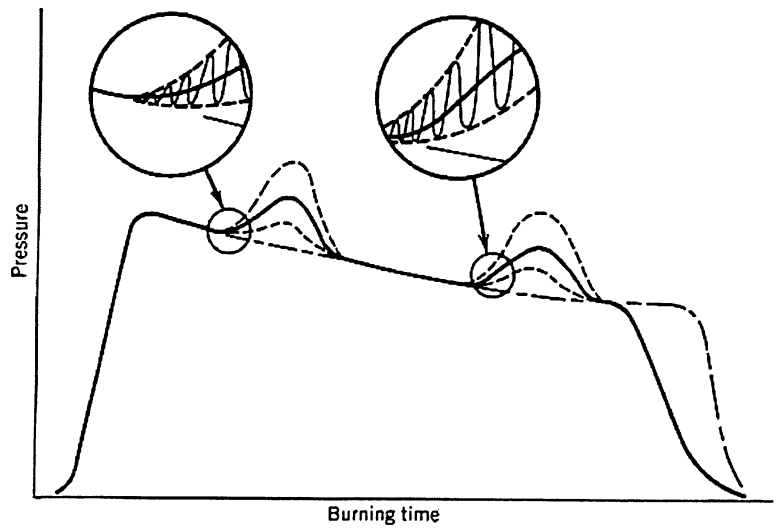

Figure 1.1. Pressure-time profile for an SRM, combustion instability scenario[3]

Combustion instability symptoms may arise when a solid rocket motor is disturbed from its stable operating conditions, with the initial disturbance potentially due to various sources, such as small pieces of propellant or wall insulation passing through the nozzle, abrupt burning of reactants in the propellant, etc.[9,10] An SRM undergoing combustion instability evaluation tests may have a disturbance initiated deliberately using an internal pyrotechnic charge. In addition, external pulses, such as those applied for static motor testing or a nearby explosion may trigger combustion instability in an SRM.[11,12] When a solid-propellant rocket motor with a cylindrical grain, as illustrated in Fig. 1.2, experiences unstable combustion, travelling axial pressure waves of significant strength can move back and forth along the length of the motor chamber. When instability occurs, the net burning rate, chamber pressure, and thrust in conjunction may also increase. The change in the motor's thrust-time profile may cause significant changes in the vehicle's flight path, and can lead to failure of the mission. If prolonged and if the vibration energy level is high, the instability can cause damage to the flight vehicle's hardware, and possibly lead to catastrophic motor failure.

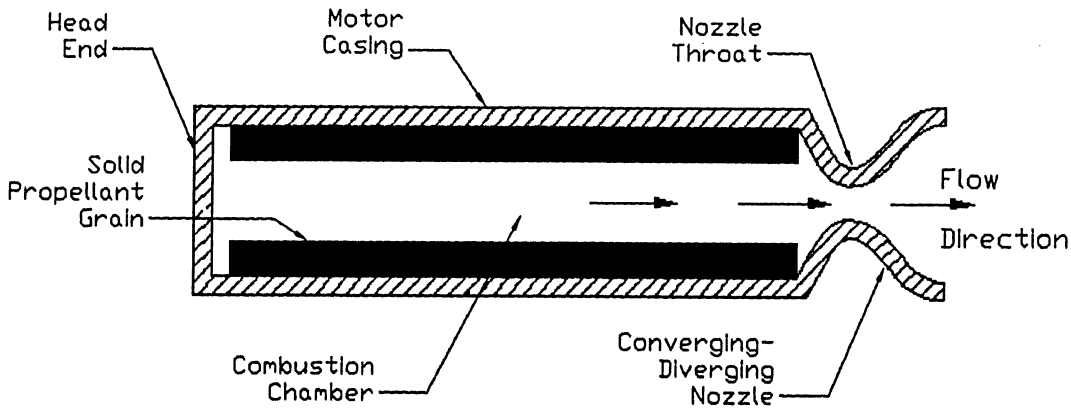

Figure 1.2. Schematic of a solid propellant rocket motor with cylindrical grain

It cannot in general be said that a particular factor alone is a prime cause of this sort of instability; it is probably a combination of various factors that is responsible for its appearance. These factors may include higher than normal mean chamber pressure,[2,10]

triggering pulse time lag after the motor's initial ignition, propellant burning rate,[5] propellant grain shape and internal area transition,[9,13,14] length of combustion chamber,[15] amplitude and shape of triggering pulse,[16] type of propellant,[17,18] percentage of stability additives in the propellant, nozzle throat to grain-port area ratio,[19] head-end area cavities (relevant to the present study's principal focus), motor gas cavity and structural oscillation frequency,[16,20] and motor mass.[5]

There are two types of combustion instabilities:[10,19] linear and non-linear. In the linear case, a small amplitude pulse triggers the flow oscillations within the combustion chamber of an SRM; whereas, in the non-linear case, a larger amplitude pulse triggers the development of sustained waves. In the present study, the focus is on non-linear axial combustion instability. This type of instability will be present in a solid rocket motor if there exist axial pressure waves of significant strength.[21] In addition to the longitudinal (i.e., axial) waves, traverse waves,[22] travelling laterally, may occur at given locations along the motor (e.g., head-end and nozzle regions).

Over the years, a number of different driving mechanisms have been identified as potential sources for sustained symptoms typically associated with non-linear axial combustion instability in liquid and solid propellant rocket motors. In the case of SRMs, these proposed mechanisms can range from frequency-dependent, pressure- and velocity-coupled combustion response to the flow above the solid propellant's burning surface,[23] to cyclic acceleration-augmented burning resulting from local propellant grain/casing structural vibration. Additionally, and more pertinent to the present investigation, observation of experimental and numerical pulsed-firing pressure-time profiles at higher than normal mean chamber pressures and propellant base burning rates suggested that a gasdynamic mechanism of reflected shock wave reinforcement in the nozzle and head end regions of the motor might be playing a significant role in some cases.[7]

The burning process of the SRM's propellant produces high-pressure and high-temperature combustion products (generally gases, but sometimes a small fraction of condensed particles) inside the chamber. These hot gases are expanded through the nozzle so as to produce thrust. The combustion chamber pressure p_c rises to a quasi-equilibrium state after ignition, at which point the main firing phase occurs, until the propellant is burned out and p_c tails off, as shown in Fig. 1.3.[24] The illustrated head-end

pressure-time profile is referred to as progressive, with pressure, thrust, and burning surface area increasing[3] with time in the main firing phase.

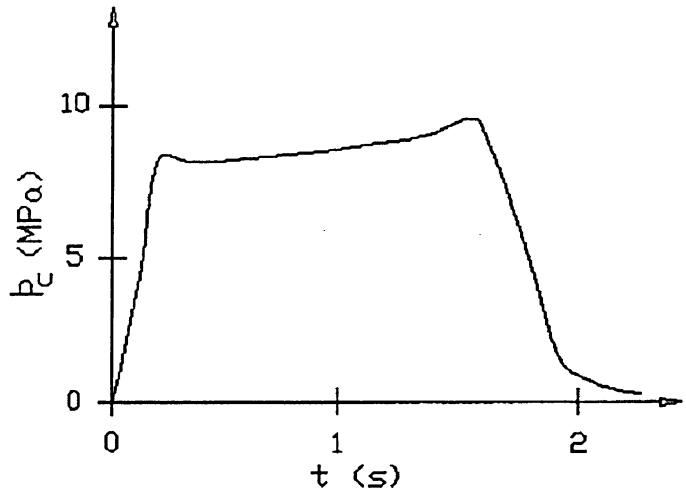

Figure 1.3. Pressure-time profile, head-end region, for normal operation of a cylindrical-grain SRM[24]

At a given time during the main firing phase, the pressure and the temperature of the gas decrease whereas the velocity increases as a function of motor length, moving rightward from the motor's head end to the aft nozzle entry, as shown in Fig. 1.4.[1] As noted earlier, a disturbance can potentially move the internal ballistic operation away from the nominal condition described here, with a travelling axial compression wave superimposed on the base internal flow, reflecting and re-reflecting from the head end region.

The most fundamental and simplest configuration of an SRM is the standard radially burning cylindrical-grain rocket motor[25] shown in Fig. 1.2. A conventional motor consists of a combustion chamber and a converging-diverging nozzle. The combustion chamber is essentially a high-pressure tank containing the solid propellant charge, called the grain, and sufficient empty space to allow for proper combustion and internal flow. The walls of the chamber are sufficiently thick and internally coated with an insulating

material to withstand thermal stresses from high-temperature combustion, in addition to the high-pressure loading.

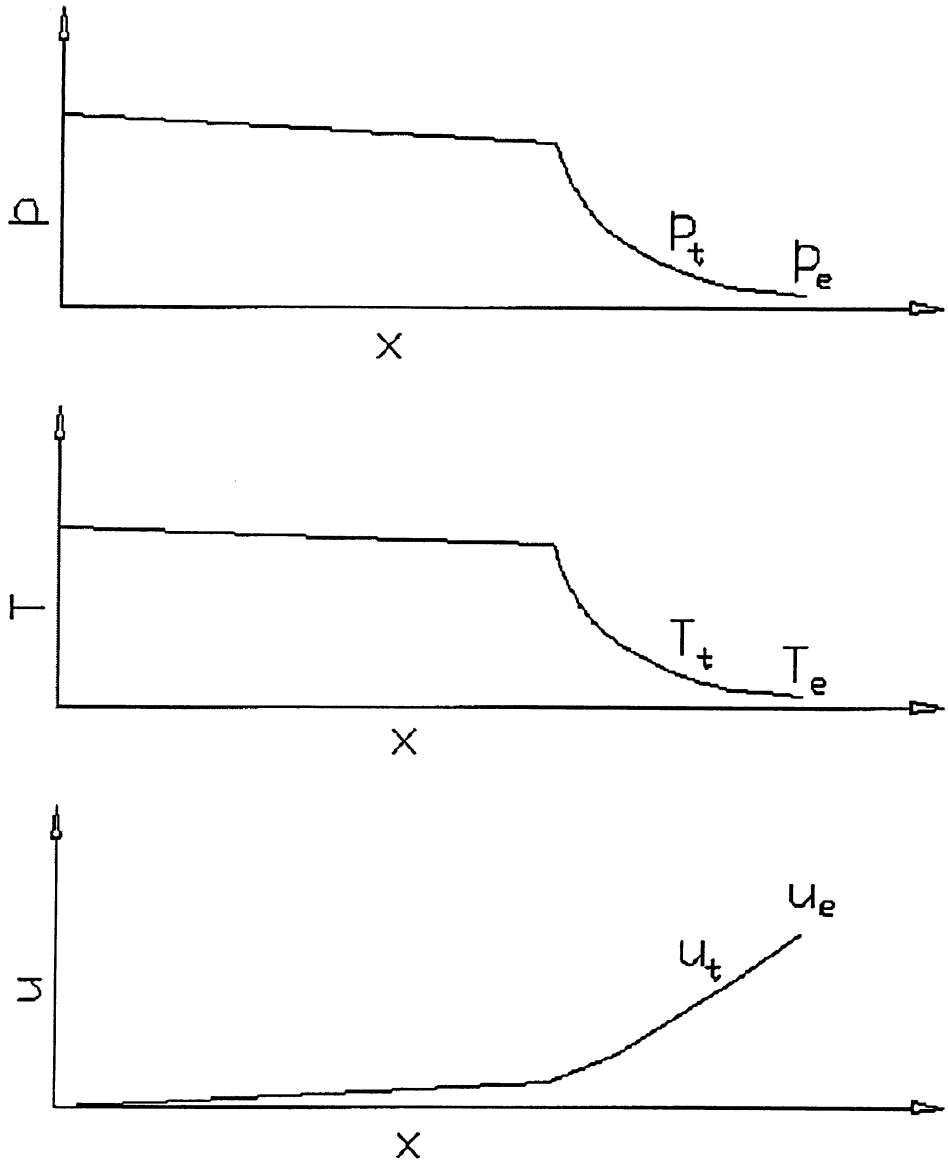

Figure 1.4. Pressure, temperature, and velocity distribution along the motor's axis at a given time[1]

1.2 Present Study

As a follow-on study to that done earlier for the nozzle region,[26] the current research is directed towards observing and evaluating the shock interaction process in the head end region of a cylindrical-grain SRM. Specifically, experimental and numerical studies are undertaken to examine various aspects pertaining to the interaction of an incident travelling shock wave with a solid rocket motor's head end (forward section), in order to identify any potential gasdynamic mechanism of wave reinforcement pertinent to combustion instability behaviour in these motors. This investigation assumes the existence of a "gap" at the motor's forward head end. This gap is defined as follows: gap width, axially, the distance between the grain's end face position and the end wall, and gap depth, radially, beyond the central port area of the grain.

The influence of several parameters (e.g., gap geometry – gap width and gap depth – and the strength of the incident normal shock wave as a function of the shock tube chambers' initial pressure) on the interaction of a traveling incident normal shock wave with the head-end region was investigated. This parametric analysis of the head end gap influence in a combustion instability scenario, when traveling shock waves are moving back and forth along the combustion chamber, is of particular interest for a number of SRM designs that have head-end gaps of varying sizes, both at the commercial level (e.g., Fig. 1.5,[27] Ariane 5) and experimental/research level (e.g., Fig. 1.6, Harris and Greatrix's experimental motor,[7] and Fig.1.7, Blomshield and Stalnaker's rocket motor[29]).

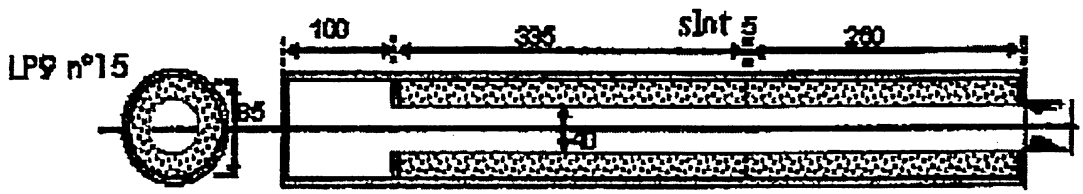

Figure 1.5. Ariane 5, subscale rocket motor, LP9 set-up[27]

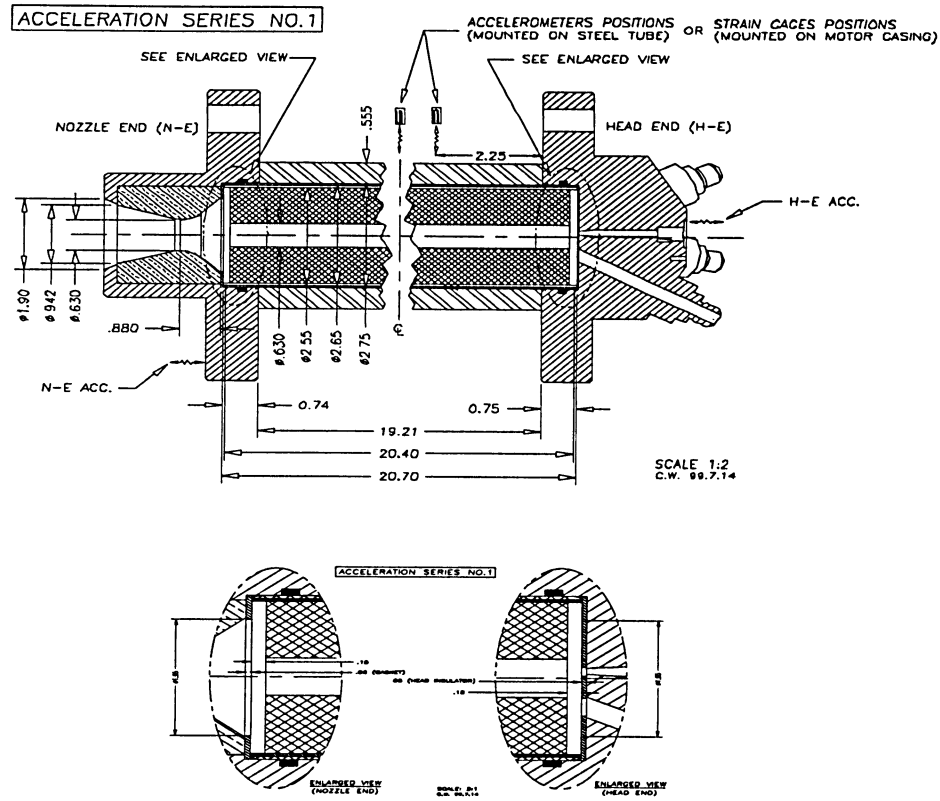

Figure 1.6. Experimental rocket motor[7]

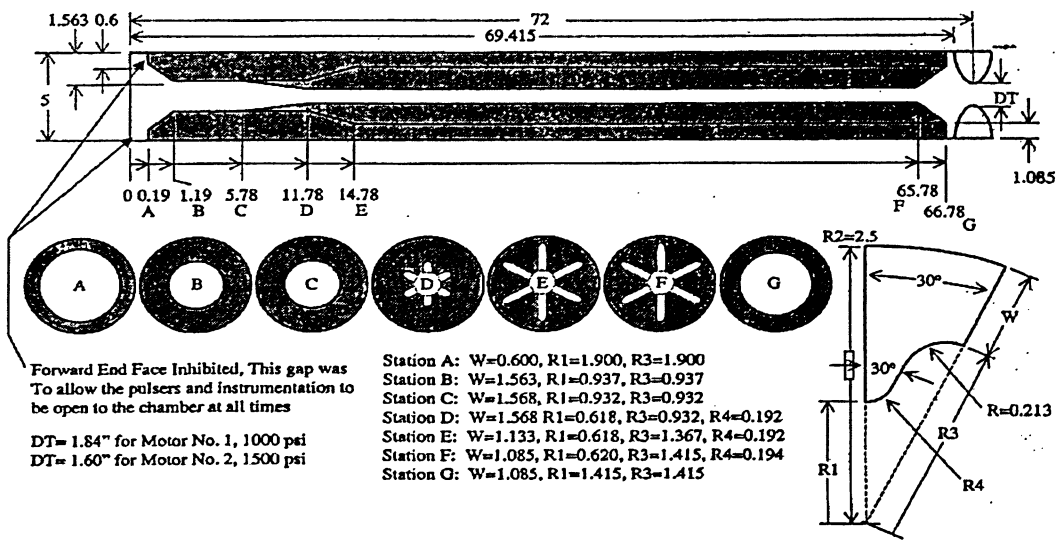

Figure 1.7. Experimental rocket motor[29]

A cold-flow experiment, based on a shock tube scheme tailored to the present application, is used in the current study towards providing information surrounding the interaction process. Because of the limitations of the air supply pressure, the shock tube is operated at substantially lower pressures than those typically occurring in SRMs. There was an expectation that at least some of the key aspects of the flow behaviour experienced in solid rocket motors would be evident in a lower pressure situation. It should be noted that although the current study was conducted at low-pressure values, the initial pressure ratio, used in the reference case, generates an incident shock wave with a comparable wavefront Mach number as that seen in a typical solid rocket motor experiencing combustion instability. Therefore, the radial oscillations, superimposed on the main reflected shock wave, analyzed in the current investigation would have similar values in relative terms to those noted in a hot-fired SRM. A number of experimental runs/firings for various head end gap geometries, and at different channel and driver pressures, are conducted as part of this investigation.

Computational fluid dynamics (CFD) simulations are generated via FLUENT, version 6.1, for comparison with the experimental results, and to provide additional information with respect to the flow behaviour. Various simulations, including differing gap geometries and pressures beyond the experimental apparatus capabilities, are undertaken as part of this investigative process.

Chapter 2. Experimental Shock Tube Apparatus

2.1 Shock Tube Theory

Shock tubes[29,30] have been employed by a number of researchers as a reliable tool for investigating the structure of shock waves, shock wave propagations and reflections. Although discovered around the turn of the century, the shock tube did not become an important research tool until after 1950. It is the device of choice for studying chemical kinetics, plasma physics, and various flow properties and phenomena related to shock waves. In addition to the high-speed compressible flow studies, shock tubes have also been used for aerodynamic testing of supersonic bodies and hypersonic entry vehicles.

For a review of shock tube flow and wave propagation,[31,32,33] one can begin with a brief description of the relations across a normal shock wave. When a perfect gas flowing supersonically with pressure p_1, density ρ_1, temperature T_1, and velocity u_1 encounters a discontinuity, then the pressure jumps to p_2, the density to ρ_2, the temperature to T_2 and the velocity to u_2 behind the shock wave front. Figure 2.1 shows the flow-property jumps across a standing, leftward-facing shock wave.

The steady-state flow across a shock wave is governed by the following fundamental equations:[34,35,36]

Continuity:

$$\rho_1 u_1 = \rho_2 u_2 \tag{2.1}$$

Momentum:

$$p_1 + \rho_1 u_1^2 = p_2 + \rho_2 u_2^2 \tag{2.2}$$

Energy:

$$h_1 + \frac{u_1^2}{2} = h_2 + \frac{u_2^2}{2} \tag{2.3}$$

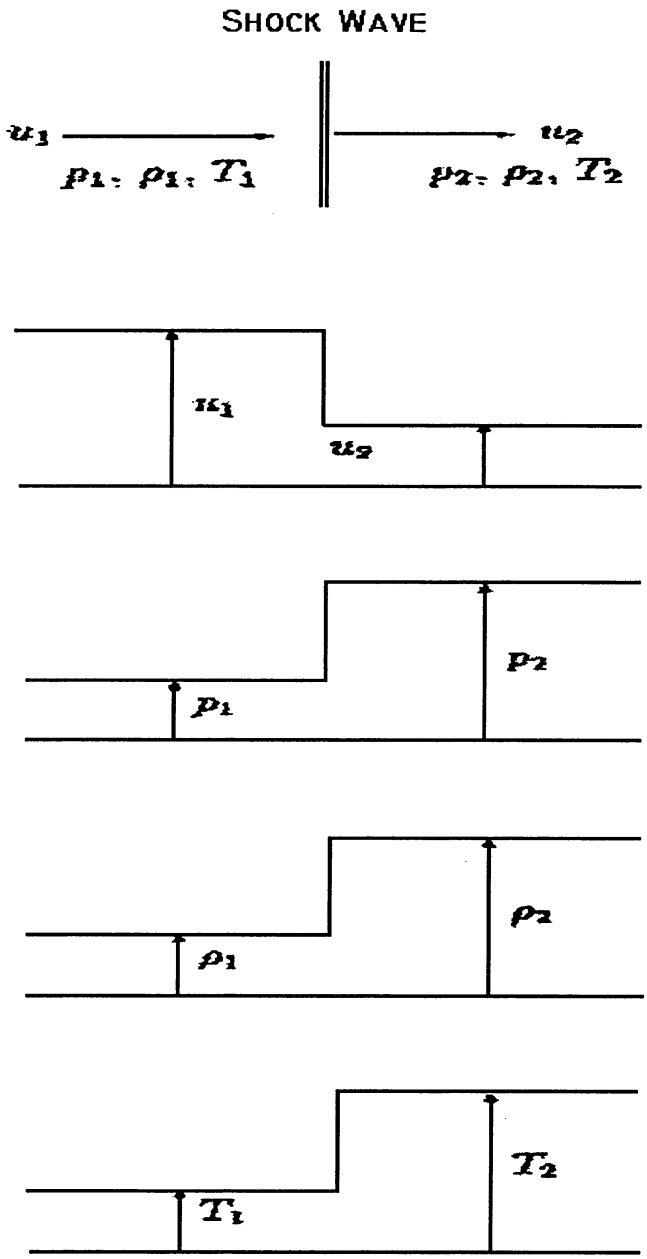

Figure 2.1. Flow-property jumps across a standing, leftward-facing shock wave[31]

In addition, for a calorically perfect gas, the following relationship apply:

$$p = \rho RT\,, \tag{2.4}$$

where R is the specific gas constant, and for an incremental change in enthalpy,

$$dh = c_p dT\,, \tag{2.5}$$

where c_p is the specific heat at constant pressure, and for local speed of sound

$$a^2 = \gamma RT = \gamma \frac{p}{\rho}, \tag{2.6}$$

where γ is the specific heat ratio.

Solving the above system of equations (i.e., Equations 2.1 to 2.6), one can obtain:

$$M_2^2 = \frac{1 + [(\gamma - 1)/2] M_1^2}{\gamma M_1^2 - (\gamma - 1)/2} \tag{2.7}$$

where the Mach number is given by: $M = u/a$.

Equation (2.7) is the first major result for a normal shock wave: it states that the flow Mach number behind the wave front, M_2, is a function only of the flow Mach number ahead of the wave front, M_1.

The next step is to determine the ratio of the thermodynamic properties ρ_2 / ρ_1, p_2 / p_1, and T_2 / T_1 across a normal shock wave.

One can obtain the equation for the densities ratio ahead and behind the shock wave by:

$$\frac{\rho_2}{\rho_1} = \frac{u_1}{u_2} = \frac{(\gamma + 1) M_1^2}{2 + (\gamma - 1) M_1^2} \tag{2.8}$$

The pressure ratio can be calculated from the momentum equation (Equation 2.2), using Equation (2.8). The final result is given by:

$$\frac{p_2}{p_1} = 1 + \frac{2\gamma}{\gamma + 1}(M_1^2 - 1) \tag{2.9}$$

Using the equation of state $p = \rho RT$ and Equation (2.9), one can obtain the temperature ratio as:

$$\frac{T_2}{T_1} = \frac{h_2}{h_2} = \left[1 + \frac{2\gamma}{\gamma + 1}(M_1^2 - 1)\right] \frac{2 + (\gamma - 1) M_1^2}{(\gamma + 1) M_1^2} \tag{2.10}$$

Equations (2.8), (2.9), and (2.10) show that the upstream flow Mach number is the determining parameter for change across a normal shock wave in a calorically perfect gas.

For the current study, a customized shock tube is used. The shock tube consists of a long tube having a constant cross-section for most of its length (up to the head-end). A

diaphragm separates a region of high-pressure gas at pressure p_4 (Region 4) from a region of low-pressure gas at pressure p_1 (Region 1), as shown in Fig. 2.2. The two quiescent gases, separated by the diaphragm, can have different values for temperature, pressure, density, and even for γ.

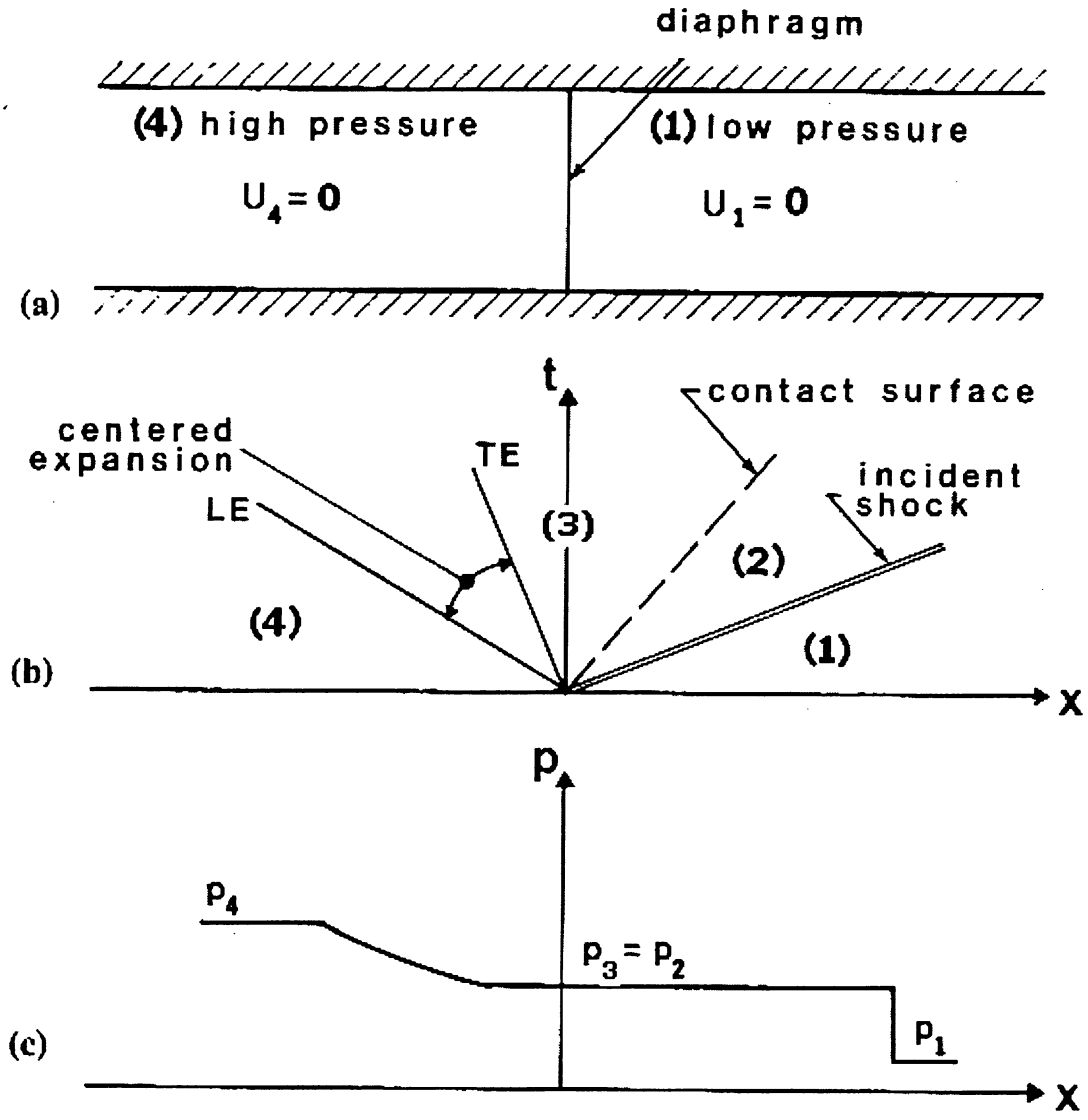

Figure 2.2. Ideal shock tube operation: (a) schematic of the shock tube before diaphragm rupture; (b) *x-t* diagram showing the principal flow features; (c) pressure trace at a given time after rupture.[33]

Although in the present investigation, air, at room temperature, has been used, it will be assumed that initially there are two different gases separated by the diaphragm, in order to evaluate the more general relations of the shock tube. The high-pressure region (Region 4) is also known as the driver channel, and the low-pressure region (Region 1) is called the driven channel. The difference between the initial pressures, p_4 and p_1, determine the load on the diaphragm, as well as the resulting shock strength.

When the diaphragm is broken by electrical or mechanical means (or in this study, by application of a pressure differential across the diaphragm at its natural rupture point), a compression shock wave is propagated into Region 1 and an expansion (or rarefaction) wave into Region 4. The expected wave behaviour occurring inside the shock tube, soon after the diaphragm is ruptured, is depicted in Fig. 2.3. One should note that the shock tube is presented in an axisymmetric representation.

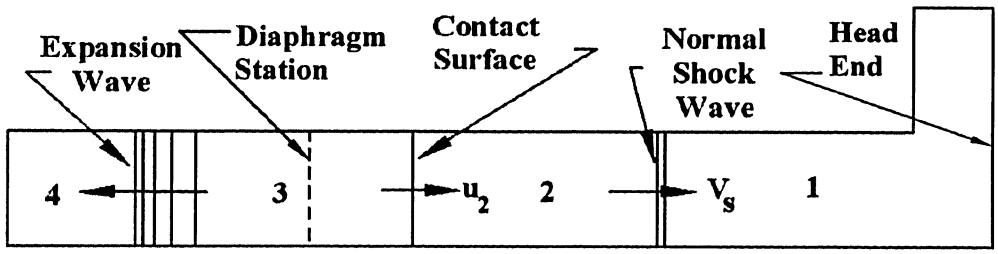

Figure 2.3. Flow inside the shock tube after the diaphragm is ruptured – axisymmetric model

The *x-t* (time – distance) diagram and pressure variation is presented in Fig. 2.2 (b) and (c). One should note that the first expansion wave, at the front of the leftward-moving expansion waves, is called *leading edge* (LE) and the last one is called the *trailing edge* (TE). Before the basic flow expressions are presented, it should be noted that the shock tube theory here invokes an underlying assumption of quasi-one-dimensional and inviscid flow. In the current investigation, transient two-dimensional

flow behaviour may be significant and must be accounted for, with respect to shock wave reflection from the head-end region.

In order to correctly use the previous shock jump relations, one needs to transform the moving shock wave coordinate system (Fig. 2.3) into a standing shock wave coordinate system. This can be done by considering the flow in Region 1 as a leftward-moving flow (initially $u_1 = 0$) to the standing shock wave. The velocity of the gas ahead the incident shock wave, relative to the wave becomes V_s and the velocity of the gas behind the shock wave will be $(V_s - u_2)$. Equation (2.21) can be written as:

$$M_s^2 = \frac{\gamma_1 + 1}{2\gamma_1}\frac{p_2}{p_1} + \frac{\gamma_1 - 1}{2\gamma_1} \tag{2.11}$$

The velocity behind the shock wave is given by:

$$V_2 = V_s - u_2 \tag{2.12}$$

so that:

$$\frac{V_2}{a_1} = \frac{2}{\gamma_1 + 1}\frac{M_s^2 - 1}{M_s} \tag{2.13}$$

Combining Equation (2.11) and (2.13), one obtains:

$$V_2 = a_1\left(\frac{p_2}{p_1} - 1\right)\left[\frac{2/\gamma_1}{(\gamma_1 + 1)(p_2/p_1) + (\gamma_1 - 1)}\right]^{1/2} \tag{2.14}$$

The pressure ratio across the expansion wave (Fig. 2.3) is determined by the *method of characteristics*, and is given by:[33,34]

$$\frac{p_3}{p_4} = \left(1 - \frac{(\gamma_4 - 1)}{2}\frac{V_3}{a_4}\right)^{\frac{2\gamma_4}{\gamma_4 - 1}} \tag{2.15}$$

Solving for V_3, one obtains:

$$V_3 = \frac{2a_4}{\gamma_4 - 1}\left[1 - \left(\frac{p_3}{p_1}\frac{p_1}{p_4}\right)^{\frac{\gamma_4 - 1}{2\gamma_4}}\right] \tag{2.16}$$

The region behind the contact surface is referred to as Region 3. Although the temperature and the density could be different across the contact surface, the velocities and pressures at both sides of the contact surface must be equal:

$$V_3 = V_2 \tag{2.17}$$

$$p_3 = p_2 \tag{2.18}$$

Combining Equations (2.14), (2.16), (2.17), and (2.18) and solving for the ratio p_4/p_1, it can be shown that:

$$\frac{p_4}{p_1} = \frac{p_2}{p_1}\left(1 - \frac{(\gamma_4 - 1)(a_1/a_4)[(p_2/p_1) - 1]}{\{4\gamma_1^2 + 2\gamma_1(\gamma_1 + 1)[(p_2/p_1) - 1]\}^{1/2}}\right)^{\frac{-2\gamma_4}{\gamma_4 - 1}} \tag{2.19}$$

Equation (2.19) gives the incident shock strength p_2/p_1 as a function of the diaphragm pressure ratio p_4/p_1. Once p_2/p_1 is known, other quantities across the moving shock are readily determined. Although it is difficult to see from Equation (2.19), an evaluation of this relation shows that, for a given pressure ratio p_4/p_1, the incident shock strength p_2/p_1 will be stronger as a_1/a_4 is made smaller. Moreover, the speed of sound in a light gas is faster than in a heavy gas. Thus, to maximize the incident shock for a given p_4/p_1, the driver gas should be a low-molecular-weight gas at high temperature (hence high a_4), and the driven gas should be a high-molecular-weight gas at low temperature (hence low a_1). For this reason, many shock tubes in practice use H_2 or He for the driver gas, and it is heated by electrical means (arc-driven shock tubes) or by chemical combustion (combustion-driven shock tubes).

Once the moving normal shock reaches the channel's head-end wall, a reflected shock wave, moving upstream, is created as shown in Fig. 2.4.

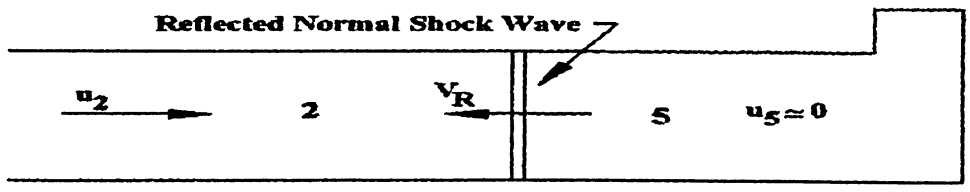

Figure 2.4. Reflected shock wave moving upstream (two-dimensional axisymmetric model)

An $x - t$ wave diagram for a conventional, constant-area shock tube channel section is shown in Fig. 2.5. At time $t = 0$ (graph origin), the incident shock wave starts from diaphragm location. Therefore, when time $t = 0$, the incident shock wave is at location $x = 0$.

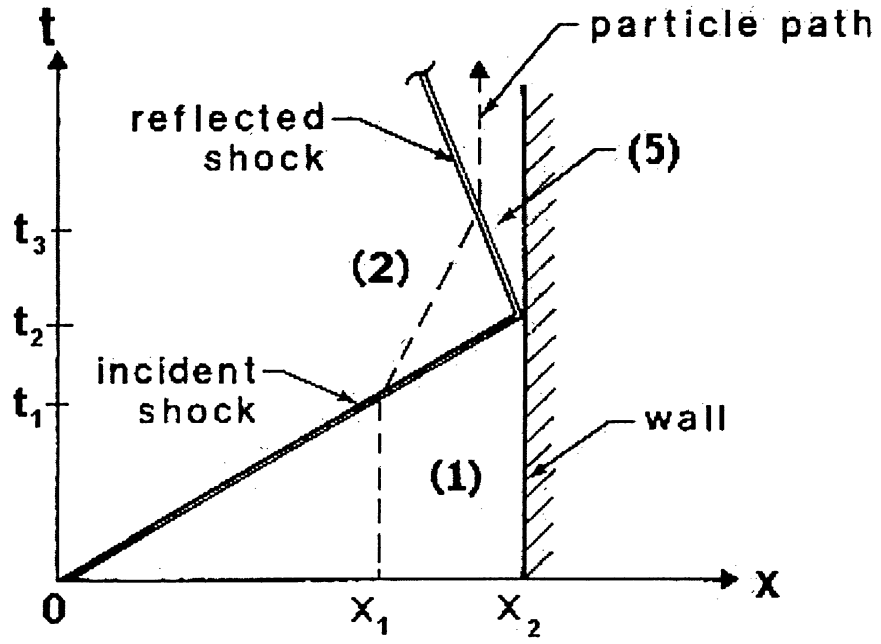

Figure 2.5. Wave diagram of a shock tube (Ref. 33, diagram modified for present application)

At some instant later ($t = t_1$), the shock wave is traveling to the right and is located at point $x = x_1$. It should be noted that the path of the incident shock wave is a straight line in the wave diaphragm. When the incident shock arrives at the head-end wall (assuming head-end gap is absent) of the shock tube (i.e., $t = t_2$ and $x = x_2$), it is reflected towards the left with velocity V_R, as shown in Fig. 2.4. The path of the reflected shock is also a straight line in the wave diagram, in this case.

The slopes of the incident and reflected shock paths are $\frac{1}{V_S}$ and $\frac{1}{V_R}$, respectively. It should be noted that a general characteristic of reflected shocks is that $|V_R|$

$< V_S$. Hence, the reflected shock path is more steeply inclined than the incident shock path. In addition to the incident and reflected shock paths, the wave diagram depicts the path of any particle that is placed inside the shock tube.

After the shock wave reflection from the end wall of the shock tube, the reflected wave travels upstream with velocity V_R. At this point it is desirable to know the conditions in Region 5, behind the reflected shock wave. The gas in this region is at rest in the ideal no-gap case, thus $u_5 = 0$. The reflected shock wave travels into the oncoming flow whose velocity is u_2. The shock jump relations are applied to the relations across the reflected shock wave by replacing the subscripts 1 and 2 by 2 and 5, respectively. Therefore, Equation (2.9) becomes:

$$\frac{p_5}{p_2} = 1 + \frac{2\gamma}{\gamma+1}(M_r^2 - 1) \tag{2.20}$$

The reference Mach number of the reflected normal shock wave front as a function of the incident shock front Mach number is given by:

$$M_r = \left[\frac{\gamma M_s^2 - \frac{\gamma-1}{2}}{1 + \left(\frac{\gamma-1}{2}\right) M_s^2} \right]^{1/2} \tag{2.21}$$

Note that $M_r M_2 = 1$, where M_2 is given by Equation (2.7), replacing M_1 with M_s for the incident shock wave. The M_r parameter is rather narrowly bounded, as can be seen from Equation (2.21):

$$M_r = 1, \text{ when } M_s = 1$$

and

$$M_r = \left(\frac{2\gamma}{\gamma-1}\right)^{1/2}, \text{ when } M_s \to \infty .$$

The actual reflected shock wave front Mach number is calculated by:

$$M_R = M_r - M_2 \tag{2.22}$$

The above one-dimensional theory provides quasi-steady values as a guideline; short-term, transient transverse wave motion arising in the vicinity of the gap area is not accounted for, as later experimental and numerical results make clear.

The aforementioned equations provide a brief background concerning the behaviour of incident and reflected shock waves inside a shock tube. A description of the expansion waves has not been provided here, since the purpose of this thesis is to study the reflected shock behaviour, before it interacts with the expansion waves. Investigations may be carried out in either section (driver or driven channels) of the shock tube; however, the most common test section, as in this thesis, is the driven channel. A number of optical methods such as shadowgraphs, Schlieren and Mach-Zehnder interferometry, can be used for obtaining flow measurements inside shock tubes.[29,32] These methods can be expensive, and sometimes difficult to adjust for operation. Other methods employing high-frequency data sampling techniques are commonly used, as in this investigation, for pressure measurements. For measuring the flow temperature inside a shock tube, thermocouples can be installed.[30] Once the pressure and temperature measurements have been taken, it is straightforward to determine various flow parameters inside the shock tube with the help of incident and reflected shock wave relations. In addition to the above experimental methods, shock tube results can also be predicted through numerical simulations, enabling a more comprehensive understanding of the flow phenomena involved.

2.2 Cold-Flow Experimental Apparatus

The previous section provides a general overview of the shock tube theory that can be applied to the customized experimental cold-flow apparatus used in the present study. The various one-dimensional equations related to the traveling normal incident and reflected shock waves are used to estimate key parameters of the experimental shock tube analysis. Various design considerations, together with the calculation of parameters pertinent to the apparatus, are described in the following paragraphs.

2.2.1 Design Analysis

It was noted in the planning and designing of the apparatus, that one requires air, at pressure higher than room pressure, in both channels of the shock tube. The air supply is made available through either the university's main air distribution line or by a two-stage compressor installed along with an air reservoir in the laboratory (Room KHE33 at Ryerson University). The shock tube apparatus is attached to the reservoir via an isolation ball valve. Also, the apparatus is easily connected to the main distribution line. The reservoir can also be used as an alternative air source in the event that the distribution line is unable to deliver the desired pressure. Furthermore, the reservoir provides a means of passing high-pressure air through the channel, by opening the isolation valve, to ensure the absence of debris prior to an experimental firing (in the open-ended case, i.e., head end removed or nozzle in place).

The available air supply from the distribution line doesn't provide a steady pressure, thus a pressure regulator with an appropriate adjustment range of pressure is used to regulate the pressure in providing a controlled supply to the driven (primary) channel. A major concern of the design was to find a method of pressurizing the two channels of the shock tube in such a way so as to prevent an excess or uncontrolled differential pressure across the diaphragm. The differential pressure control is necessary to prevent any kind of premature rupture of the diaphragm, which separates the driver (secondary) and driven chambers. This issue was solved by branching the reservoir air supply (connected to the air compressor) to the driver channel. A boost-pressure valve along with a flow restrictor can control the volume and pressure of air supply into the secondary section of the shock tube. The boost-pressure valve is a push-button-type spool valve that enables fine pressure control in the driver channel. This type of control (i.e., pressure regulator for the main air distribution line and boost-pressure valve for the reservoir air supply) can be used to produce a precise differential pressure, which governs the shock strength upon rupturing of the diaphragm.

Up to the point when the desired pressure is reached in the primary channel, the secondary chamber is simultaneously pressurized by the boost-pressure valve so as to avoid premature weakening or the rupture of the diaphragm. Hence, when the pressure in

the driven and the driver channels is equal with p_1 (i.e., the initial desired value for the driven channel), one starts pressurizing only the driver chamber to achieve the necessary differential pressure (across the diaphragm) for the diaphragm rupture and flow initialization. Once the flow has been generated, the next step in the process is to take transient pressure measurements at a specified location upstream of the shock tube head-end. Employing a high-frequency data sampling system, connected to a pressure transducer of appropriate operating range, via a charge amplifier, solves this problem. The pressure transducer is located 10 cm upstream of the head-end region, at the shock tube's wall. Fig. 2.6 depicts a schematic diagram of the experimental apparatus.

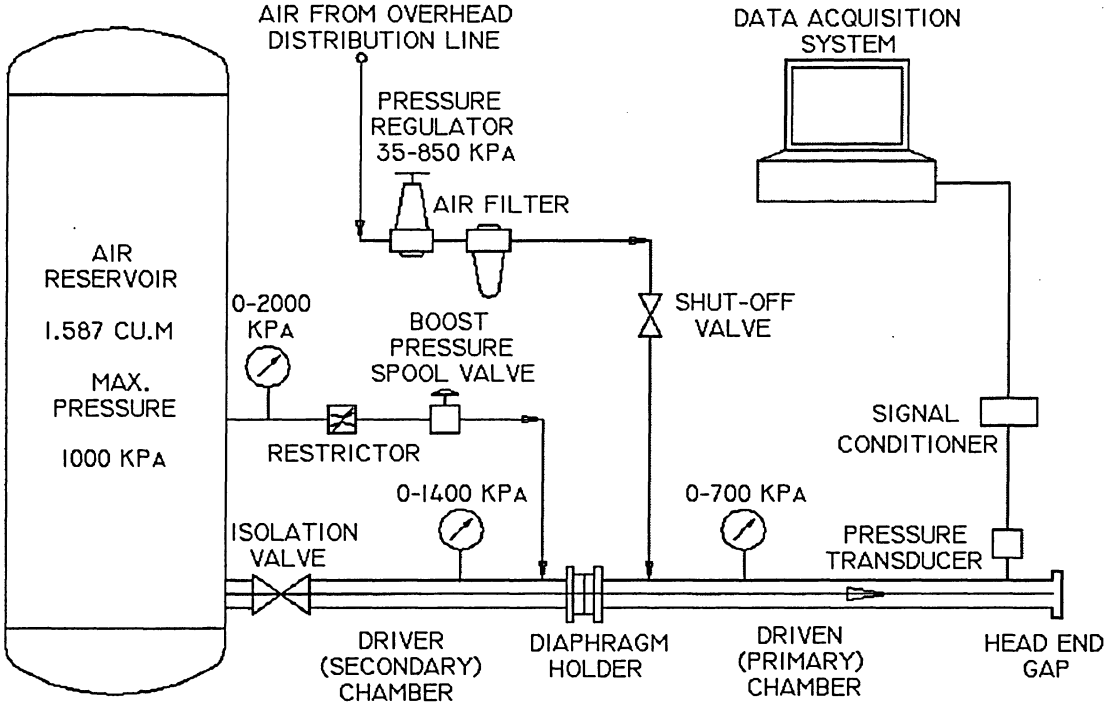

Figure 2.6. Schematic diagram of experimental apparatus

2.2.2 Operating Pressure and Channels Size

Once the working components of the apparatus are established, one can proceed further to identify a general starting pressure level for the apparatus. As a follow-on study to that done for the nozzle region,[26] it was desired for the current study to keep for the

reference case the same initial pressures as the ones in the nozzle interaction research. Therefore, it has been decided to use for the reference case a driven channel pressure of 375 kPa (i.e., the reference pressure value used in the choked-flow nozzle experiment), although there is no minimum allowable pressure for the current study, with a closed end.

The initial pressure, p_1 = 375 kPa can be reached using the available air from the distribution line. Also, this initial pressure level is in concordance with the structural limitation and safe operation of the experimental apparatus. The current pressure transducer also limits the allowable operating pressure to levels well below the ones seen in a solid-propellant rocket motor. The pressure values for the incident and reflected shock waves are recorded as overpressures above the 375 kPa baseline.

The driven channel is pressurized via the shut-off valve, using the available air supply from the Ryerson main distribution line. Once the desired level is reached, the valve is closed and the air in the primary chamber will be at rest. Thus, the initial velocity of the air, before the diaphragm rupture is:

$$u_1 = 0$$

After deciding the initial conditions associated with the driven channel, the next step in the process is to establish the nominal reference pressure of the driver (high-pressure) chamber to produce the desired incident shock strength, and keep the shock tube within structural and operational limits. Using a standard diaphragm, the initial nominal pressure of the secondary channel was determined to be:

$$p_4 = 850 \text{ kPa.}$$

These initial values for the two chambers of the experimental shock tube apparatus are only for the reference case; multiple experimental and numerical model scenarios, involving different pressure values, are investigated in the present study.

In addition to the initial pressure level, one needs to know the remaining fluid properties in order to properly proceed with the experimental set-up and corresponding numerical analysis. The working fluid in both chambers is air, at room temperature. Therefore for the sampling calculation of the reference case, the air is considered as an ideal gas having the initial temperature:

$$T_1 = T_4 = 294 \text{ K,}$$

and the local gas specific heat ratio:

$$\gamma_1 = \gamma_4 = 1.4$$

Knowing the initial conditions and the pressure ratio when the diaphragm is ruptured: $\frac{p_4}{p_1} = 2.26667$, one can calculate the pressure behind the incident shock wave using Equation (2.19). This equation is solved iteratively with the assumption that $\gamma_1 = \gamma_4 = 1.4$ and the local speed of sound has the same value both in the driver and driven channels (specific gas constant $R = 287 \ \frac{\text{J}}{\text{kg} \cdot \text{K}}$):[31]

$$a_1 = a_4 = \sqrt{1.4 \cdot 287 \cdot 294} = 343.699 \text{ m/s.}$$

The incident normal shock pressure ratio is found to be:

$$\frac{p_2}{p_1} = 1.487$$

At this point, one can consider the implication the size of the shock tube's channels. Sizing of the experimental apparatus involves the diameter and length of the driven and driver sections. Primarily, size is governed by the available space in the aerodynamics laboratory (Room KHE33 at Ryerson University). The compressor and the reservoir are installed in the northeast corner of the laboratory and the air distribution line runs through this location as well.

A two-inch diameter pipe (i.e., 5.08 cm) is used for the driver and the driven section. The cold-flow apparatus used for the nozzle interaction study was considered appropriate for the head-end study, without significant changes of the shock tube channels' lengths. Thus, the section length values are:

- Driven chamber = 2.3 m
- Driver chamber = 1.73 m

One should note that the 2.3 meters value corresponds to the case when no gap is present in the head-end region. When the width of the gap has a value greater than zero, then this value should be added to the driven channel to obtain the entire length of the test section.

After the initial conditions and the length of the driven channel are known, one can calculate the moving shock and gas velocities, both for the incident and reflected normal shock waves (using the previously described one-dimensional approach), as well as the necessary time to collect data during the experimental firings (i.e., the time needed by the incident shock to reach the head-end region, and the time needed by the reflected shock wave to pass the transducer location).

The first step is to calculate the local Mach number of the incident moving shock front using Equation (2.11):

$$M_s = 1.19$$

The incident shock velocity is given by:

$$V_s = M_s a_1 = 1.19 \cdot 343.699 = 409 \text{ m/s}$$

Using the motion equation and considering the initial values for time and distance being equal with zero, one can estimate the incident shock wave time between the diaphragm station and the head-end:

$$t - t_0 = \frac{1}{V_s}(x - x_0)$$

$$t = \frac{2.3}{409} = 5.623 \text{ ms}$$

The above time value represents the time necessary to the incident shock wave to reach the end of the driven chamber (l = 2.3 m). For the no gap case, this is the moment when the incident shock is reflected from the head-end wall of the driven channel. In order to calculate the reflection time and velocity, one needs to know the flow parameters behind the incident shock wave (Region 2 in the shock tube theory section).

The local flow Mach number behind the incident shock wave front is obtained from Equation (2.7), where M_1 is replaced by M_s (changing from moving frame coordinates to fixed frame coordinates):

$$M_2 = 0.848$$

The temperature T_2 is obtained from Equation (2.10):

$$\frac{T_2}{T_1} = 1.1217,$$

$$T_2 = 329.8 \text{ K}$$

The local speed of sound is given by:

$$a_2 = \sqrt{1.4 \cdot 287 \cdot 329.8} = 364 \text{ m/s}$$

Thus:

$$u_2 = a_2 M_2 = 308.67 \text{ m/s}$$

The velocity of the gas behind the incident shock wave front is given by Equation (2.24):

$$V_2 = V_s - u_2 = 409 - 308.67 = 100.33 \text{ m/s}$$

The reflected shock wave Mach number is obtained from Equation (2.21):

$$M_r = 1.179$$

The actual reflected shock wave front velocity is calculated by Equation (2.22):

$$V_R = M_r a_2 - u_2 = 120.486 \text{ m/s}$$

The time necessary for the reflected shock wave to reach the transducer location (10 cm upstream of the head-end wall – no gap case) is obtained by:

$$t_r = \frac{0.1}{120.486} = 0.83 \text{ ms}$$

The total time between the diaphragm rupture and the moment when the reflected shock wave reaches the transducer location is given by:

$$t_{total} = t + t_r = 5.623 + 0.83 = 6.453 \text{ ms}$$

The experimental and numerical results of this study are presented in a pressure-time chart, the initial moment on the time axis being the one corresponding to the moment when the incident shock wave passes the pressure transducer location. As demonstrated above, the time necessary for the reflected shock wave front to reach the 10 cm position upstream of the head-end location is less than a millisecond, and it was decided that a collection data time period of 4 ms, after the incident shock passes the transducer (the trigger time), would suffice for the purpose of this investigation.

Particularly important to this investigation are the conditions behind the reflected shock wave (Region 5 in the shock tube theory section). These conditions can be estimated using the one-dimensional shock tube theory as well.

The pressure value behind the reflected shock wave is given by Equation (2.20):

$$\frac{p_5}{p_2} = 1.455,$$

$$p_5 = 1.455 \cdot 375 \cdot 1.487 = 811.35 \text{ kPa}$$

In a similar way, using the shock tube theory described at the beginning of this chapter, one can estimate some key values from the expansion wave theory (the expansion wave moving upstream of the diaphragm station to the reservoir end).

In summary, the nominal reference values for the experimental apparatus are:

- Length of driver chamber = 1.73 m
- Length of driven chamber = 2.3 m
- Diameter of pipe = 0.0508 m
- Driver chamber pressure = 375 kPa
- Driven chamber pressure = 850 kPa
- Diaphragm pressure ratio, $\frac{p_4}{p_1} = 2.2677$
- Shock pressure ratio, $\frac{p_2}{p_1} = 1.486$

The above pressure values results from one-dimensional, ideal flow theory. Exact values resulting from the experimental firings may differ due to system losses, etc.

2.2.3 Diaphragm Selection

As previously stated, the diaphragm separates the high-pressure (driver) chamber from the low-pressure (driven) channel, and the diaphragm pressure ratio, $\frac{p_4}{p_1}$, in turn determines the shock strength, $\frac{p_2}{p_1}$. Therefore, selection of the diaphragm material requires some consideration, depending upon the desired shock strength. It was shown in Section 2.2.2 that a nominal strength of 1.487, generated by an initial pressure ratio of 2.2667, would be the required condition for the reference case of this investigation. Hence, the diaphragm should burst at the above initial pressure ratio so that the desired shock strength is achieved.

When a diaphragm without a scratch (as the one used in the present experimental firings) is employed in a circular-type shock tube, a rough measure of the spontaneous rupture is given by:[29]

$$\frac{p_4}{p_1} = \frac{4df}{r} \tag{2.23}$$

where r is the diameter of the diaphragm, d is its thickness, and f is the stress at which breakage occurs in tension.

Keeping in mind the required diaphragm pressure ratio, it was established that a polyester film having a thickness of 0.08 mm would serve the purpose. The film is cut into a circular shape and is ready to use. However, while performing actual experimental firings at the nominal or other pressure settings, if it is found that there is a premature rupturing of the diaphragm and the desired shock strength is not achieved, then other diaphragm materials and thicknesses might be considered. Figure 2.7 shows a diaphragm after an actual shock tube firing.

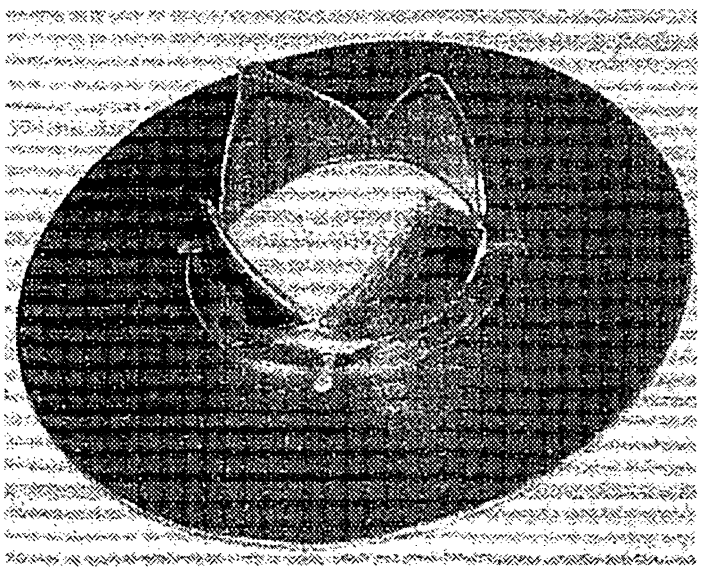

Figure 2.7. Diaphragm after the experimental firing

The diaphragm is placed in the diaphragm holder that is situated between the two channel sections. The holder is tightened into the correct position with the help of nuts and bolts as shown in Fig. 2.8. In the present study, slowly increasing the pressure in the

driver chamber to a certain level ruptures the diaphragm, rather than employing the heated fuse wire technique discussed below.

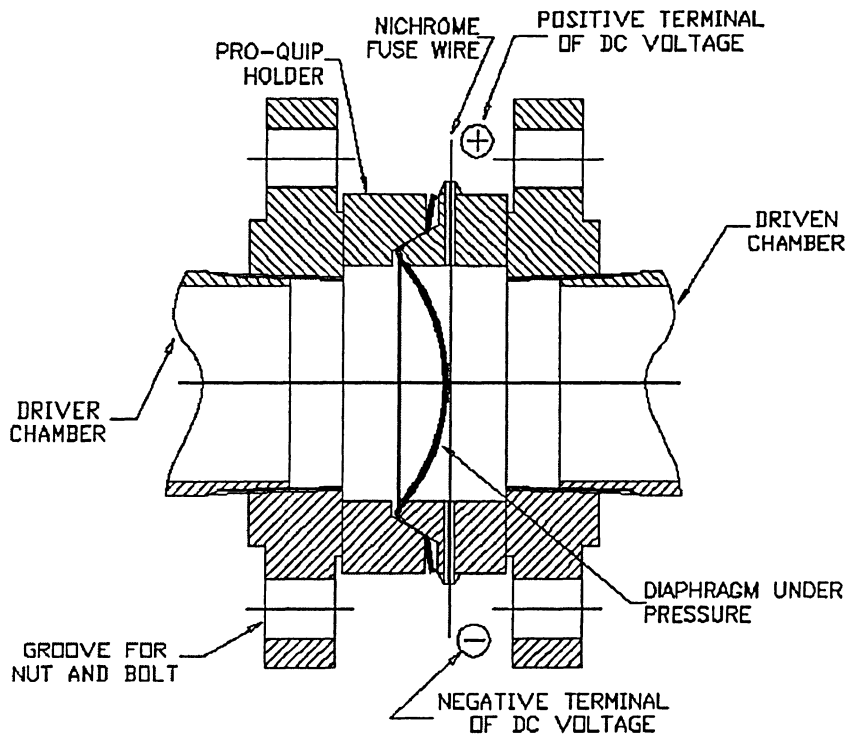

Figure 2.8. Diaphragm holder and fuse wire assembly

In order to achieve higher shock strengths, thicker diaphragm materials, such as steel, aluminium, or tin, in single or double mode operation[30] can be easily facilitated in the diaphragm holder. Usually, thicker materials are more difficult to rupture by increasing the pressure in the driver chamber. Hence, to fulfill this requirement, one can make use of a low resistance fuse wire like nichrome to melt the diaphragm. A direct current (DC) voltage is supplied to the fuse wire, which is in contact with the diaphragm surface. The localized wire temperature attained is high enough to locally melt the diaphragm, thus producing a rupture of the diaphragm material. The above rupturing mechanism is cost-effective, and desired results are easily obtained. The diaphragm holder along with the fuse wire assembly is shown in Fig. 2.8.

2.2.4. Head End Design

The head end design is very important for the experimental part of the present research. Additionally, switching between the head end and nozzle end geometries should be relatively uncomplicated. With these design considerations in mind, it was decided to attach at the end of the driven channel, on the exterior part (as shown in Fig. 2.9), a flange that can be used to connect the head end holder to the driven chamber via two bolts and nuts. Inside the holder (head end housing), the head end part can move from the no-gap case (Fig. 2.9) up to a 1-cm head end gap (Fig. 2.10).

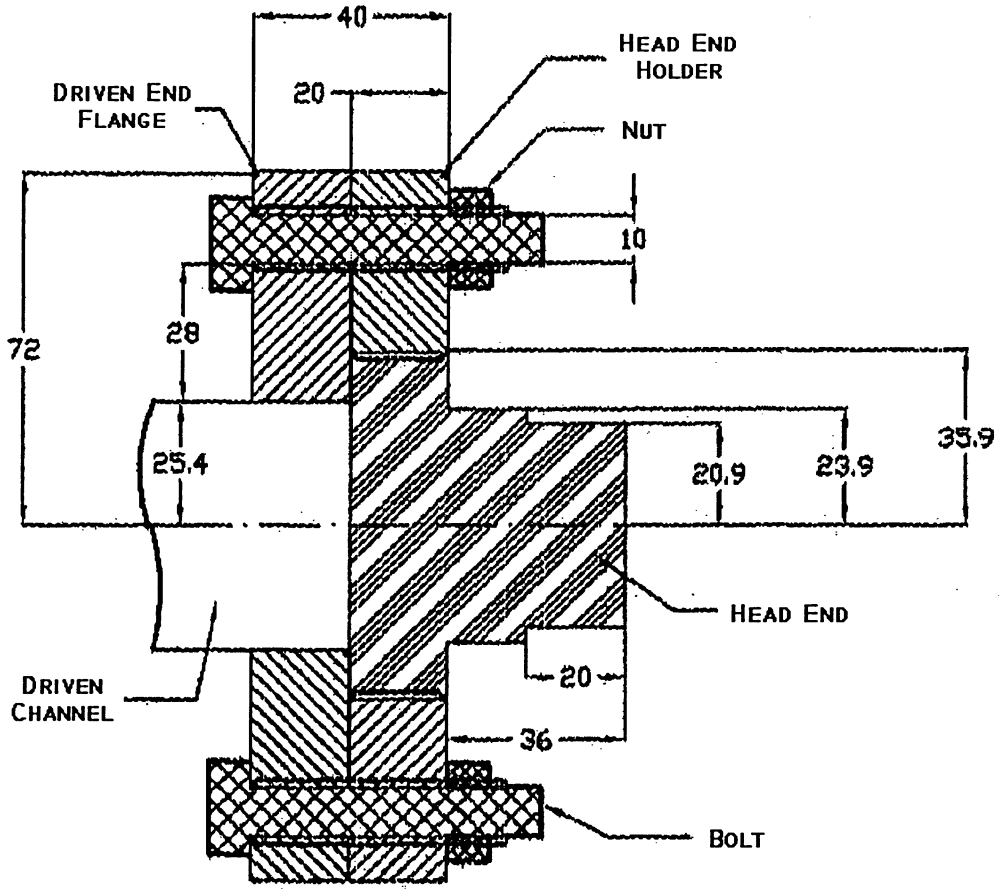

Figure 2.9. Driven – head end assembly (all dimensions in mm)

The variable geometry on the horizontal directions allows for the use of the same equipment for experimental firings with gap widths from 0 to 10 mm. The 10 mm gap width is the maximum allowed value in meeting safety concerns, the maximum gap width representing half of the total head end holder width.

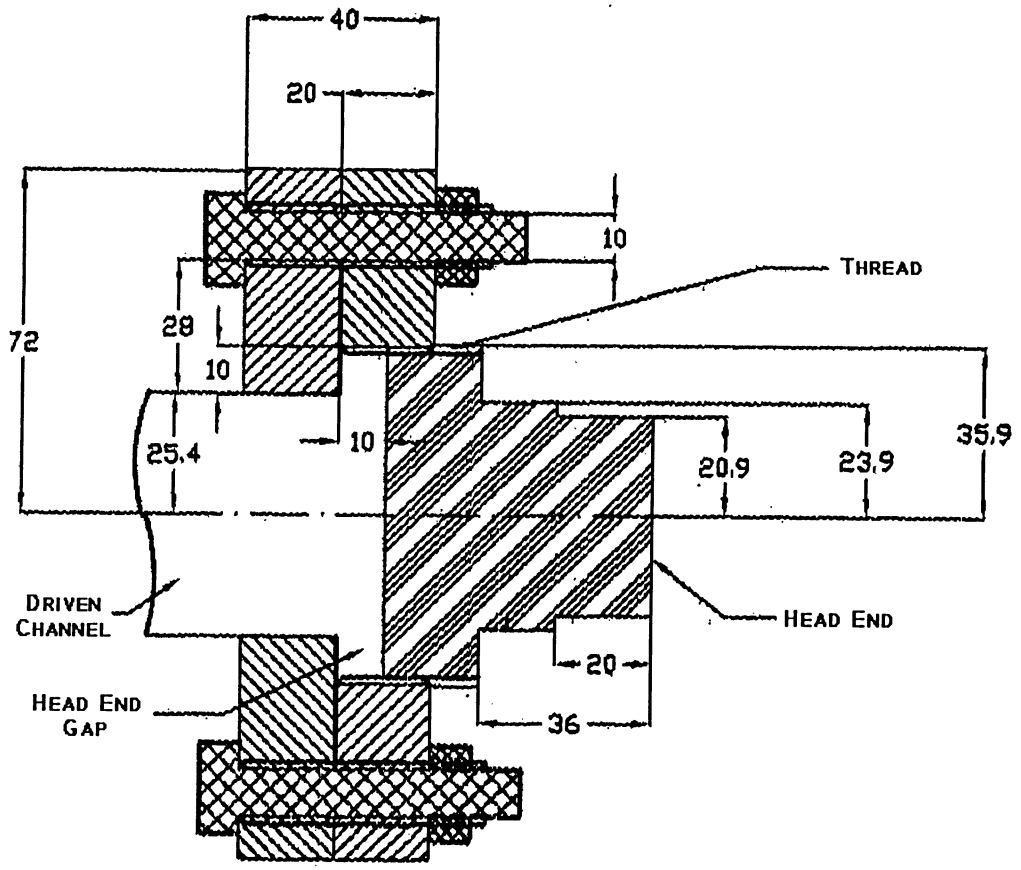

Figure 2.10. Schematic of 1 cm head end gap (all dimensions in mm)

2.2.5 Compressor

The compressor in the aerodynamics laboratory is a two-stage compressor. It is situated in the northeast corner of the laboratory. The compressor is equipped with a receiver tank, which is connected to the driver chamber of the shock tube through an isolation ball valve, as shown in Fig. 2.6. In the absence of air supply from the main

distribution line, the compressor's capacity is ample enough to provide the required pressure to the driver channel (850 kPa). The maximum pressure that can be attained in the reservoir tank is 1000 kPa. If the pressure in the tank exceeds the maximum allowed value, the compressor is shut down automatically through a pre-installed safety mechanism.

2.2.6 Primary Air Supply

In this section, the method of pressurizing the driven (primary) channel is described. A groove, made on the primary chamber tube and providing a seat for a standard 2-inch coupling manufactured by Victaulic Company coupling (as shown in Fig. 2.11), is situated at 0.12 m from the diaphragm station. The coupling consists of an annulus chamber, which acts as a plenum (an enclosure in which air or other gas is at a pressure greater than that of the outside atmosphere).

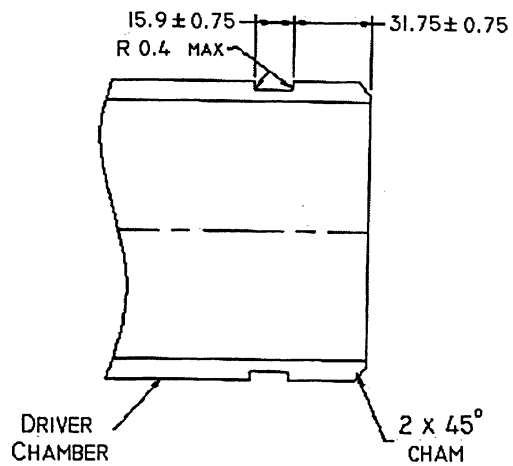

Figure 2.11. Groove details (all dimensions in mm)

The chamber diffuses the incoming airflow from the main distribution line and forces the air through a circumferential slit of 0.15 cm width. Silicone rubber is used as a sealant to seal the area around the coupling-pipe interface, as shown in Fig. 2.12, to prevent any air leakage. The desired air pressure in the driven channel is controlled via a pressure regulator attached to the main air distribution line.

Only the groove details of the driver chamber are shown in Fig. 2.11. A similar kind of groove is made on the driven channel.

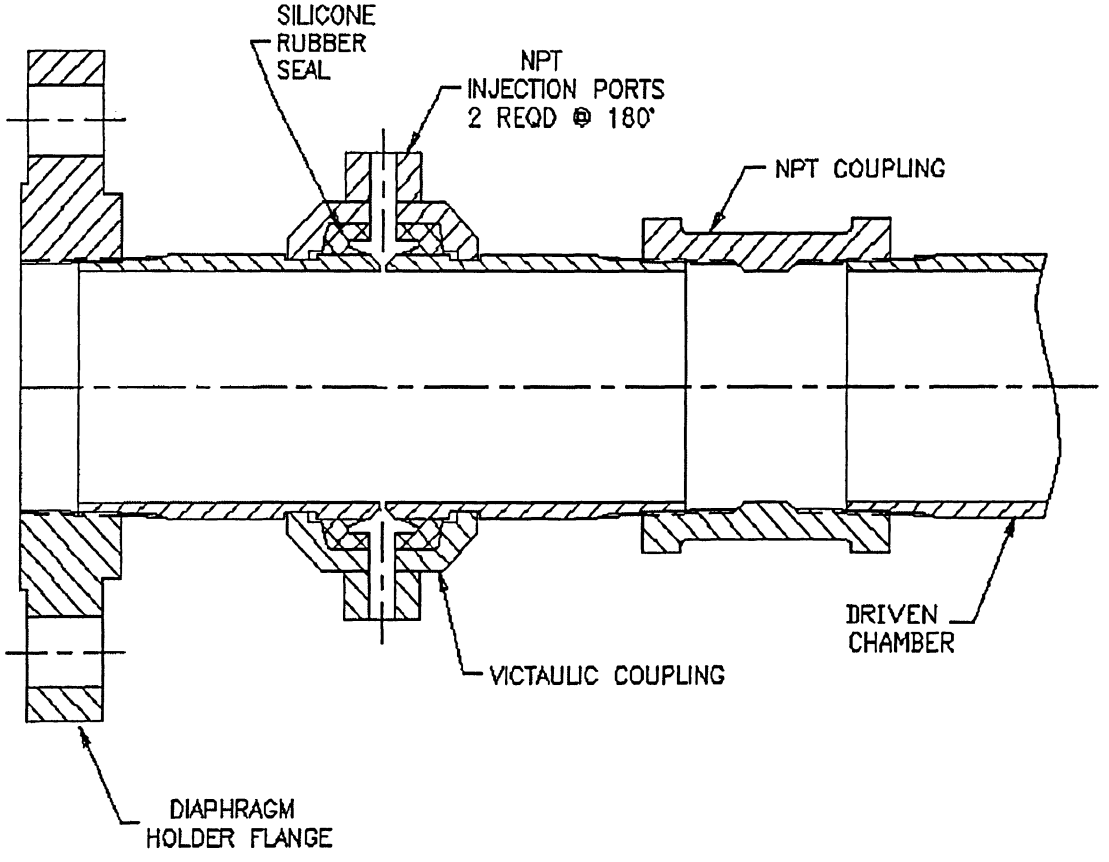

Figure 2.12. Primary air inlet assembly

The above-described procedure of pressurizing the driven chamber can be used as well for the nozzle case, the coupling being able to provide a steady inflow.

2.2.7 Measurements

Various measuring instruments, i.e., pressure gauges, pressure transducer, and thermocouples, can be attached at fixed positions in the wall of the shock tube. Required measurements can be easily taken at a desired time after the firing is initialized. The high

speed and the short duration of the flow necessitate that the measuring systems recording the pressure and the temperature should have a high frequency response.

It should be noted that the tappings in the shock tube wall allow measurements to be taken in the immediate vicinity of the measuring probe.

The range of the pressure gauges used in the apparatus is from 0 to 2200 kPa. Typical pressure and temperature taps used in the apparatus are shown in Fig. 2.13.

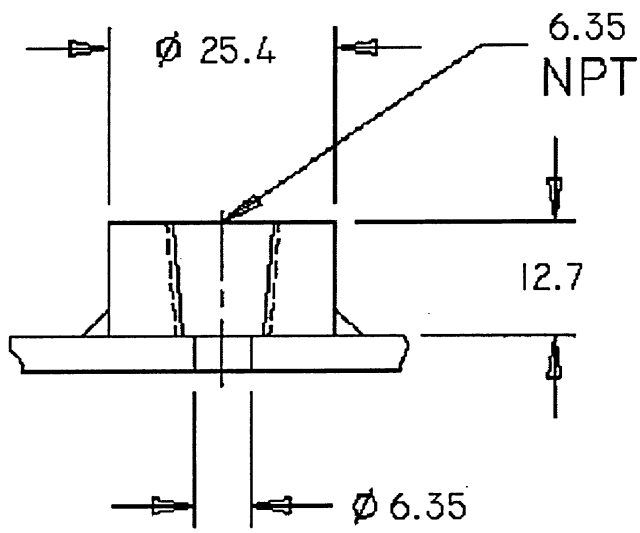

Figure 2.13. Pressure and temperature tap (all dimensions in mm)

2.2.8 Selecting a Transducer

Generally, strain gauges are a common choice for static pressure measurements. However, these gauges lack the frequency response necessary for the measurement of the high speed and short duration characteristics of a shock wave. A better-suited sensor for shock tube dynamic pressure measurements is a piezoelectric transducer. The natural frequency of such transducers depends on the particular crystal unit. In general, these transducers operate on the principle of change in the capacitance between two conducting plates generating charge in a piezoelectric crystal. The signal can then be conditioned and captured by an imaging oscilloscope or by a computer-based system.

In the present study, a high frequency, piezoelectric pressure transducer (manufactured by PCB PIEZOTRONICS Inc.) is used to measure the transient pressure in the shock tube. The transducer is a probe type, general-purpose quartz pressure sensor, made of stainless steel and hermetically sealed. It produces a high quality signal, which is independent of the cable length used for transmission of the signal. Specifications for the pressure transducer are listed below:[37]

1. Model number: 112A02
2. Serial number: 17993
3. Sensing element: quartz
4. Sensitivity: 0.000145 pC/Pa ($\pm$ 15%)
5. Resolution: 13.78 Pa
6. Measurement range: 689.5 kPa
7. Maximum pressure (static): 6895 kPa
8. Resonant frequency: up to 500 kHz
9. Rise time: $\leq$ 2 μs
10. Temperature range: -478 K to 478 K
11. Flash temperature: 1900 K
12. Capacitance: 18 pF
13. Insulation resistance at 294 K: $\geq 10^{12}$

In the current investigation, the transducer is mounted at 2.2 m from the diaphragm station, i.e., 10 cm upstream of the head end. Therefore, the transducer is quite close to the head-end/nozzle entrance region as required, and as soon as the incident shock arrives, the transient pressure is recorded in the present study. The transducer is screwed in a pressure transducer tap, which is different from the normal pressure taps. Such a tap is shown in Fig. 2.14.

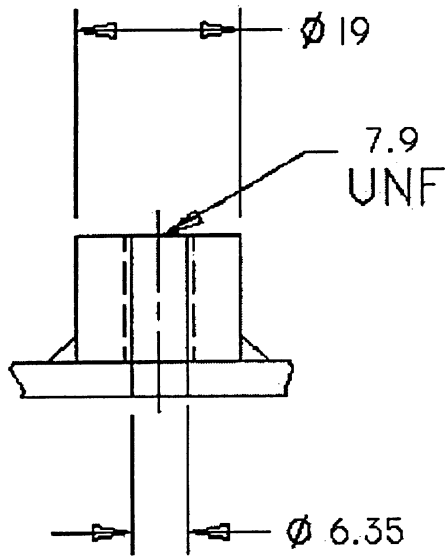

Figure 2.14. Pressure transducer tap (all dimensions in mm)

2.2.9 Data Acquisition

This section provides a description of components and method of recording pressure readings. The instrumentation for measuring the transient pressure in the shock tube is available in the Propulsion Research Facility (PRF at Room KHE128A at Ryerson University).

The pressure transducer is connected to a charge amplifier (converter) by means of a coaxial cable.[37] This amplifier converts sensor signals from the pressure transducer to voltage signals for transmission over long cables, and provides an interface to the data acquisition system. It is low in noise, powered by sensor signal conditioners, and installed in-line between the pressure sensor and signal conditioner. This charge amplifier is coupled to a sensor signal conditioner by means of another coaxial cable, which is connected to the data acquisition system. The sensor signal conditioner is a single channel system, with unity gain, and battery-powered.[37] It offers a portable, convenient method for powering sensors and conditioning their output signals for transmittal to readout and recording instruments, as in the present investigation.

The data acquisition system offers high resolution and high-speed signal capturing capabilities. This system enables the capture of analog and continuous signals measured by the sensor and modified by the signal conditioner, and it feeds a digital signal to a computer. In the present study, WaveBook, manufactured by IOtech Inc., is used as a high-speed data acquisition system. WaveBook has a 16-bit analog-to-digital resolution, 1 MHz analog-to-digital speed, 72 channels, and a sampling rate of up to 1 MHz.[34] The data sampling rate used for the present study is 500 kHz for a period of 20 ms.

WaveBook software includes WaveView,[38] a graphical Windows-based data acquisition program that enables one to acquire data for immediate viewing, or for storage on a desktop PC hard disk. The point-and-click interface simplifies the hardware set-up, without programming or connecting icons. The intuitive control automatically queries the WaveBook upon connection to the PC. Specific channel characteristics, such as gain, are automatically updated. The data collected by the WaveView are stored as a text file on the hard disk and can be easily exported to Microsoft Excel and then to SigmaPlot for preparing graphical results. A simple block diagram, shown in Fig. 2.15, is presented for a better understanding of the various connections in the data acquisition equipment.

2.2.10 Apparatus Assembly

In the previous sections, all the necessary components required for the experimental apparatus are described and discussed. The apparatus was assembled at the northeast corner of the aerodynamics laboratory (Room KHE33 at Ryerson University). Because the outlet air valve of the reservoir tank is at 0.6 m from the ground, a wooden table is used so that the whole assembly could be mounted on this table. The table is rigidly attached to the ground and various clamps were used to screw the apparatus to the table. The clamping was very rigid, so as to withstand the high-speed flow and high operating pressures. The driver (secondary) chamber is connected to the outlet valve for utilising air from the reservoir tank.

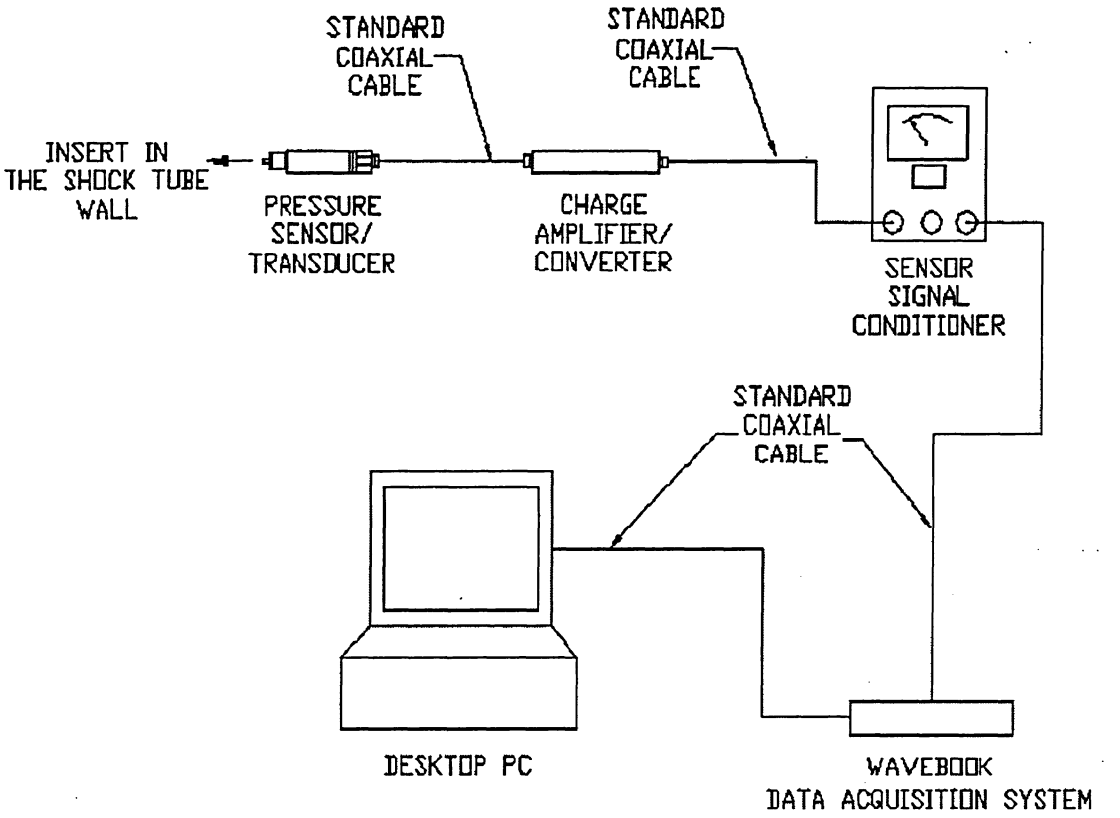

Figure 2.15. Data acquisition system – block diagram

The driven and driver chambers are cut to the required lengths and the diaphragm holder flanges are coupled to the chambers at one end. Pressure, temperature and transducer taps are available on both channel sections at the desired locations. The free end of the driver chamber is connected to the outlet valve of the reservoir tank through an isolation ball valve. The air supply to the driver chamber from the reservoir tank is connected at the boost pressure port.

At the other free end of the driven channel the head end (or nozzle) part is attached. The overhead air distribution line is connected to this chamber at the primary air inlet port. A diaphragm is loaded in the diaphragm holder and placed in the diaphragm flange. It is then screwed tightly with nuts and bolts, so as to avoid any air leakage.

The various pressure and temperature gauges are mounted on the respective taps. A panel having control valves to monitor the air supply to both chambers was secured permanently and labelled on a nearby cabinet. The complete assembly with all the necessary dimensions is shown in Fig. 2.16. It should be noted that the wooden table on which apparatus is mounted and the control panel having various pressure measuring gauges and valves to control air supply to both chambers and the data acquisition system are not shown in Fig. 2.16.

Once the design of the shock tube was completed and the apparatus was constructed, the assembly was thoroughly checked for air leakages, proper mounting of various gauges, leak-proof connections in piping, etc. The preliminary testing procedures are listed in Appendix A. A detailed list of procedures for operating the apparatus, conducting tests, and shutting down the apparatus is given in Appendix A.

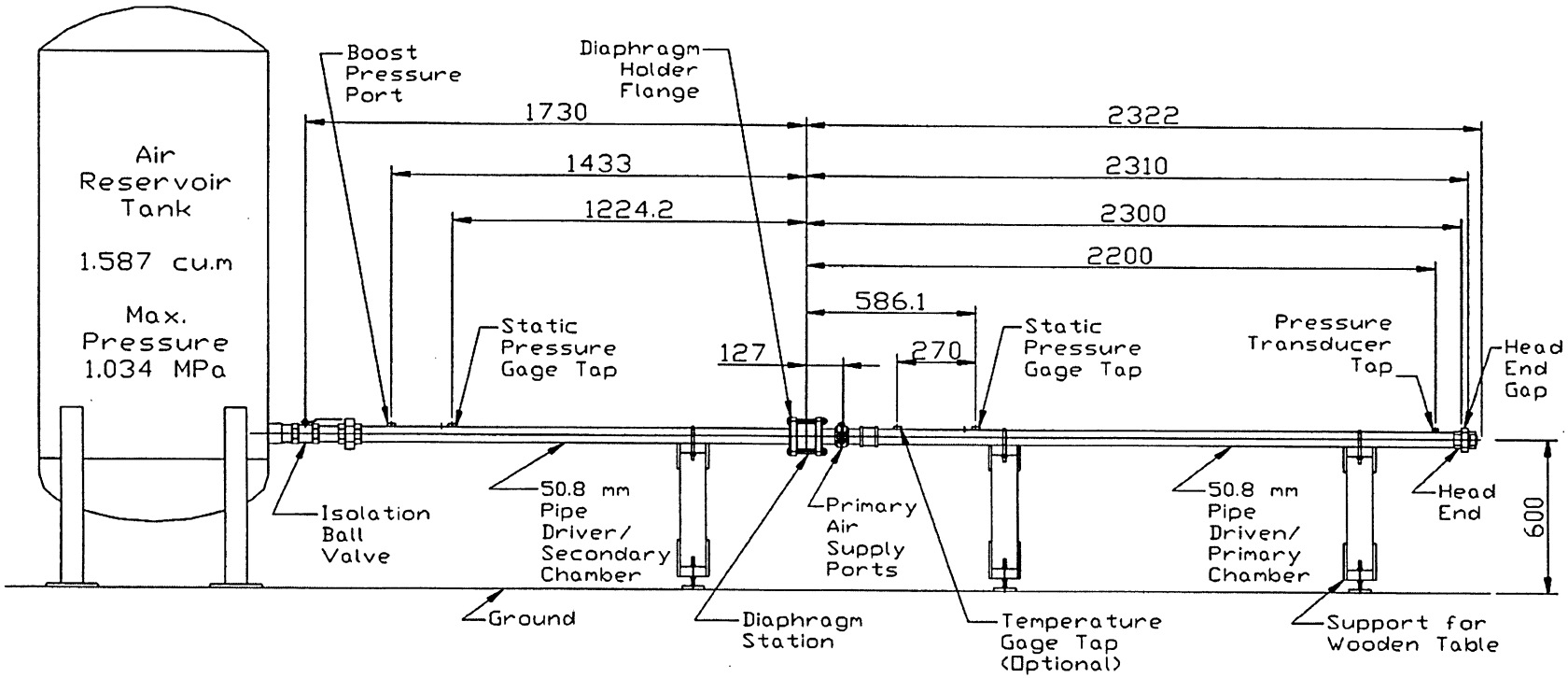

Figure 2.16. Cold-flow experimental apparatus

Chapter 3. Computational Fluid Dynamics (CFD) Study

The CFD analysis of the traveling shock wave interaction with the rocket motor head end, which yields various numerical flow simulation results, is done with the help of FLUENT 6.1. The following sections of this chapter provide an introduction to FLUENT software, its capabilities and its features. It is important to note that the numerical aspect of this investigation is not intended as a software validation exercise. The computational results provide insight that supplements the experimental data.

3.1 Introduction to FLUENT

FLUENT is a computer program for modeling fluid flow and heat transfer involving simple or complex geometries. FLUENT provides the capability for solving flow problems via a grid (i.e., a mesh) that is generated inside or around the flow domain of interest. There are several mesh types that are supported by FLUENT, including triangular, quadrilateral, tetrahedral, hexahedral, pyramid, and wedge shapes. These meshes may be high in density (fine) or low in density (coarse), depending on the required flow solution. This capability is useful for accurately predicting flow fields.

FLUENT is written in C computer language. True dynamic memory allocation, efficient data structures, and flexible solver control are the main features of this software. All functions required to compute a solution and display the results are accessible in FLUENT through an interactive, menu-driven interface. The FLUENT package used in the present study contains:

1. FLUENT, the solver.
2. GAMBIT, the pre-processor for geometry modeling and mesh generation.

One can create the flow model geometry and grid in GAMBIT. Once the grid has been generated and read into FLUENT, the FLUENT solver performs all the remaining operations. These operations include defining physical models and fluid properties, setting boundary conditions, executing the solution, refining the grid, viewing and post-

processing the results. The FLUENT solver has the following relevant modeling capabilities with respect to the current research:[39]

1. Flows in 2D or 3D geometries.
2. Incompressible or compressible flows.
3. Steady state or transient analysis.
4. Inviscid, laminar, and turbulent flows.

FLUENT is ideally suited for incompressible and compressible flow simulation in complex geometries. The software is capable of handling triangular and quadrilateral elements (or a combination of the two) in two dimensions, and tetrahedral, hexahedral, pyramid, and wedge elements (or a combination of these) in three dimensions. This flexibility allows one to pick mesh topologies that are best suited for a particular application. One can adapt all types of meshes in FLUENT in order to resolve large gradients in the flow field, but the initial mesh should always be generated outside the solver, using GAMBIT or any other CAD package for which the mesh import filters are available in FLUENT.

3.2 Preparation for CFD Analysis

Prior to starting to solve the problem in FLUENT, several aspects were considered. It was decided that a 2D axisymmetric flow model would be adequate to serve the present purpose. After that, the geometrical model was generated and meshed with structured quadrilateral cells in GAMBIT. The meshed density was then calibrated in going from a coarser grid to a finer grid, until the point when various pertinent flow parameters were not appreciably affected anymore by the grid density. The final grid cell geometry selected as a result of these test ~~the~~ numerical runs was a square cell with sides of 1-mm length.

Different numerical computational schemes and the process of collecting static pressure variations with time at specific locations were decided. Careful consideration of these key points will contribute to meaningful and successful results, and allow for a

better comparison to the experimental shock tube data. The following sections provide details of the analysis.

3.3 Procedural Steps for Solving Problem

After determining the important features of the problem, the following steps are followed to solve the problem:

1. Create a 2D axisymmetric model geometry and grid in GAMBIT.
2. Export the grid as a mesh file.
3. Start the appropriate solver for 2D modeling.
4. Import (i.e., read) the mesh file in FLUENT through a case file.
5. Check the grid and the grid scale.
6. Select the solver for solving the problem.
7. Choose the basic equations by specifying viscous and energy models.
8. Specify the material properties as air, ideal gas.
9. Specify the boundary conditions.
10. Define the custom field functions.
11. Define surface control points.
12. Adjust the solution control parameters (e.g., residual and surface monitors)
13. Initialize the flow field and patch the custom field functions.
14. Calculate the solution.
15. Display and examine the results.
16. Save the results as a data file.
17. If necessary, refine the grid or consider revisions to the numerical and physical model.

3.4 Inputs for CFD Analysis

This section describes the various input parameters for conducting the CFD analysis.

3.4.1 Model Construction

Since the experimental apparatus is symmetric about the x-axis, an axisymmetric model is used in FLUENT. A 2D axisymmetric model is generated in GAMBIT to represent the upper half of the experimental shock tube apparatus. The model has dimensions that correspond to the experimental apparatus (see Chapter 2). A schematic diagram is shown in Fig. 3.1.

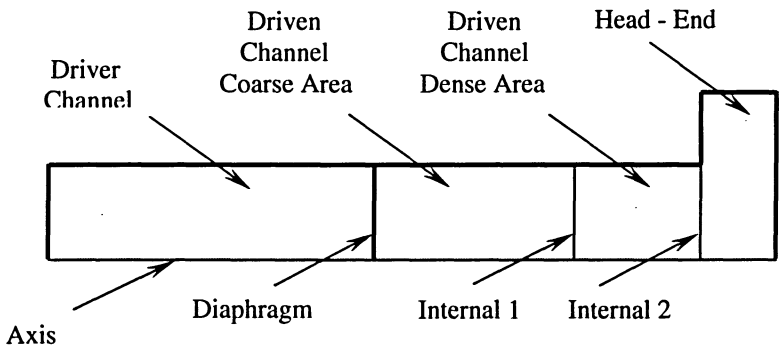

Figure 3.1. 2D axisymmetric model for CFD analysis (not to scale)

3.4.2 Grid Generation

After constructing the model, the next step is to generate a mesh in GAMBIT. The choice of grid depends largely on the type of flow to be modeled. Since the geometry is two-dimensional, the choice of grid cells is restricted to quadrilateral and triangular only. It is common practice to choose quadrilateral cells for simple geometries, in which the flow conforms to the geometry. Hence, for this particular study, quadrilateral cells are used.

The mesh to be generated should be of good quality and resolution so as to yield high accuracy and stability during numerical computations. Factors contributing to mesh quality are node point distribution, smoothness, and skewness. The flow characteristics

depend on the density and the distribution of nodes in the mesh. The grid in the head-end and the "driven channel dense" areas is shown in Fig. 3.2. It should be noted that the grid cell is a square with the length of 1 mm, as described previously.

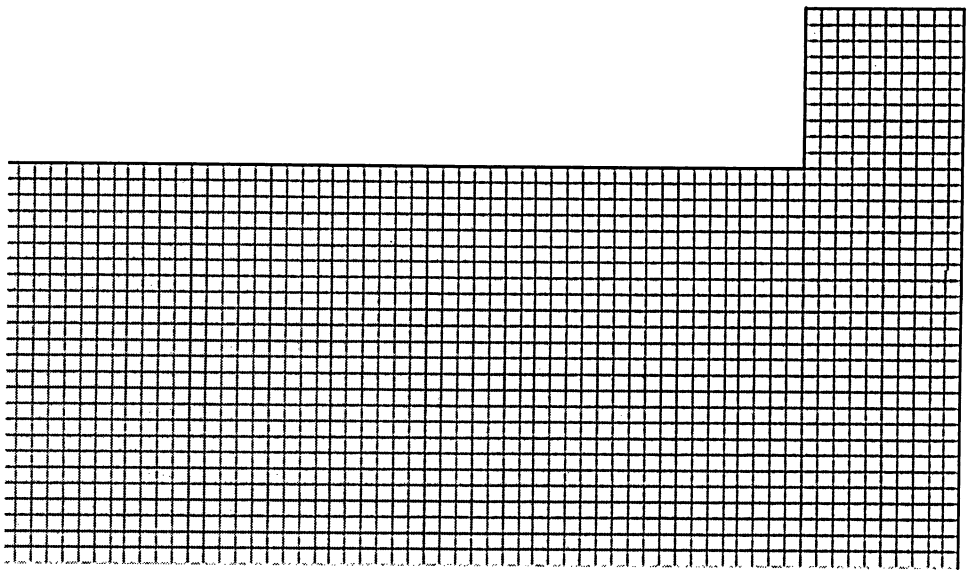

Figure 3.2. Grid in the head-end and "driven channel dense" areas
(enlarged view)

3.4.3 Exporting and Importing of Mesh

Once the model has been generated, faces are created through wire frame edges, various zones (i.e., regions) are defined (e.g., driver channel, driven channel coarse and fine mesh areas, and head-end region), different boundary types are defined (e.g., AXIS along the symmetry axis line, INTERNAL for the lines placed inside the shock tube, and WALL for the rest of the edges, including the diaphragm) and the geometry has been meshed; this information is then exported to FLUENT as a mesh file. This file contains the coordinates of all the nodes (i.e., vertices), connectivity information that tells FLUENT how the nodes are connected to one another to form edges, faces, and the zone types and numbers/names of all the faces. The file does not contain any boundary

conditions, flow parameters, or solution parameters. These characteristics are applied to the existing model in FLUENT.

The mesh file is imported/read directly into FLUENT through a case file (i.e., an input file whose format is understood by FLUENT and is used to read a mesh file). After reading a mesh file, the grid should be checked in FLUENT for possible errors. The area and volume statistics should always be positive; if they are found to be negative, the implication is that one or more cells have improper connectivity, and one should eliminate these negative values before starting the flow solution process. Simultaneously, grid size and scale should be verified.

3.4.4 Selection of Numerical Schemes

FLUENT provides two different solver formulations:[39]

1. Segregated solver
2. Coupled solver

Either method solves the governing equations for mass, momentum, and energy by means of a control-volume-based technique. This technique consists of the following:

(i) discretization, i.e., division of the entire domain into discrete control volumes and integration of the governing equations over these individual control volumes to construct algebraic equations for the dependent variables such as pressure, velocity, and temperature, etc.,

(ii) linearization of these algebraic equations, and

(iii) solution of the resulting linear equation system to determine new values of the dependent variables.

In the case of the segregated solver, the governing equations are solved sequentially (i.e., segregated from one another), whereas in case of the coupled solver, the governing equations are solved simultaneously (i.e., coupled together). Of these two

numerical methods, the coupled, second-order explicit solver is used for the present investigation.

The solution process for the particular numerical simulation of the shock tube flow application involves the modelling of a transient flow process, simulating the flow after the diaphragm is ruptured (i.e., the diaphragm boundary condition is set from "wall" to "internal" to initialize the flow) with the incident normal shock wave travelling downstream towards the head-end. A list of all the selected solution options is given below:

1. Solver: coupled
2. Formulation: explicit (2^{nd} order upwind)
3. Space: 2D axisymmetric
4. Time: unsteady
5. Energy solver
6. Viscous model
7. Time step: 1x 10^{-6} seconds

In addition to the above listed solution options, the present analysis includes the modeling of turbulence. FLUENT provides the following turbulence models:[39]

1. Spalart-Allmaras model
2. $k-\varepsilon$ models:
    a. Standard $k-\varepsilon$ model
    b. Renormalization-group (RNG) $k-\varepsilon$ model
    c. Realizable $k-\varepsilon$ model
3. $k-\omega$ models:
    a. Standard $k-\omega$ model
    b. Shear-stress transport (SST) $k-\omega$ model
4. Reynolds stress model (RSM)
5. Large eddy simulation (LES) model

Among the above models, the $k-\varepsilon$ (RNG) turbulence model was chosen for the present application. This model is quite simple and reliable for many practical engineering flow problems.

3.4.5 Physical Properties of Working Medium for FLUENT

One of the important steps in the set-up of the model is the defining of the physical properties of the material involved. In FLUENT, one defines the physical properties of fluids and solids as required. These properties are relevant to the modeling problem and generally include density, molecular weight, viscosity, heat capacity, thermal conductivity, mass diffusion coefficients, kinetic theory parameters, etc. A list of the reference properties for the present case, with air as the working medium, is given below:

1. Density: Ideal gas density
2. Specific heat at constant pressure: 1006.43 J/kg-K
3. Thermal conductivity: 0.0242 W/m-K
4. Dynamic Viscosity: 1.7894×10^{-5} kg/m-s
5. Molecular weight: 28.966 kg/kgmol

In FLUENT, the operating pressure can be absolute pressure or gauge pressure. Since it is necessary to use absolute pressure for high-speed compressible flows, for the present numerical study, the operating pressure is absolute. The final numerical results, presented in the "Results and Discussion" chapter, are converted in the gauge pressure scale in order to be shown in the same scale as the experimental results.

3.4.6 Boundary Conditions

Boundary conditions are applied for the flow at the boundaries of the model. Various boundary types are available in FLUENT such as mass flow inlet, pressure outlet, pressure far-field, outflow, wall, internal, axis etc. In Fig. 3.1, various edges are specified with appropriate boundary types. The boundary conditions for each edge are listed in Appendix D.

In addition, each centre axis segment is defined as an axisymmetric axis boundary type, the internal grid defined as an interior boundary type, each region having fluid as a fluid boundary type, and each wall as a wall boundary type.

It should be noted that initially, when the grid is imported in FLUENT as a mesh file, the diaphragm is considered as a wall boundary type (indicating that the diaphragm is not ruptured), and then, to initialize the transient flow, the diaphragm is considered as an interior boundary type (indicating that it is removed). During the current investigation, in the initial phases when the grid density and the associated solution accuracy were being assessed, another model set-up was defined using the diaphragm as a mass flow inlet boundary type acting as the lefthand boundary, to save on computational effort by not modelling the flow in the upstream driver channel. Once the desired grid density was determined, the approach using the mass flow inlet (i.e., only the driven section being studied, the shock wave strength being calculated and applied as the equivalent mass flow inlet boundary condition) was changed to the full model one (as shown in Fig. 3.1, both driver and driven channel flow being simulated).

3.4.7 Defining Custom Field Functions

Custom field functions are scalar functions defined by the user for initializing flow conditions, prior to beginning the flow solution process. These functions are patched to each zone/region (see Fig. 3.1) in terms of scalar values or in the form of a function. In

FLUENT, all the custom field functions are evaluated and stored in SI units; hence, care should be taken while entering these functions for analysis. A list of these functions is given in Appendix D.

3.4.8 Defining Solution Control Parameters

In FLUENT, the main control over time stepping is via the Courant Friedrichs Lewy (CFL) number, and the time step is proportional to the CFL requirement. In the present model, a CFL value of 0.75 was chosen for the shock wave interaction with the shock tube head-end, appreciably less than unity to conservatively ensure that all transient wave phenomena are captured. Based on the minimum grid size noted earlier and typical flow conditions for the runs, this CFL setting produced a time step on the order of 1 μs. The various solution control parameters are given in Appendix D.

3.4.9 Defining Monitors

Residual monitors are defined in order to check the solution convergence dynamically during the solution process. A residual for the coupled solvers is the time rate of change of any variable. One can print and plot the residual values for all relevant variables. For unsteady flows, one can monitor the elapsed time. FLUENT provides scaled and unscaled residual monitors. In general, it is difficult to judge convergence by examining the unscaled residual, since no scaling (i.e., no comparison with other residual values) is employed. However, in scaled residuals, scaling is done on the basis of residual values obtained from a certain number of iterations. These scaled residuals are useful indicators of solution convergence. Convergence criteria can be modified for each variable being monitored. The solution will stop automatically when each variable meets its specified convergence criterion. Variables to be monitored and checked for convergence are listed in Appendix D.

In addition to residual monitors, surface monitors are also defined in the model in order to record the static pressure at given locations as a function of time. In the model,

data are collected at 10 cm upstream of the head-end area (corresponding to the pressure transducer location in the experimental study) both at the wall and at the centre axis of the shock tube. Other four monitors are defined at 5 cm and 15 cm respectively from the head-end area, at the wall and at the centre axis. The parameter monitored at those six locations is the absolute pressure variation over the time. The area-weighted average for a given cell location is the means of data collection for the surface monitors. This information is stored in an output file. The output file can then be imported and analyzed using software such as Excel or SigmaPlot.

3.4.10 Convergence

In general, it is a good idea to judge convergence not only by examining residual levels, but also by monitoring relevant integrated quantities such as pressure, velocity, and temperature, etc. Generally, for a majority of flow problems, the convergence criterion is that the residual levels decrease to at least 10^{-3} (for the present work, conservatively, criteria are set substantially below this value). The convergence criterion for various equations is defined in Appendix D.

3.4.11 Transient Flow Calculations

The transient flow calculations are performed to describe time-dependent phenomena, including the capturing of the transient behaviour of a moving shock wave. Iterations are performed until a converged final solution for a given time step is obtained. The location of the moving incident shock wave can be visualized by displaying flow contour diagrams at a given time step. In the current investigation, any given time step should be a multiple of approximately $1x10^{-6}$ seconds. As noted in Section 3.4.9, the static pressure at various locations in the channel is monitored, to provide additional information.

3.4.12 Flow Contours and Results

A number of graphic tools are available in FLUENT, which allow processing of the information contained in the CFD solution and allowing one to easily view the results. One can generate graphic displays showing grids, contours, profiles, vectors, and path-lines. In FLUENT, one can also plot contour lines superimposed on the physical domain. Contour lines are lines of constant magnitude for a selected variable. It is possible to obtain colour-filled contours instead of default line contours, to specify the range of values to be contoured, to choose the portions of the grid to be displayed, and to store plots. One can also draw flow vectors in the entire domain or on selected surfaces. Each flow vector is drawn at the centre of the cell, with length and colour of the arrows representing the magnitude of the selected variable. Various flow contours for different head-end area set-ups (i.e., various head-end gap widths and depths) are presented throughout the "Results and Discussion" chapter. The flow contours and the absolute pressure variation over time obtained via the numerical simulation are not used as a validation exercise of the experimental data; they represent an important addition to the experimental investigation, offering an insight that supplements the data and yield a better understanding of the flow phenomena in the head-end area (i.e., head-end gap and upstream).

Chapter 4. Results and Discussion

4.1 Head End Reference Case

In meeting the objectives of this thesis, experimental and numerical studies were undertaken to examine various aspects pertaining to the interaction of an incident traveling shock wave with the shock tube head-end region (simulating the head-end area of a solid rocket motor). Both for the numerical and experimental investigations, the reference set-up involved the following parameters (described in Chapter 2):

- driver channel absolute pressure when diaphragm rupture occurs: 850 kPa
- driven channel absolute pressure when diaphragm rupture occurs: 375 kPa
- head-end gap width: 1 cm
- head-end gap depth: 1 cm
- gas temperature: 294 K

In the following sections, the key experimental and numerical results for the reference case are presented and discussed, while Appendix E provides a summary of all the key parameters discussed in the current chapter.

4.1.1 Experimental Results for the Reference Case

The experimental overpressure-time profile for the reference head-end geometry at a driven channel pressure of 375 kPa (absolute static pressure) is presented in Fig. 4.1. This pressure, before the arrival of the incident shock wave arising from the diaphragm rupture, is considered as the zero reference for the overpressure values in the graph. The pressure transducer, located at a specified position (i.e., 10 cm upstream of the head-end, at the wall), senses the pressure associated with the passage of this incident shock, and the data is transmitted via the charge amplifier to the acquisition system.

As soon as the travelling incident normal shock wave reaches the transducer location, the step change in pressure experienced by the transducer triggers it, and this instant of time becomes the origin of the time axis depicted in Fig. 4.1. One should note

that the time elapsed between the diaphragm rupture and pressure transducer trigger point is not recorded in the experimental analysis.

Analyzing the experimental pressure-time profile, it can be observed that the incident shock overpressure is on the order of 175 kPa. After passing the transducer position, the normal shock wave travels downstream and is reflected from the shock tube head-end. As can be seen from the figure, the reflected shock wave front passes the transducer location at $t \approx 0.6$ ms. This phenomenon appears as an initial spike in pressure (the spike being measured from the short-term mean pressure value at that time, if oscillations subsided, to the transient peak initial value), followed by a series of progressively decaying secondary oscillations, superimposed on the quasi-equilibrium base pressure of approximately 400 kPa.

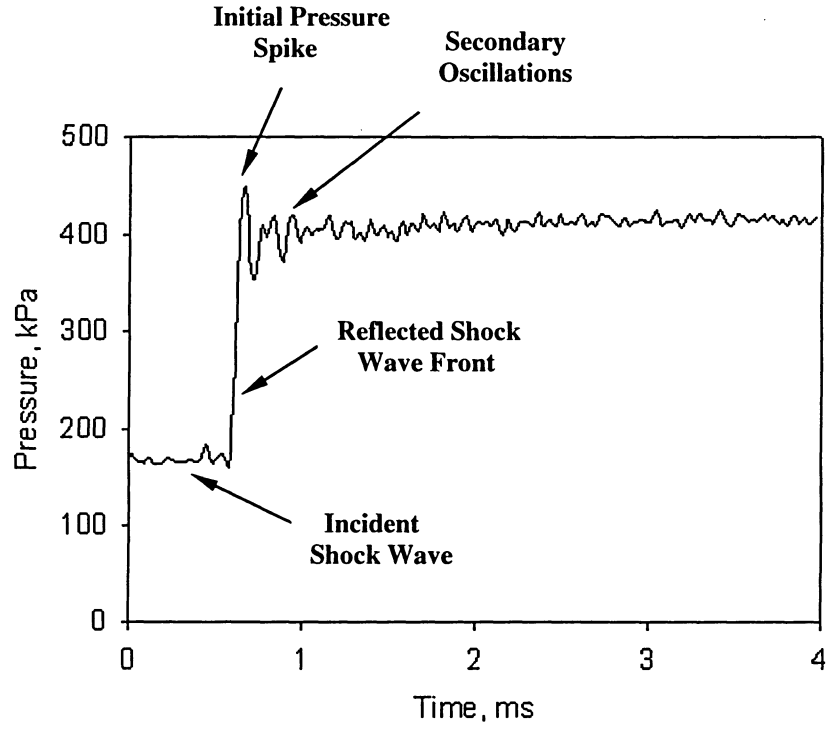

Figure 4.1. Experimental overpressure-time profile at the wall, 10 cm upstream (h.e. gap depth = 1 cm, width = 1 cm, p_1 = 375 kPa, p_4 = 850 kPa)

The incremental overpressure (i.e., the magnitude) of the initial pressure spike in Fig. 4.1 is on the order of 40 kPa, corresponding to about 10% of the reflected shock's base overpressure strength. The secondary oscillations appear to have a frequency that corresponds to the fundamental radial pressure wave frequency at that location of the chamber, which is given by:[1,23]

$$f_{1R} = 1.22\left(\frac{a_5}{d_1}\right) \tag{4.1}$$

where a_5 is the speed of sound in Region 5 (i.e., behind the reflected shock wave front, as described in Chapter 2) and d_1 is the channel diameter (5.08 cm).

From Chapter 2 (Equation 2.34), the reference Mach number of the reflected normal shock wave front is:

$$M_r = 1.179$$

and the temperature in Region 2 is:

$$T_2 = 329.8 \text{ K}$$

Using Equation 2.22, one can obtain the temperature behind the reflected shock wave (Region 5) and the local speed of sound:

$$T_5 = 366 \text{ K}$$

$$a_5 = \sqrt{\gamma R T_5} = 371.95 \text{ m/s}$$

Putting the above-specified numerical values in Equation (4.1), one determines:

$$f_{1R} = 1.22\left(\frac{371.95}{0.0508}\right) \approx 8.9 \text{ kHz}$$

Eventually, the radial wave loses its strength with each reflection in the transverse direction. Likely due to some flow variability combined with amplifier background noise, one does observe a continuation of some relatively low-level random bumpiness in the experimental pressure profiles.

4.1.2 Numerical Results for the Reference Case

Numerical simulations for the flow in the shock tube are generated via FLUENT and then data are imported and edited in SigmaPlot to be presented in the same format as

the experimental results. Initially, FLUENT provides all values of pressure (Y-axis of the chart) in the absolute scale, and they are subsequently changed to the overpressure values. In FLUENT, data are collected starting at time $t = 0$, corresponding to the initial diaphragm rupture. The X-axis (time axis) is then also adjusted, by re-initializing the time when the incident shock wave first passes the monitored location.

CFD simulation results are provided below for the reference head-end geometry at a driven channel absolute pressure of 375 kPa. In addition to the 10-cm upstream position (corresponding to the experimental transducer position), the static pressure is also collected at 5 cm and 15 cm upstream of the head-end. The static pressure both at the wall and at the centre axis of the shock tube is measured. This assists in determining any trends with regard to the radial wave activity occurring at different axial and transverse locations.

The pressure-time profile at the wall of the shock tube, 10 cm upstream of the head-end gap, is presented in Fig. 4.2. Prior to the reflected shock front's arrival, a small dip in pressure is observed at the monitor point, produced by an upstream-moving rarefaction wave arising from the incident shock passing through an expansion area (the gap, before meeting the head-end wall that produces the main reflected shock front). As the incident shock wave moves into the gap, it becomes more spherical in this region, and thus loses strength (i.e., continually drops in pressure during this phase) as it spreads out spherically; in order to conserve flow pressure conditions upstream of this activity, an upstream rarefaction wave is generated, and thus the appearance of the precursor pressure dip in the resulting profile. Conversely, when the incident shock front interacts with the head-end and surrounding gap upper walls, the resulting reflected shock front would be expected to gain strength as it moves back through the gap and converges as it enters into the upstream channel. In Fig. 4.2, the magnitude of the incident normal shock wave is on the order of 175 kPa, similar to the one observed in the experimental case (Fig. 4.1). Also, the value of the reflected shock's initial spike is approximately the same as that obtained for the experimental overpressure-time profile in Fig 4.1. Overall, the experimental and numerical profiles exhibit a similar value for the mean radial wave frequency, for the initial pressure spike, and for the follow-on secondary oscillations.

In addition to the pressure transducer location, results for locations 5 cm (Fig. 4.3) and 15 cm (Fig. 4.4) upstream of the head-end are also presented here. Analyzing these profiles, one can note that the incident and the quasi-equilibrium reflected shock wave pressure values are the same relative to values displayed in Fig. 4.2. The time necessary for the reflected shock wave to reach the monitored location varies from 0.4 ms in Fig. 4.3 to 1 ms in Fig. 4.4.

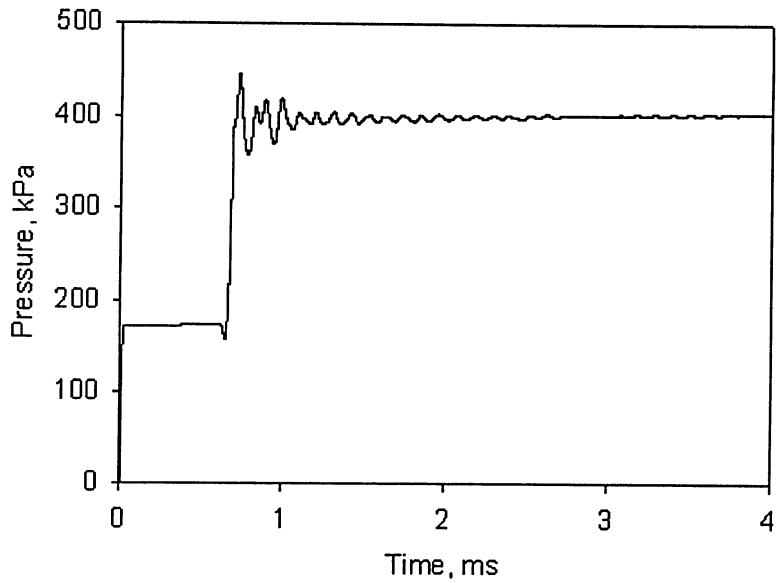

Figure 4.2. Numerical overpressure-time profile at the wall, 10 cm upstream (h.e. gap depth = 1 cm, width = 1 cm, p_1 = 375 kPa, p_4 = 850 kPa)

Comparing all of the above mentioned figures, it can be noted that the pressure dip in front of the reflected shock wave is more visible closer to the head-end location (5 cm upstream) than further upstream of the head-end gap (15 cm). This happens because the main reflected shock wave front (high-pressure; moving at a speed greater than the local speed of sound) has more time to catch up to the reflected precursor rarefaction pressure wave (low-pressure; moving at the local speed of sound) at the 15-cm position.

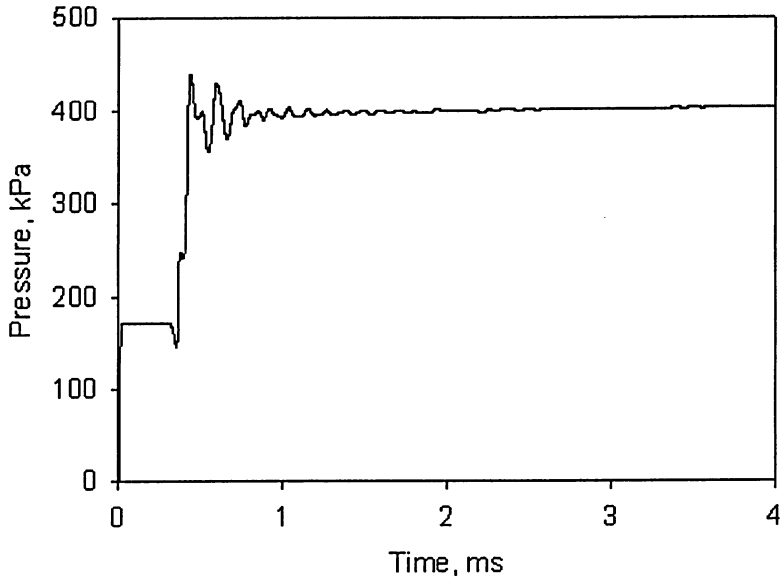

Figure 4.3. Numerical overpressure-time profile at the wall, 5 cm upstream (h.e. gap depth = 1 cm, width = 1 cm, p_1 = 375 kPa, p_4 = 850 kPa)

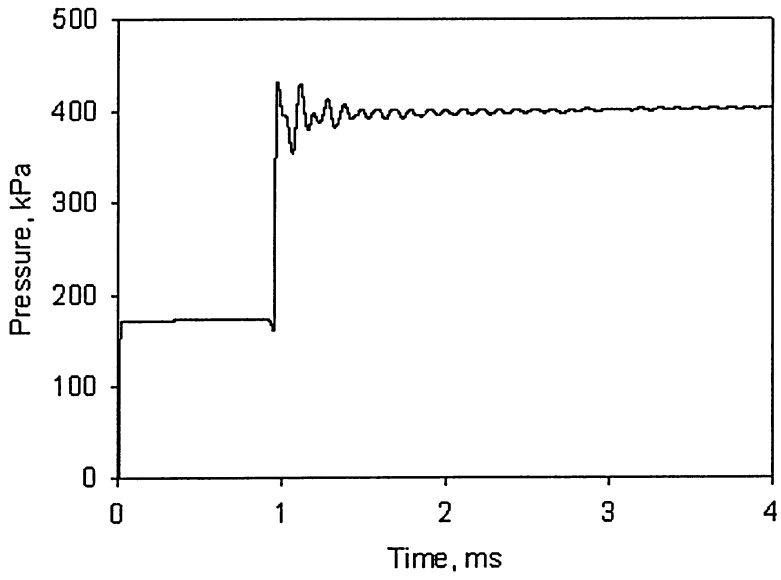

Figure 4.4. Numerical overpressure-time profile at the wall, 15 cm upstream (h.e. gap depth = 1 cm, width = 1 cm, p_1 = 375 kPa, p_4 = 850 kPa)

The value of the initial pressure spike has a variation at the wall of the shock tube from 50 kPa for the 5-cm position to 30 kPa for the 15-cm position. Although the initial pressure value is higher closer to the head-end gap, the secondary oscillations are more pronounced at the 15-cm location and they are present for a longer period of time. The mean radial wave frequency has values of 8.8 kHz at the 5-cm location and 9.5 kHz at the 15-cm upstream location, at the wall.

The predicted pressure at the centre axis of the shock tube, 10 cm upstream of the head-end gap, is shown in Fig. 4.5. While the pressure values of the incident shock wave and of the reflected main base (quasi-equilibrium) shock wave are the same as the ones at the wall of the shock tube (Fig. 4.2), the pressure spike and the secondary oscillations are stronger at the centre axis. The spike pressure increases from 40 kPa at the wall to around 85 kPa at the centre axis.

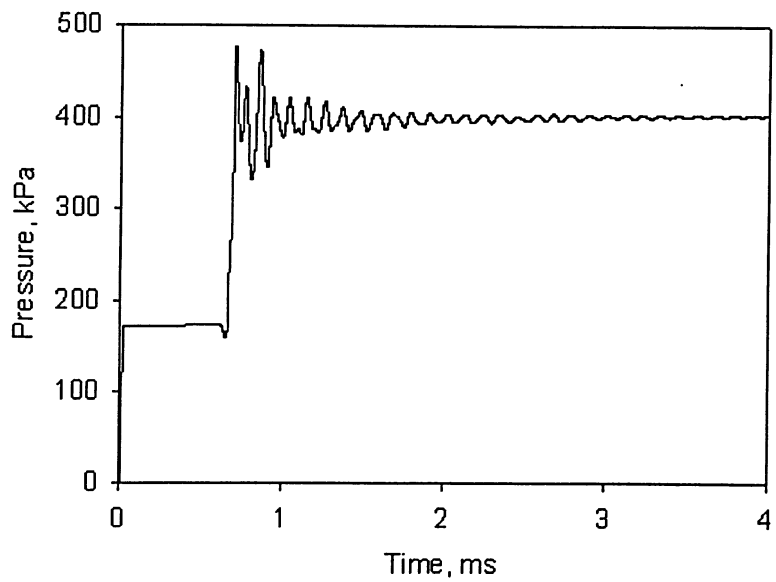

Figure 4.5. Numerical overpressure-time profile at the centre axis, 10 cm upstream (h.e. gap depth = 1 cm, width = 1 cm, p_1 = 375 kPa, p_4 = 850 kPa)

The secondary oscillations are of higher amplitude at the centre axis and therefore they are present for a longer period of time. In general, the radial activity is more pronounced at the centre axis of the shock tube than at the wall for the same distance

from the head-end gap. On the other hand, the mean radial wave frequency decreases when one moves from the wall (8.9 kHz) to the centre axis (8.5 kHz).

Variation of the radial wave activity occurring at the centre axis at different axial locations has been studied by monitoring locations 5 cm and 15 cm upstream of the head-end gap, in addition to the 10 cm location (shown in Fig. 4.5). Figures 4.6 and 4.7 depict the overpressure-time profiles for the 5 cm and 15 cm locations, respectively. Examining the centre axis results, one can observe a more visible variation over axial distance compared to the wall monitoring points.

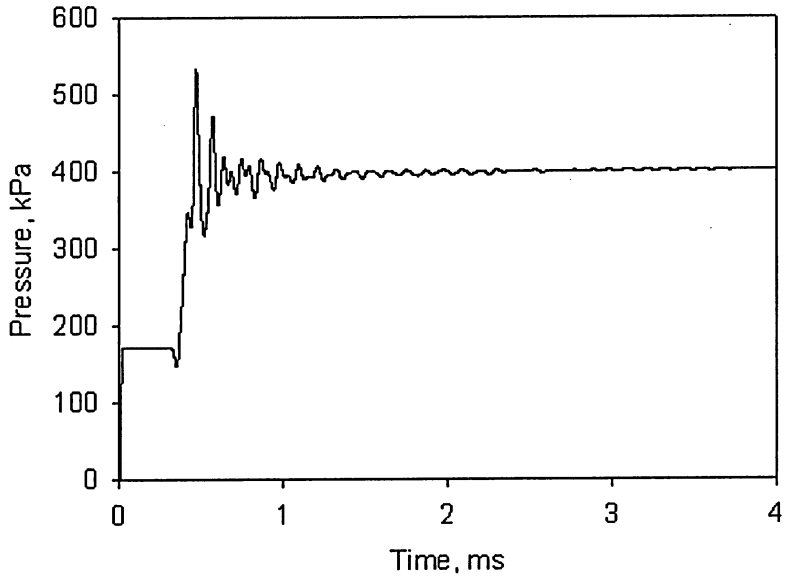

Figure 4.6. Numerical overpressure-time profile at the centre axis, 5 cm upstream (h.e. gap depth = 1 cm, width = 1 cm, p_1 = 375 kPa, p_4 = 850 kPa)

The initial pressure spikes vary from 140 kPa (Fig. 4.6) to 50 kPa (Fig. 4.7), with an intermediate value of 85 kPa at 10 cm upstream (Fig. 4.5). The secondary oscillations' behaviour can be ascertained as well. When closer to the head-end gap, the secondary oscillations decay quickly from the initial spike value, subsiding in approximately one millisecond (Fig. 4.6), while for a location farther from the head-end region, the secondary oscillations are present for a longer period of time (over 2 ms at 15 cm

upstream location). The mean radial wave frequency is higher at the 5 cm upstream position (9.2 Hz) than at 15 cm upstream (8.1 kHz).

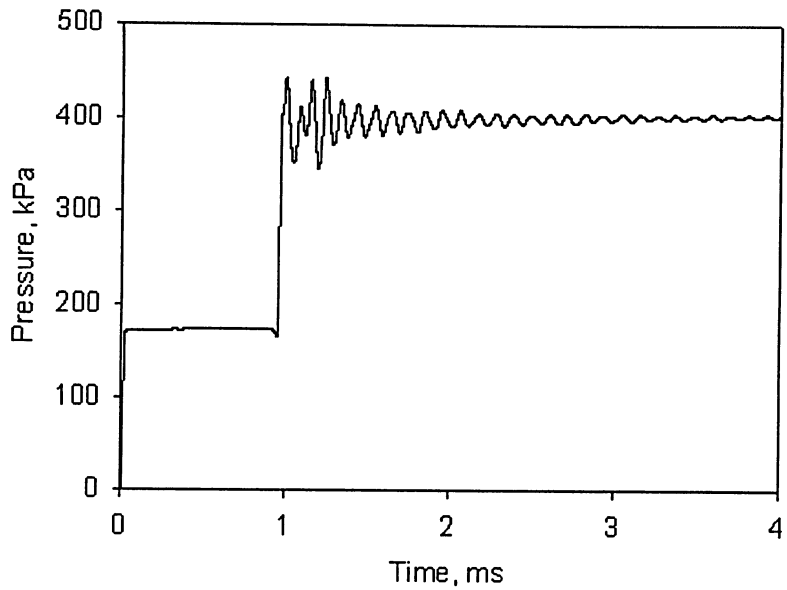

Figure 4.7. Numerical overpressure-time profile at the centre axis, 15 cm upstream (h.e. gap depth = 1 cm, width = 1 cm, p_1 = 375 kPa, p_4 = 850 kPa)

A better understanding of the phenomena surrounding the shock wave interaction can be achieved observing the static pressure contours at various moments of time. For example, Fig. 4.8 shows the absolute static pressure contours (in Pa) at t = 0.5 ms after passing the pressure transducer location. This moment corresponds to the beginning of the reflected shock wave's formation. One can also notice the low-pressure rarefaction wave moving upstream of the gap entrance, in front of the main reflected shock wave.

Fig. 4.9 shows the static pressure contours (in Pa) at t = 0.75 ms. The main reflected shock wave front is moving further upstream at this time, with considerable secondary wave motion evident behind the front. One can note the presence of a high-pressure pocket at the centre axis (dark red colour), concurring with earlier observations of higher initial pressure spike values here versus at the wall of the shock tube (as shown by the overpressure-time profiles).

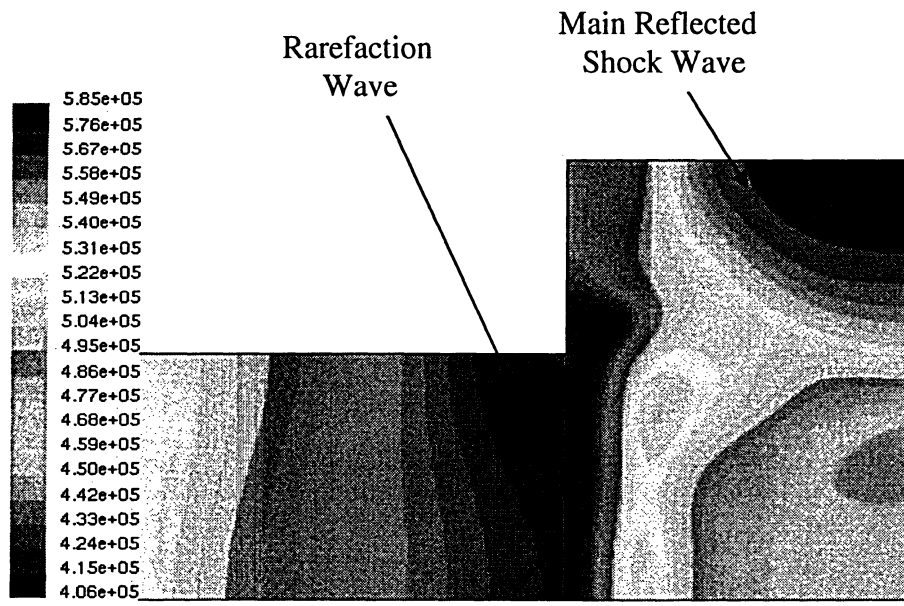

Figure 4.8. Static Pressure Contours (t = 0.5 ms), units in Pa

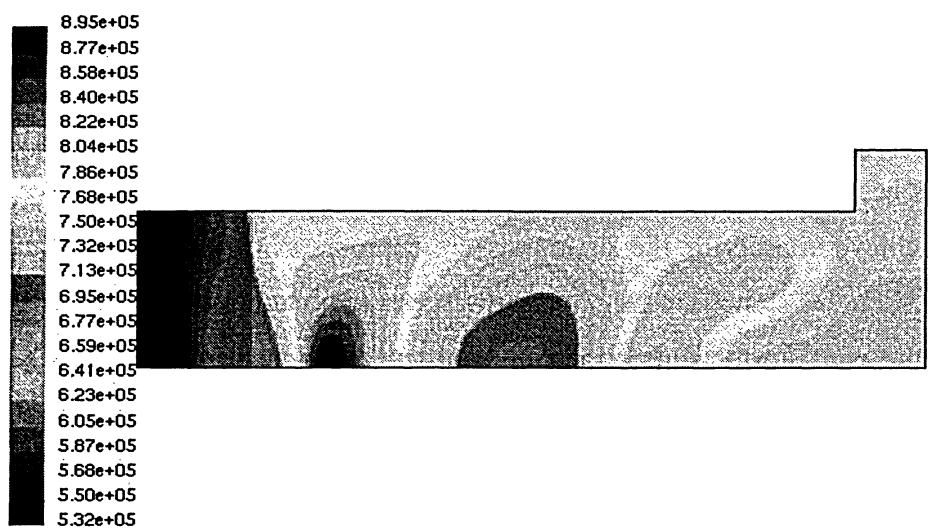

Figure 4.9. Static Pressure Contours (t = 0.5 ms), units in Pa

In general, the experimental and numerical analysis of the reference head-end gap geometry case has shown the existence of substantial transient radial wave development superimposed on the base reflected axial shock wave. In addition, the six monitored

points have helped in understanding the pressure variation with time at various locations of the shock tube. Both transversal (from centre axis to the wall) and axial (along the wall/centre axis) variation of flow properties with distance have been shown and discussed.

In the following subsections, various parameters that may affect the shock interaction behaviour are discussed further.

4.2. Head End Reference Model – Inviscid Case

A first sensitivity test carried out here involves the comparison between the viscous flow solution (presented in Chapter 4.1) and the inviscid solution, for the reference pressure and gap geometry. In both cases, after the diaphragm rupture, an incident normal shock wave, traveling downstream towards the head-end gap (Fig. 4.10), is generated. In the same time frame, expansion pressure waves can be seen in the driven channel (Fig. 4.11), advancing towards the shock tube reservoir end. The current parametric study focuses only on the interaction between the incident shock wave and the head-end of the shock tube, given that the rearward-moving expansion wave activity does not have a bearing on the present study.

Figure 4.10. Incident normal shock wave traveling towards the head-end gap, units in Pa

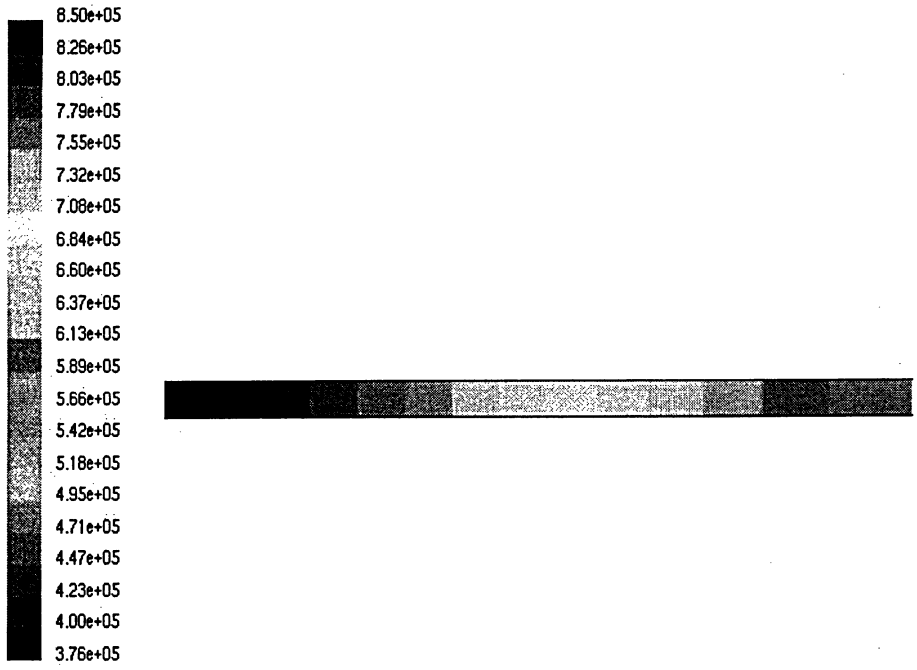

Figure 4.11. Expansion waves in the driver channel, units in Pa

In the inviscid case, the overpressure-time profiles are examined at the same monitor locations as in the viscous reference case. The results for the 10-cm upstream location, at the wall, are presented in Fig. 4.12. A comparison between Figs. 4.12 and 4.2 (viscous case at the same location) shows that the magnitude of the normal incident shock wave is on the order of 185 kPa for the inviscid case and only 175 kPa for the viscous model. This increase in the incident shock wave strength has a proportional effect on the reflected shock wave's quasi-equilibrium base pressure (410 kPa in the inviscid case) and on the initial pressure spike that is on the order of 65 kPa (inviscid case), compared to only 40 kPa in the viscous model. Excepting the described shift in pressure values noted above, the overpressure-time profiles appearance and the mean radial wave frequencies are similar in both inviscid and viscous cases.

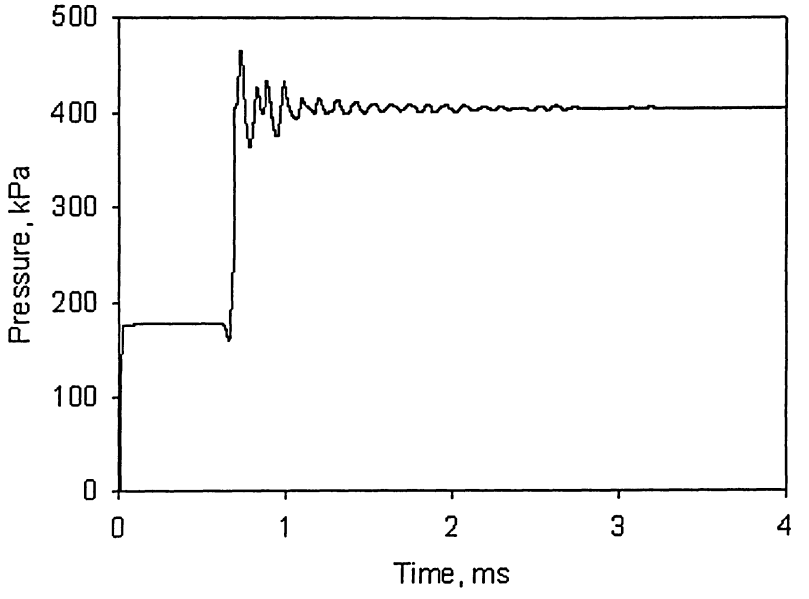

Figure 4.12. Numerical overpressure-time profile at the wall, 10 cm upstream (h.e. gap depth = 1 cm, width = 1 cm, p_1 = 375 kPa, p_4 = 850 kPa), inviscid case

The increased pressure values for the inviscid case are more obvious at the shock tube centre axis. Fig. 4.13 shows the overpressure-time profiles at 10-cm upstream of the head-end gap, at the centre axis. One can note the similarity with the viscous case (Fig. 4.5). The initial pressure spikes value increases from 85 kPa to almost 100 kPa.

The same trend can be observed at the 5-cm (Fig. 4.14) and 15-cm (Fig. 4.15) positions upstream of the head-end gap, at the centre axis. The initial spike, in the inviscid model, increases to 180 kPa and to 75 kPa (from 140 kPa in Fig. 4.6 and 50 kPa in Fig. 4.7), respectively.

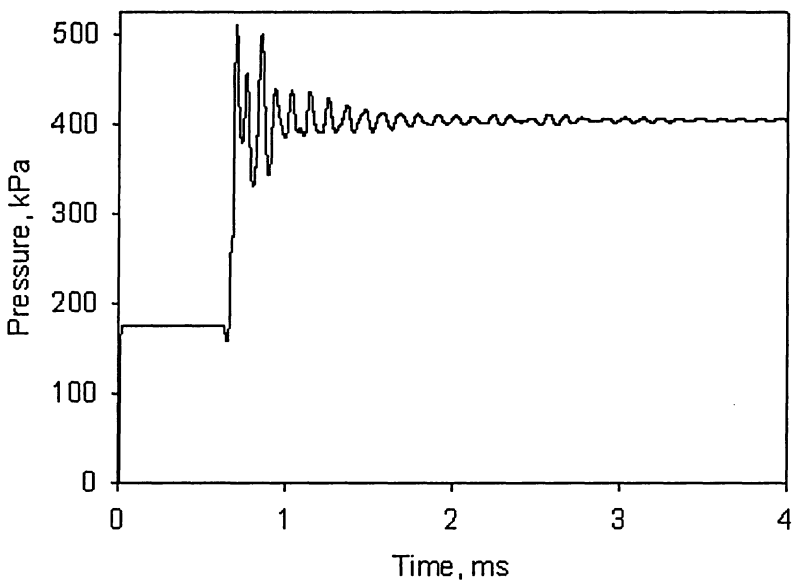

Figure 4.13. Numerical overpressure-time profile at the centre axis, 10 cm upstream (h.e. gap depth = 1 cm, width = 1 cm, p_1 = 375 kPa, p_4 = 850 kPa), inviscid case

Overall, in the inviscid case, the interaction between the traveling shock wave and the head-end of the shock tube displays very similar behaviour with that noted in the viscous reference case. The mean radial wave frequency remains the same at all monitored locations, and the overpressure-time profiles show a similar pressure distribution (although the inviscid profile is shifted in the positive direction of the pressure axis).

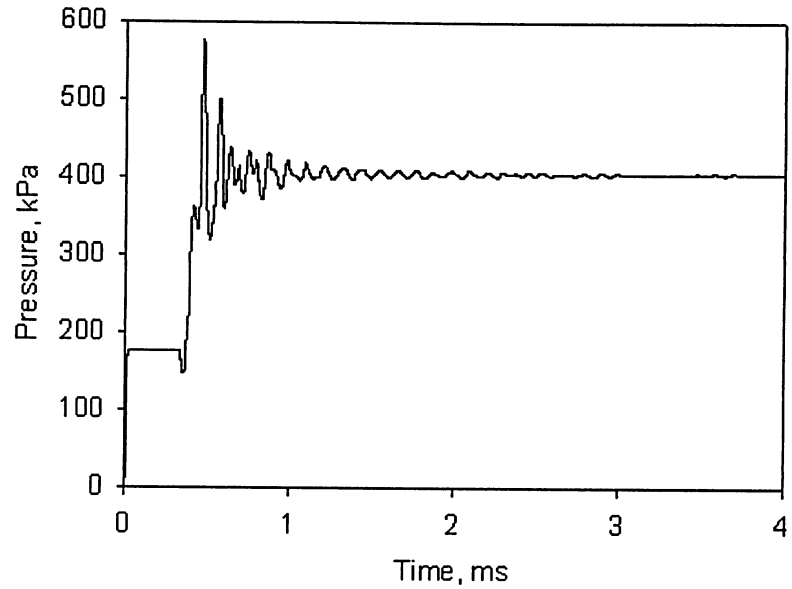

Figure 4.14. Numerical overpressure-time profile at the centre axis, 5 cm upstream (h.e. gap depth = 1 cm, width = 1 cm, p_1 = 375 kPa, p_4 = 850 kPa), inviscid case

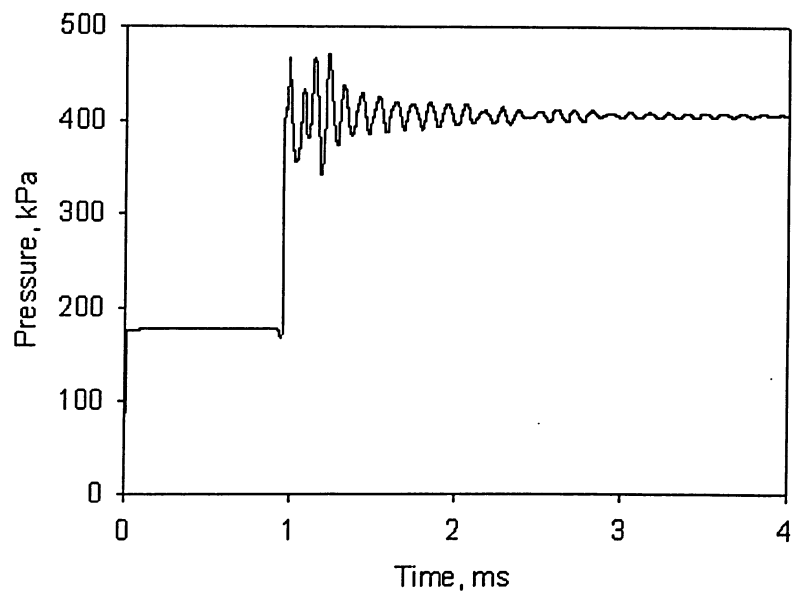

Figure 4.15. Numerical overpressure-time profile at the centre axis, 15 cm upstream (h.e. gap depth = 1 cm, width = 1 cm, p_1 = 375 kPa, p_4 = 850 kPa), inviscid case

4.3. Variable Head-End Gap Geometry

An objective of the current investigation is to determine the influence of the gap geometry on the initial pressure spike development, and on the secondary radial oscillations superimposed on the quasi-equilibrium reflected shock wave base pressure. In this evaluation, the head-end gap geometry is varied, while the initial driver and driven channel pressures are set as in the reference case. Therefore, the incident shock wave strength is the same, when it reaches the head-end gap region, as shown in Fig. 4.16. The subsequent shock wave interaction with the shock tube head-end is influenced by the width and depth of the head-end gap.

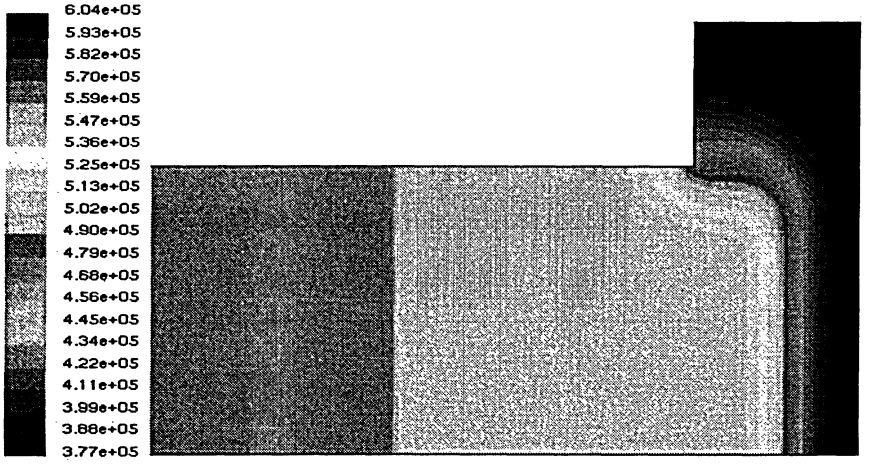

Figure 4.16. Incident shock wave reaching the head-end gap region, units in Pa

4.3.1 Influence of Head-End Gap Width

The first factor studied is the head-end gap width influence. The width has been changed from 0 cm (no gap) up to 3 cm, while the head-end gap depth was kept constant to 1 cm. Numerical results are presented for the following cases: 0 cm, 0.5 cm, 1.5 cm, and 3 cm gap width. The experimental firings are limited, as described in Chapter 2, to up

to a 1-cm gap width. Therefore, only experimental results of the 0 cm (no gap) and 0.5 cm set-up cases are discussed in this section.

Figs. 4.17 and 4.18 show the numerical results for the 0 cm case (i.e., no head-end gap is present at the shock tube end region). Fig. 4.17 shows the overpressure-time profile at the shock tube wall, 10 cm upstream of the head-end, while Fig. 4.18 depicts the pressure distribution over time, corresponding to the 10-cm location, at the centre axis.

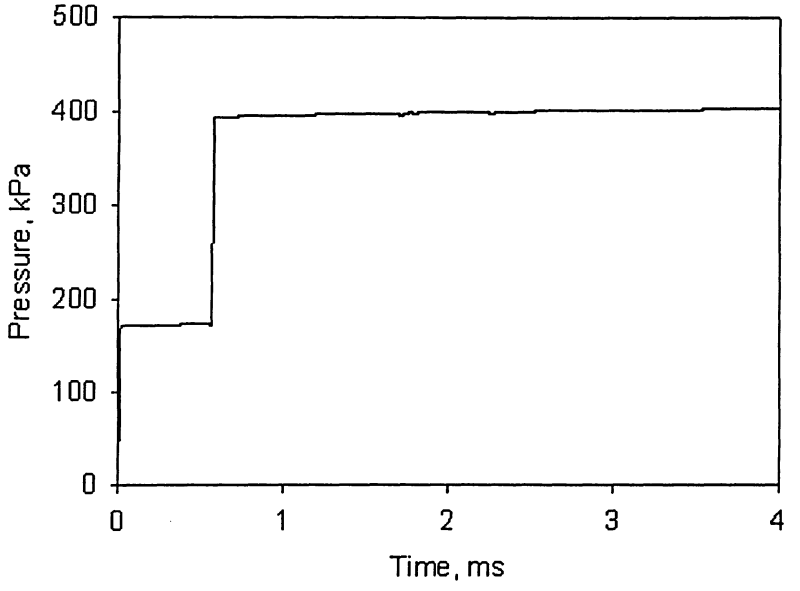

Figure 4.17. Numerical overpressure-time profile at the wall, 10 cm upstream (no head-end gap, p_1 = 375 kPa, p_4 = 850 kPa)

One can observe that the static pressure profiles are the same at the centre axis and at the wall of the shock tube. The incident shock wave overpressure is on the order of 175 kPa and the reflected shock wave overpressure is around 400 kPa. These values are the same as in the reference case but, without the existence of a gap in the head-end region, one can note that the initial pressure spike and the secondary radial oscillations are not present anymore. This model (no gap) is very close to the one described in the one-dimensional shock tube theory (Chapter 2). In reality, the existence of a head-end gap will generate secondary radial oscillations that the one-dimensional theory doesn't account for.

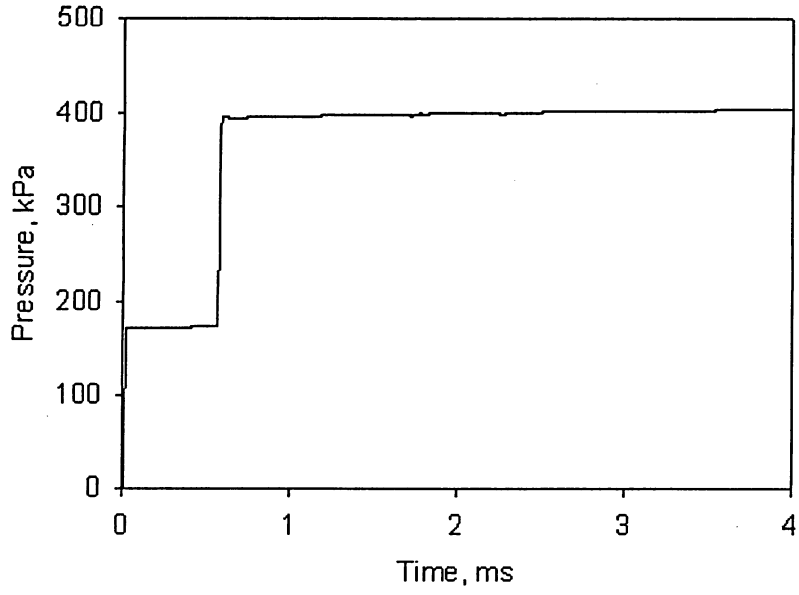

Figure 4.18. Numerical overpressure-time profile at the centre axis, 10 cm upstream (no head-end gap, p_1 = 375 kPa, p_4 = 850 kPa)

In Fig. 4.19 the experimental overpressure-time profile for the 0-cm head-end gap, at the wall, 10 cm upstream of the head-end wall is presented. The experimental profile shows a very similar behaviour for the incident and reflected shock waves as noted in the numerical profiles. As described in the reference case study, one can note the presence of relatively low-level random bumpiness in the experimental profile, likely generated by some flow variability combined with amplifier background noise. However, it is obvious that there is no substantial initial pressure spike at the beginning of the reflected shock wave front.

The experimental overpressure-time profile at the wall, 10-cm upstream of the head-end gap and a gap width of 0.5 cm (depth of 1 cm), is shown in Fig. 4.20. The incremental overpressure of the initial pressure spike is on the order of 50 kPa, a value comparable with the reference case (with a width of 1 cm). This shows that even the presence of a small gap at the shock tube end will generate substantial secondary radial oscillations superimposed on the main reflected shock wave.

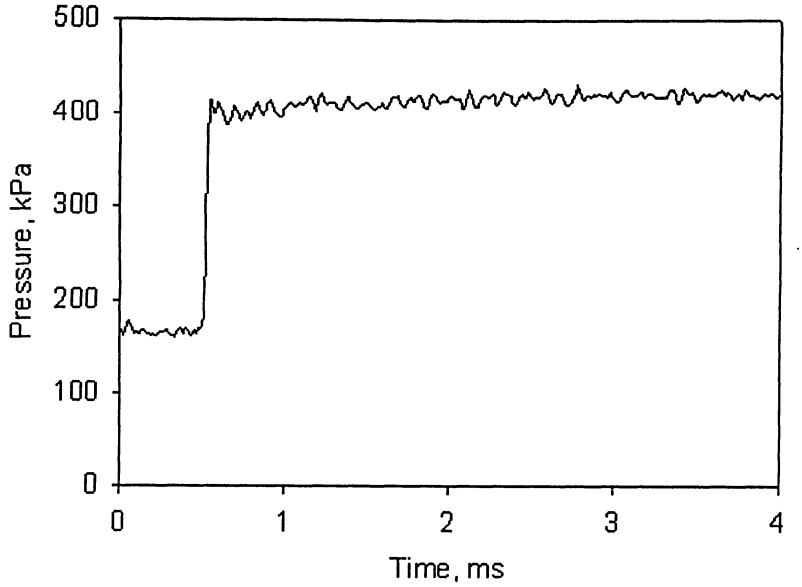

Figure 4.19 Experimental overpressure-time profile at the wall, 10 cm upstream (no head-end gap, p_1 = 375 kPa, p_4 = 850 kPa)

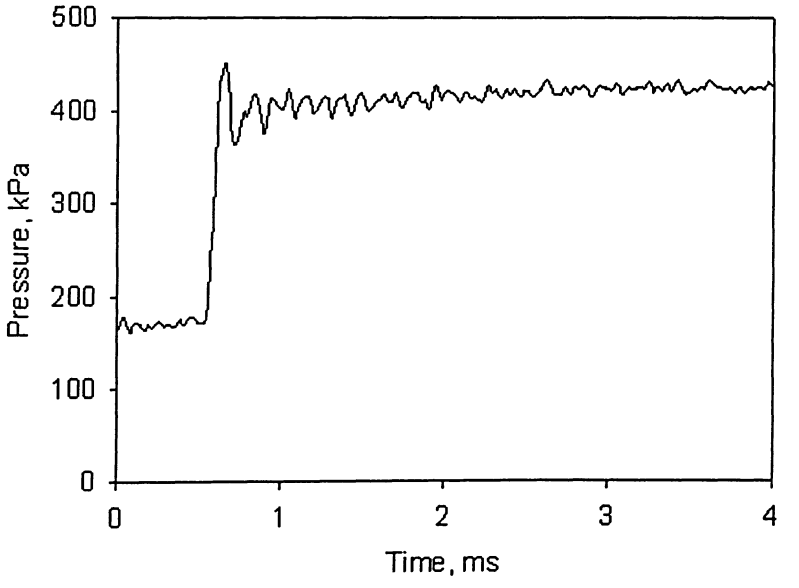

Figure 4.20. Experimental overpressure-time profile at the wall, 10 cm upstream (h.e. gap depth = 1 cm, width = 0.5 cm, p_1 = 375 kPa, p_4 = 850 kPa)

The corresponding numerical profile is shown in Fig. 4.21. As observed in the experimental profile, the initial spike is on the order of 50 kPa and the secondary oscillation have a frequency of 9 kHz, close to the reference case value observed at the same monitored location.

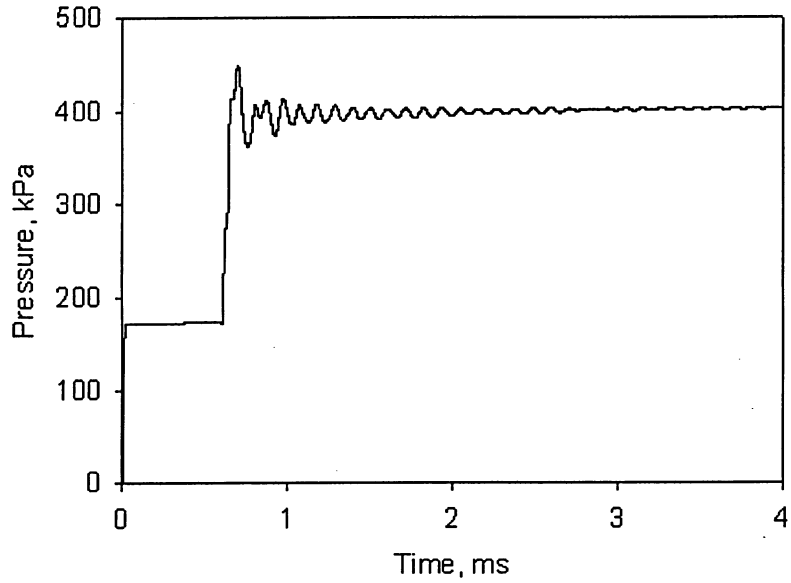

Figure 4.21. Numerical overpressure-time profile at the wall, 10 cm upstream (h.e. gap depth = 1 cm, width = 0.5 cm, p_1 = 375 kPa, p_4 = 850 kPa)

Figs. 4.22, 4.23, and 4.24 depict the numerical overpressure-time profiles at the centre axis of the shock tube, for the 10-cm, 5-cm, and 15-cm locations, respectively. Analyzing Fig. 4.22, one can note that the initial pressure spike is around 95 kPa, higher than the one observed in the reference case (85 kPa), and the secondary oscillations are also a little stronger with a frequency of 8.7 kHz.

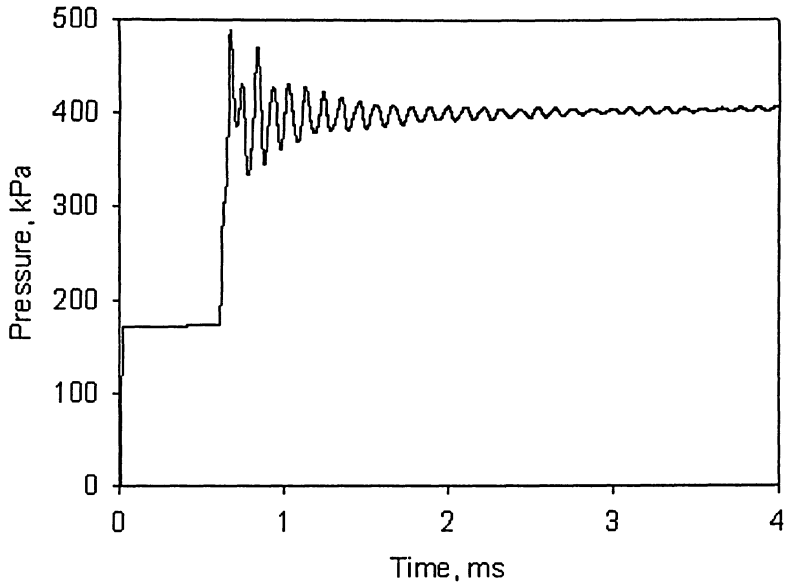

Figure 4.22. Numerical overpressure-time profile at the centre axis, 10 cm upstream (h.e. gap depth = 1 cm, width = 0.5 cm, p_1 = 375 kPa, p_4 = 850 kPa)

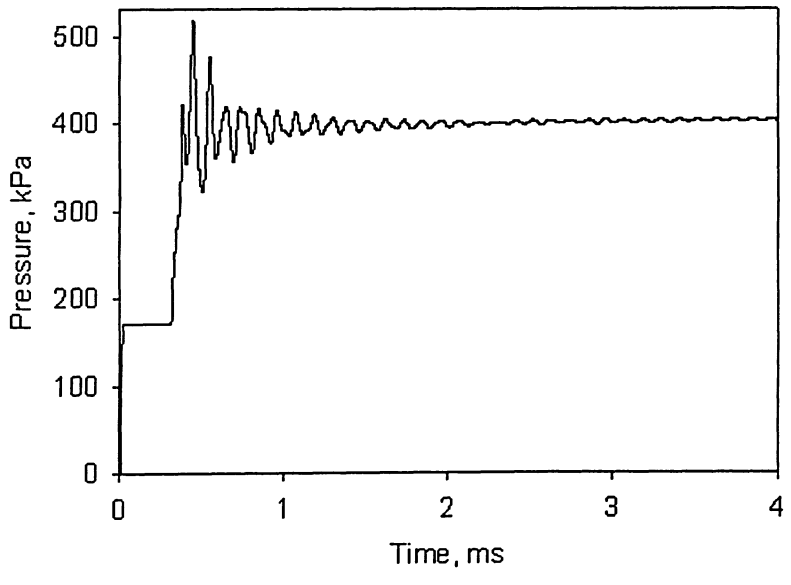

Figure 4.23. Numerical overpressure-time profile at the centre axis, 5 cm upstream (h.e. gap depth = 1 cm, width = 0.5 cm, p_1 = 375 kPa, p_4 = 850 kPa)

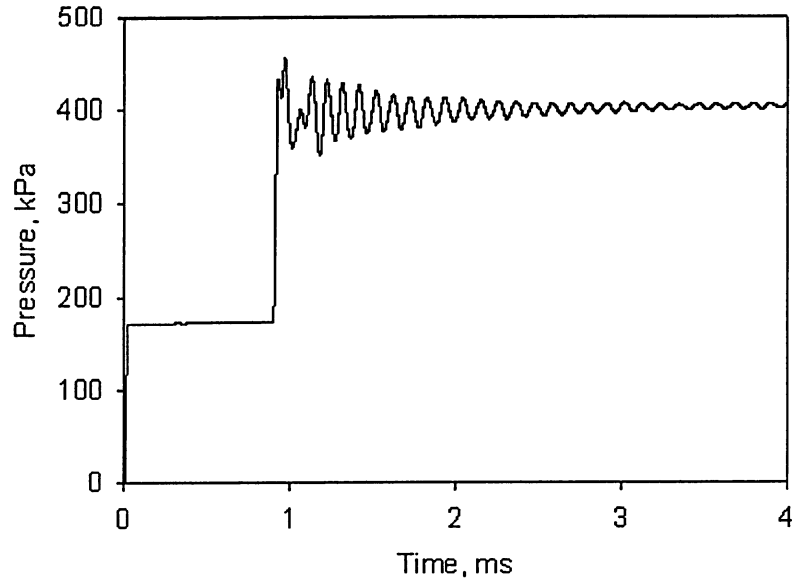

Figure 4.24. Numerical overpressure-time profile at the centre axis, 15 cm upstream (h.e. gap depth = 1 cm, width = 0.5 cm, p_1 = 375 kPa, p_4 = 850 kPa)

A similar variation of the initial pressure spike is observed at the other monitored locations, at the centre axis: 5 cm (Fig. 4.23) and 15 cm (Fig. 4.24) upstream. Closer to the head-end region, the initial pressure spike is 120 kPa, while at the 15-cm location it is only 60 kPa. The secondary radial oscillations have frequencies of 9 kHz and 8.2 kHz, respectively. One should note that in all the overpressure-time profiles shown for a gap width of 0.5 cm, the small dip in the front of the main reflected shock wave front (observed in the reference case) is not present anymore. With the width of the gap only half of the depth of the head-end gap, the reflected shock wave more quickly overtakes the precursor rarefaction wave.

Overall, the data analysis for the head-end gap with a width of 0.5 cm shows that the initial pressure spike and the secondary oscillations have a similar behaviour to that observed in the reference case. The amplitude of the secondary oscillations is slightly higher for the 0.5 cm gap width than the 1 cm gap width. Further increasing the gap width will show a decrease in the initial pressure spike and an increase in the pressure dip in front of the main reflected shock wave.

Although the experimental apparatus is limited to firings up to a 1-cm head-end gap width, it is necessary, for a complete understanding of the gap width influence on the shock wave interaction with the rocket motor head-end, to analyze overpressure-time profiles for gaps having widths greater than 1 cm.

Fig. 4.25 depicts the overpressure-time profile for a gap width of 1.5 cm, at the 10-cm location, at the wall of the shock tube. The initial pressure spike is only 15 kPa (compared to 40 kPa for the reference case) and the radial oscillations' frequency is around 8.1 kHz.

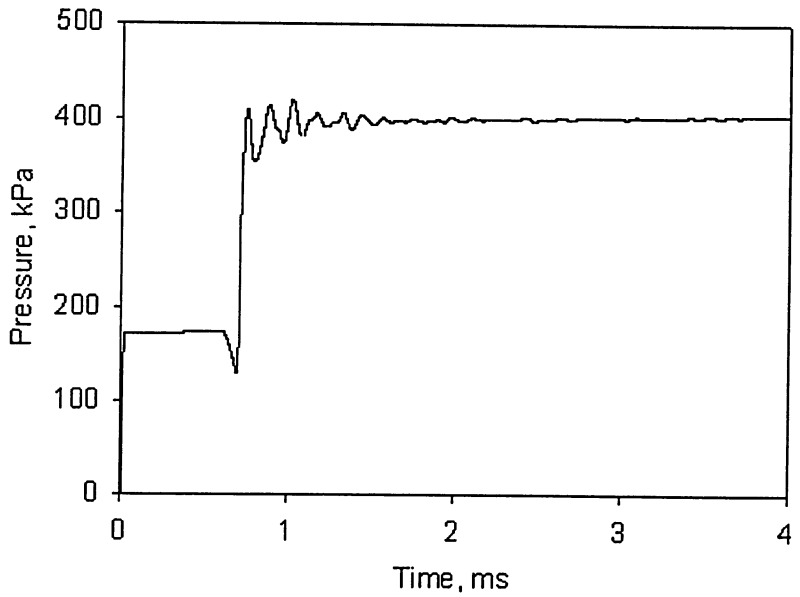

Figure 4.25. Numerical overpressure-time profile at the wall, 10 cm upstream (h.e. gap depth = 1 cm, width = 1.5 cm, p_1 = 375 kPa, p_4 = 850 kPa)

In Figs. 4.26, 4.27, and 4.28, the overpressure-time profiles, for the head-end gap width of 1.5 cm, are shown at 5-cm, 10-cm, and 15-cm at the centre axis locations, respectively. The pressure dip in front of the main reflected shock increases for higher gap widths; one can observe the pressure dip values varying from 50 kPa (measured from the incident shock wave's base pressure value) for the 5-cm location to 10 kPa for the 15-cm location. This phenomenon depends on the period of time necessary to the main reflected shock wave to catch up to the reflected precursor rarefaction pressure wave.

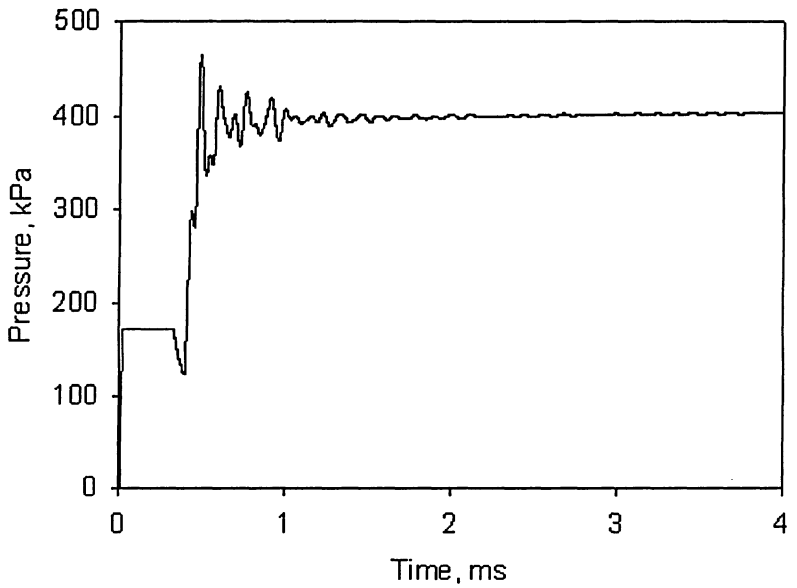

Figure 4.26. Numerical overpressure-time profile at the centre axis, 5 cm upstream (h.e. gap depth = 1 cm, width = 1.5 cm, p_1 = 375 kPa, p_4 = 850 kPa)

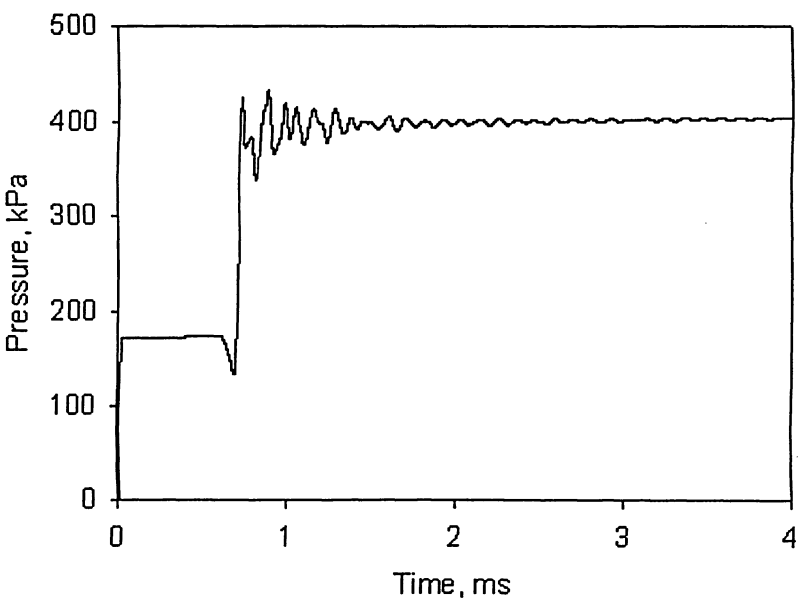

Figure 4.27. Numerical overpressure-time profile at the centre axis, 10 cm upstream (h.e. gap depth = 1 cm, width = 1.5 cm, p_1 = 375 kPa, p_4 = 850 kPa)

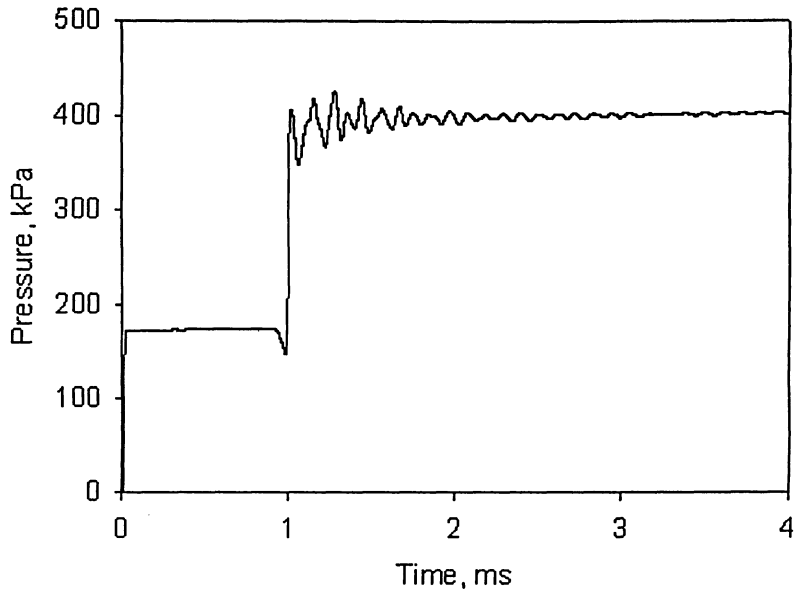

Figure 4.28. Numerical overpressure-time profile at the centre axis, 15 cm upstream (h.e. gap depth = 1 cm, width = 1.5 cm, p_1 = 375 kPa, p_4 = 850 kPa)

Examining the results for a gap width of 1.5 cm, one can note a substantial decrease, compared to the reference case, in the initial pressure spike at all monitored locations. These values vary from 80 kPa (Fig. 4.26) to 15 kPa (Fig. 4.28). On the other hand, the secondary oscillation frequencies remain comparable to the ones noted in the reference case. They range from 8.5 kHz for the 5-cm location to 9.2 kHz for the 15-cm location.

The gap width can be further increased to 3 cm. Numerical results at the wall of the shock tube for the 10-cm upstream location are presented in Fig. 4. 29. The pressure dip in front of the reflected shock wave has a value of 75 kPa and the initial pressure spike decreases, the spike being below the eventual base pressure value. The secondary pressure oscillations, although of lower amplitude, are present for a relatively long period of time and seem to have a frequency comparable to the one shown in the overpressure-time profile of the reference case, at the same location.

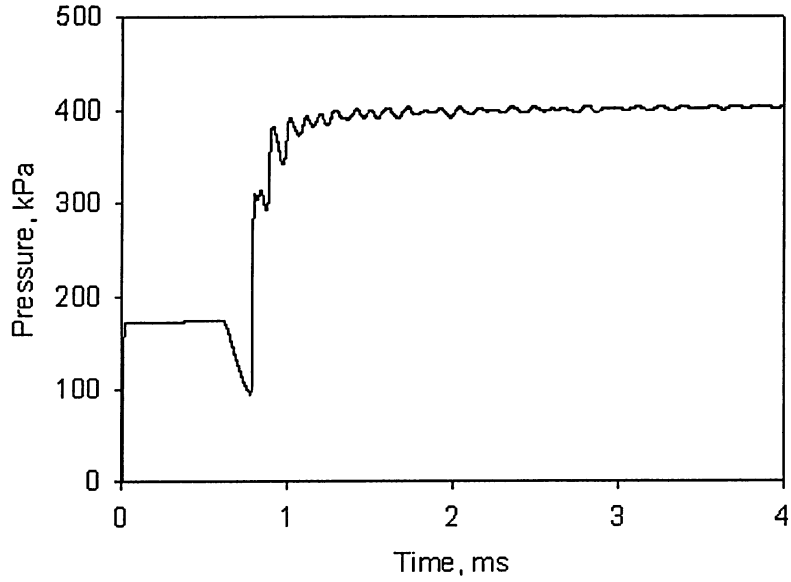

Figure 4.29. Numerical overpressure-time profile at the wall, 10 cm upstream (h.e. gap depth = 1 cm, width = 3 cm, p_1 = 375 kPa, p_4 = 850 kPa)

In Figs. 4.30 to 4.32, the overpressure-time profiles, at the centre axis of the shock tube, for the monitored locations (i.e., 5-cm, 10-cm, and 15-cm points upstream of the head-end gap) are presented. The pressure dip in front of the reflected shock wave ranges from 80 kPa at the 5-cm location to 65 kPa at the 15-cm location, with a value of 75 kPa at the 10-cm upstream location.

The initial pressure when the reflected shock wave passes the monitored locations is well below the eventual base pressure of 400 kPa. The smallest value of the initial pressure is recorded at the nearest location to the head-end gap (i.e., 5 cm upstream), increasing while the reflected shock wave front moves upstream. Eventually, the pressure behind the reflected shock wave front rises to the mean quasi-equilibrium value. The radial secondary oscillations superimposed on the reflected shock wave pressure can be noted at all locations. Their frequencies vary from 9 kHz (5-cm location) to 9.9 kHz (15-cm location), with a value of 9.3 kHz for the 10-cm location, at the centre axis of the shock tube.

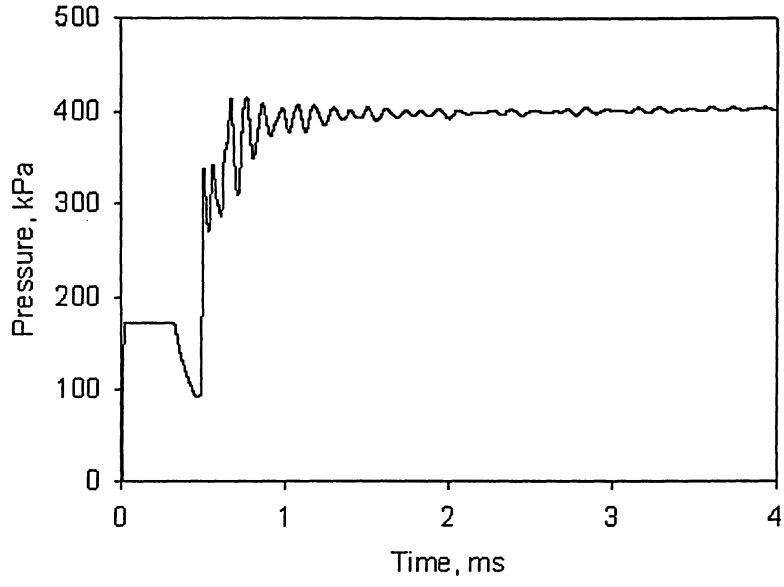

Figure 4.30. Numerical overpressure-time profile at the centre axis, 5 cm upstream (h.e. gap depth = 1 cm, width = 3 cm, p_1 = 375 kPa, p_4 = 850 kPa)

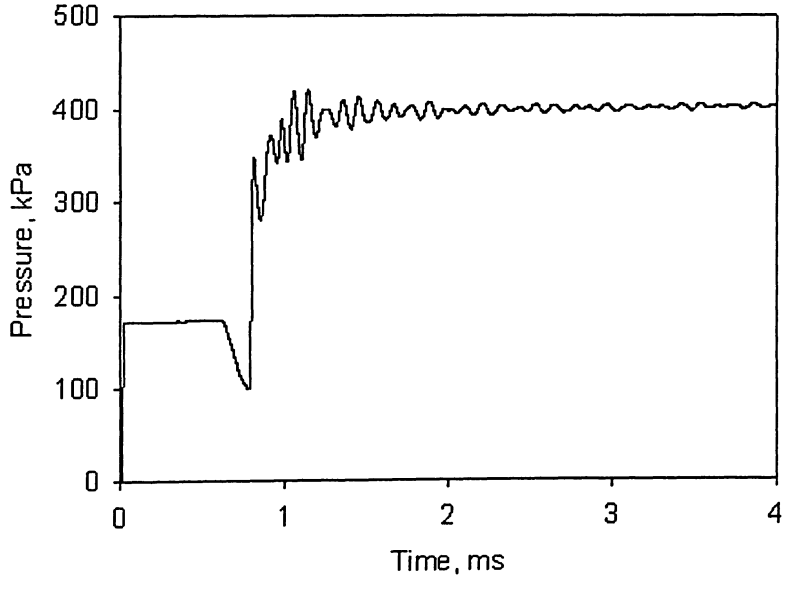

Figure 4.31. Numerical overpressure-time profile at the centre axis, 10 cm upstream (h.e. gap depth = 1 cm, width = 3 cm, p_1 = 375 kPa, p_4 = 850 kPa)

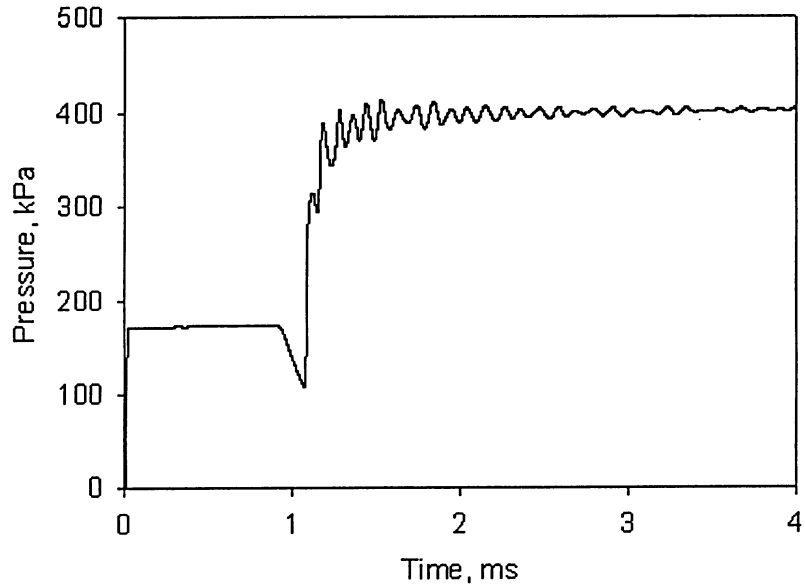

Figure 4.32. Numerical overpressure-time profile at the centre axis, 15 cm upstream (h.e. gap depth = 1 cm, width = 3 cm, p_1 = 375 kPa, p_4 = 850 kPa)

The analysis of the head-end gap width influence on the shock wave interaction with the rocket motor head-end shows that an increase in gap width (while keeping a constant depth and the same incident shock wave strength) will decrease the initial pressure spike of the reflected shock wave and will increase the pressure dip generated by the rarefaction pressure wave compared to the reference case. However, the secondary radial oscillations are present in all cases involving a gap in the head-end region (excepting for the "no gap" case) and their frequency is comparable with the one observed in the reference case. The amplitude of the radial oscillations is decreasing as the head-end gap width is increased relative to the value of the head-end gap depth. One should note that when the gap width is decreased relative to the gap depth, both the initial spike magnitude and the amplitude of the secondary oscillations increase.

4.3.2 Influence of Head-end Gap Depth

The second factor taken into consideration, for the analysis of the influence of gap geometry on the shock wave interaction with the rocket motor head-end, is the gap depth. The depth in this section is changed from 0 cm (no gap case) up to 3 cm, while the head-end gap width is kept constant at 1 cm (as well, the initial driver and driven channel pressures are set as before). Additionally, the incident shock strength is the same in making this comparison.

Although there have been many different cases studied in this investigation, involving various gap depth values, only some of the most relevant results are presented and discussed in this section (i.e., depths of 0.5 cm and 3 cm, respectively). The 0 cm gap depth case is coincident to the 0 cm gap width case discussed in a previous section. The only difference is the time necessary for the incident shock wave to reach the shock tube head-end wall (shorter in the 0 cm width model compared to the 0 cm depth case). As before, the incident shock wave pressure is on the order of 175 kPa and the reflected shock wave is 400 kPa, with no spiking or secondary oscillation development (Fig. 4.17).

The first set of results is presented for the head-end gap case having a depth (0.5 cm) that is less than the one used in the reference case (1 cm). Fig. 4.33 shows the overpressure-time profile corresponding to the 10-cm location, at the wall of the shock tube. The initial pressure spike is on the order of 25 kPa and the secondary radial oscillations have a frequency of 9.2 kHz. One can note the presence of the small pressure dip in the front of the reflected shock wave front, generated by the precursor rarefaction pressure wave moving upstream of the head-end gap region.

The overpressure-time profile at the centre axis, 5 cm upstream of the head end gap, is presented in Fig. 4.34. The initial pressure spike superimposed on the main reflected base pressure is 90 kPa. Overall the pressure profile is similar to the corresponding profile for the reference case. The secondary radial oscillations have a relatively strong amplitude early on, and a frequency of 9 kHz. The observed profile confirms that even for a small gap geometry, the radial activity is strong behind the reflected shock wave front.

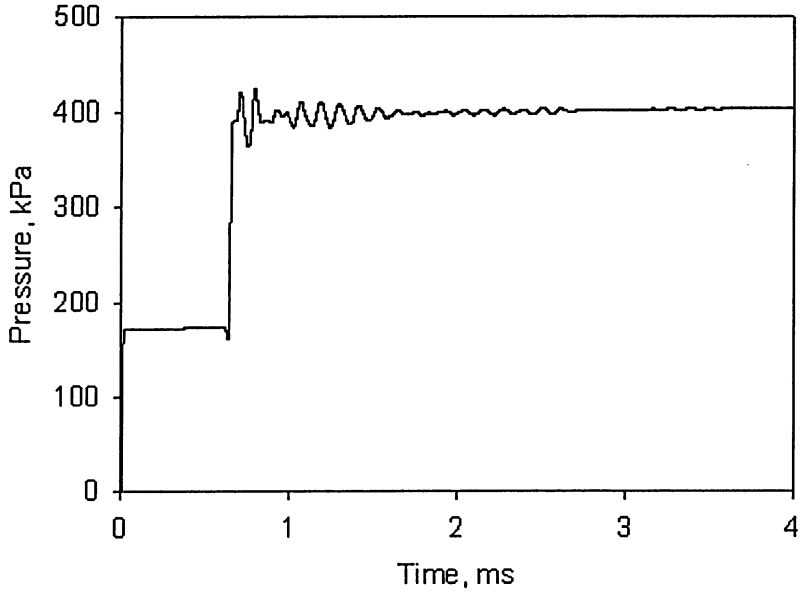

Figure 4.33. Numerical overpressure-time profile at the wall, 10 cm upstream (h.e. gap depth = 0.5 cm, width = 1 cm, p_1 = 375 kPa, p_4 = 850 kPa)

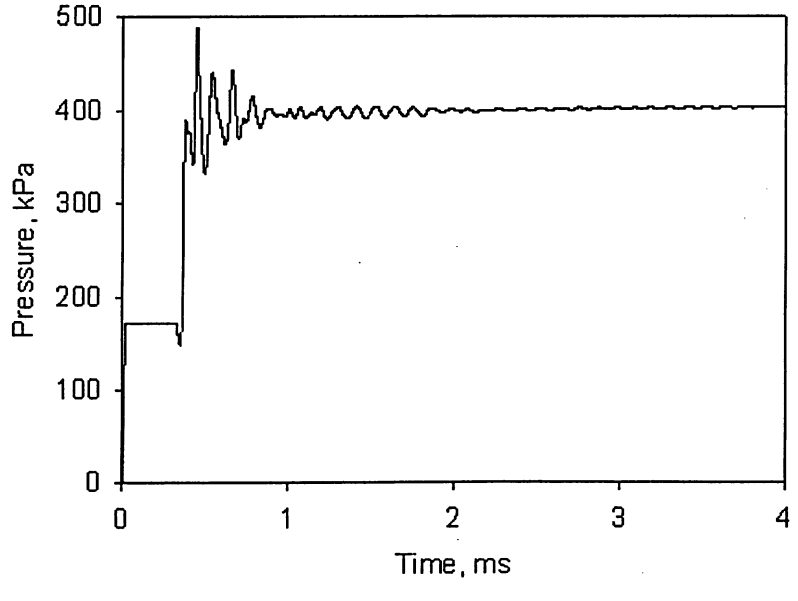

Figure 4.34. Numerical overpressure-time profile at the centre axis, 5 cm upstream (h.e. gap depth = 0.5 cm, width = 1 cm, p_1 = 375 kPa, p_4 = 850 kPa)

Moving further from the head-end region, at the centre axis, overpressure-time profiles are generated for the 10-cm (Fig. 4.35) and 15-cm (Fig. 4.36) locations. The initial pressure spike decreases from 40 kPa to 25 kPa, respectively. The secondary radial oscillations have comparable frequencies, around 8.5 kHz. Analyzing Figs. 4.34 to 4.36, one can note that the small pressure dip in front of the reflected shock wave varies from 20 kPa (close to the head-end gap at the 5-cm position) to 0 kPa at the 15-cm location. The small gap geometry doesn't generate as strong a rarefaction wave as the ones seen for a bigger gap depth at the same width.

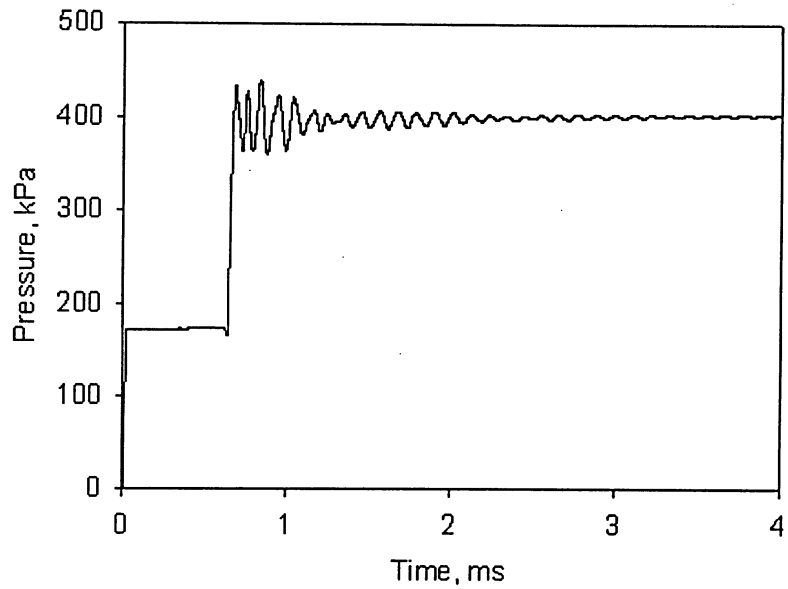

Figure 4.35. Numerical overpressure-time profile at the centre axis, 10 cm upstream (h.e. gap depth = 0.5 cm, width = 1 cm, p_1 = 375 kPa, p_4 = 850 kPa)

In Fig. 4.37, the predicted pressure-time profile is shown for the 10-cm upstream position at the wall of the shock tube, for a head-end gap geometry of 3-cm depth and 1-cm width. The incident shock wave pressure is 175 kPa as before, but in front of the main reflected shock wave arrival one can observe a small precursor reflected shock generated by the normal wave reflection from the head-end wall, a phenomenon that occurs before the main reflected wave is generated and exits from the deep gap cavity. The base

pressure behind the reflected shock wave is on the order of 400 kPa, similar to the reference case. The initial pressure spike is 25 kPa, less than the reference case value.

Fig. 4.38 shows the overpressure profile at the centre axis of the shock tube for the 5-cm upstream location. The initial pressure spike is 100 kPa and one can note a considerable increase in the early secondary oscillations. The precursor reflected shock has a pressure spike of 80 kPa (measured from the incident shock wave pressure value of 175 kPa). The secondary oscillations have a frequency of 8.7 kHz.

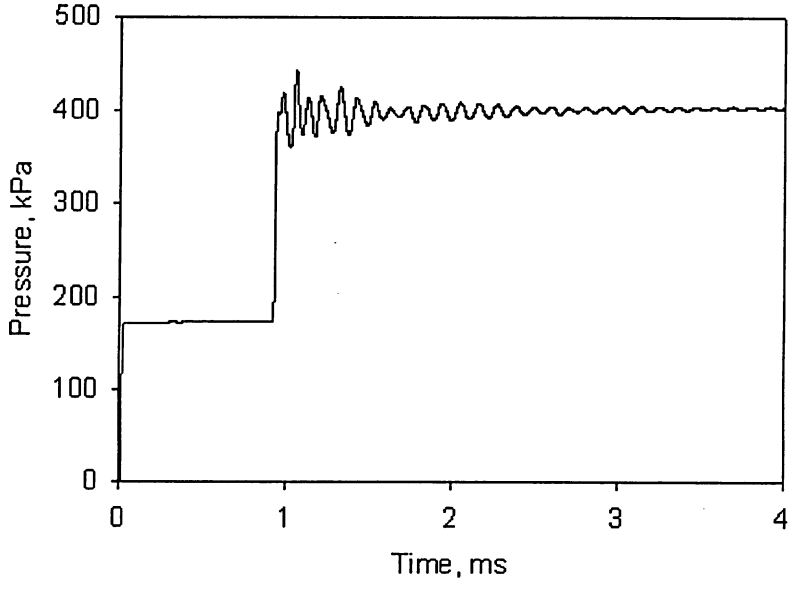

Figure 4.36. Numerical overpressure-time profile at the centre axis, 15 cm upstream (h.e. gap depth = 0.5 cm, width = 1 cm, p_1 = 375 kPa, p_4 = 850 kPa)

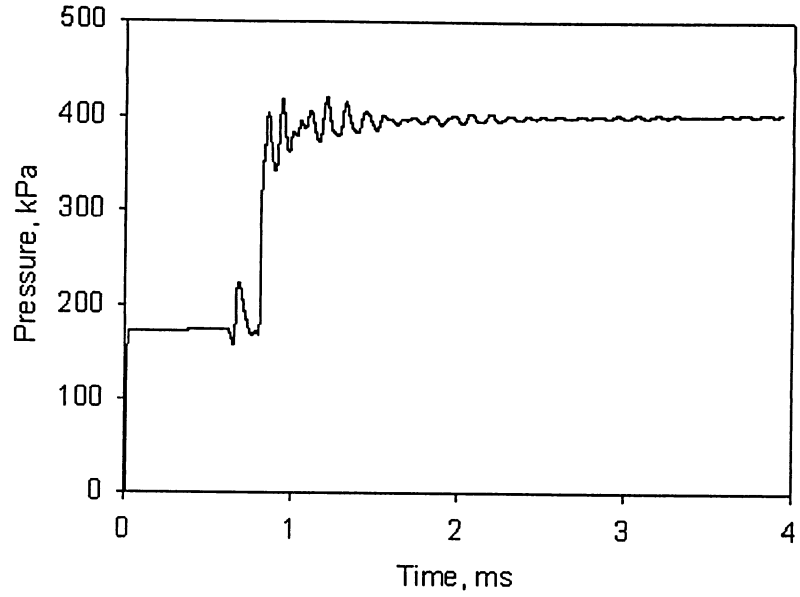

Figure 4.37. Numerical overpressure-time profile at the wall, 10 cm upstream (h.e. gap depth = 3 cm, width = 1 cm, p_1 = 375 kPa, p_4 = 850 kPa)

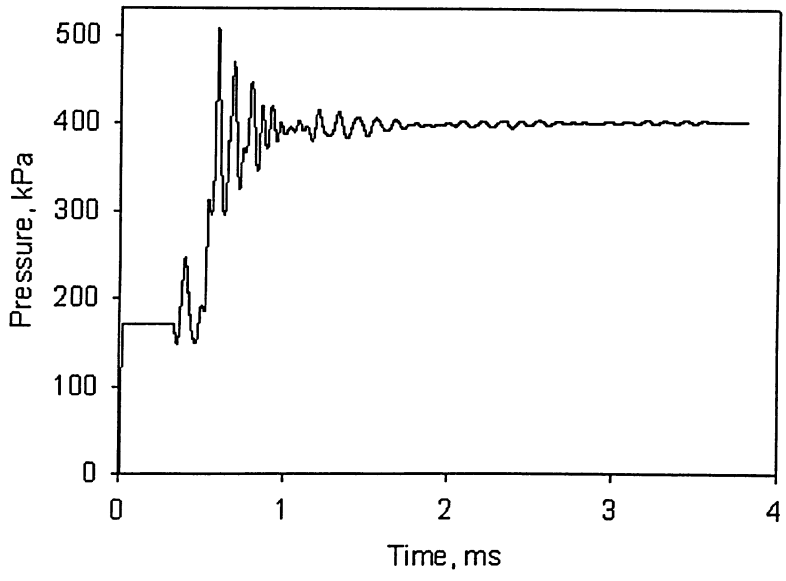

Figure 4.38. Numerical overpressure-time profile at the centre axis, 5 cm upstream (h.e. gap depth = 3 cm, width = 1 cm, p_1 = 375 kPa, p_4 = 850 kPa)

Figs. 4.39 and 4.40 depict the pressure profiles along the centre axis of the shock tube at 10-cm and 15-cm location, respectively. The precursor reflected pressure value decreases from 40 kPa to only 25 kPa at the 15-cm position. However, one can note the increase in the early secondary oscillations' magnitude, the amplitude remaining almost the same as the initial pressure spike for about 0.5 ms, before starting to decay. From these results one can conclude that the head-end gap depth has a relatively stronger influence on the secondary radial oscillations' development, as compared to the gap width.

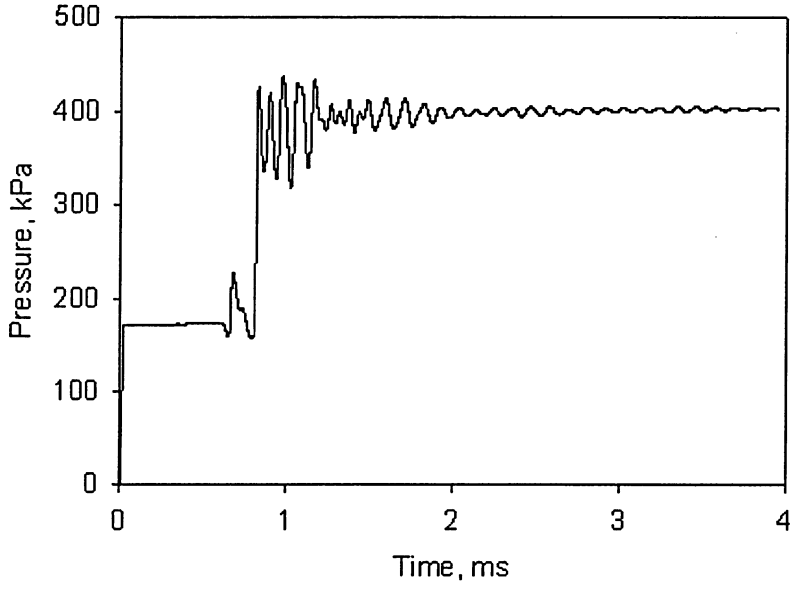

Figure 4.39. Numerical overpressure-time profile at the centre axis, 10 cm upstream (h.e. gap depth = 3 cm, width = 1 cm, p_1 = 375 kPa, p_4 = 850 kPa)

To conclude, it seems that the head-end gap depth has a stronger direct influence on the radial oscillation behaviour, while the head-end gap width has a more important influence on the axial shock wave behaviour. The interaction between the axial and radial shock waves can be studied further, by changing both the depth and the width of the head-end gap, as discussed in the next section.

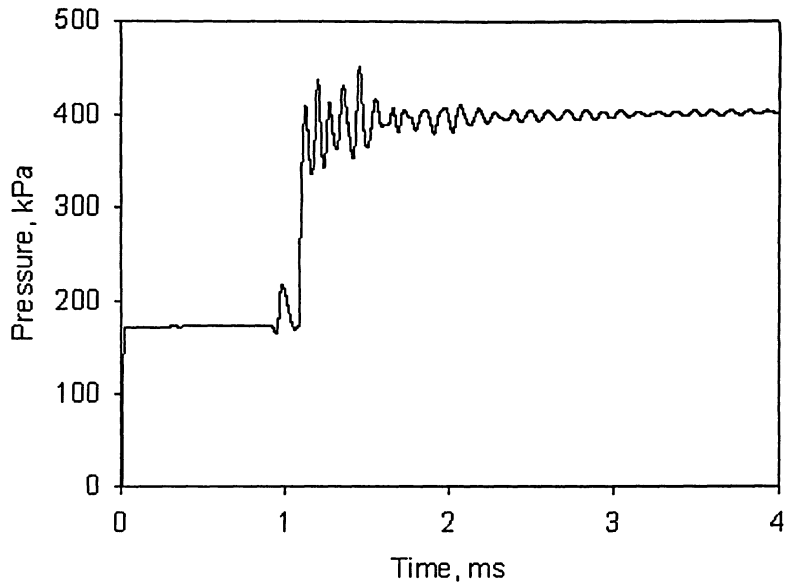

Figure 4.40. Numerical overpressure-time profile at the centre axis, 15 cm upstream (h.e. gap depth = 3 cm, width = 1 cm, p_1 = 375 kPa, p_4 = 850 kPa)

4.3.3 Combined Change of the Gap Depth and Width

The combined effect of varying both the head-end gap depth and width, for the same incident shock wave strength (i.e., the initial driven and driver pressures are kept constant in all cases, 375 kPa and 850 kPa, respectively), has been analyzed as well in this investigation. The gap geometry was changed in a matrix format (i.e., starting from 0.5 cm depth by 0.5 cm width, up to 3 cm depth by 3 cm width); only some key results are presented in the current thesis: 0.5-cm by 0.5-cm, 3-cm by 2-cm, and 3-cm by 3-cm gap geometry (the gap geometry is defined as depth value by width value).

Fig. 4.41 shows the overpressure-time profile at the 10-cm location, at the wall of the shock tube, for a gap geometry of 0.5 cm depth by 0.5 cm width. The incident shock wave overpressure remains the same as in the reference case (175 kPa) as well as the main reflected shock wave pressure (400 kPa). The initial pressure spike is around 25 kPa, less than the 40 kPa value for the reference case, at the same location. The secondary

oscillations superimposed on the main reflected shock wave have a frequency of 9 kHz, comparable to that observed for the 1-cm gap.

The pressure-time profile at the centre axis, close to the head-end gap region (5-cm upstream) shows strong radial secondary oscillation development behind the reflected shock wave front (Fig. 4.42). The initial spike is 60 kPa with the follow-on secondary pressure spike increasing to 110 kPa, and only after that do the oscillations proceed to subside. The secondary oscillations have a high amplitude for almost 1 ms, and the frequency is on the order of 9.3 kHz.

Moving upstream from the head-end, the pressure-time results are presented for the 10-cm (Fig. 4.43) and 15-cm (Fig. 4.44) location, at the centre axis of the shock tube. One can note the strong radial pressure wave development with maximum amplitudes of 60 kPa at both locations. One can note that there is no phenomenon recorded in front of the main reflected shock wave (neither the pressure dip or rise of a reflected precursor wave) as seen in previous results involving a bigger gap cavity. In general, these results suggest the presence of a very small gap (relative to the overall diameter of the core flow) in the head-end area of a rocket motor will trigger the development of secondary radial oscillations that may have an initial pressure spike up to 30% of the main reflected quasi-equilibrium shock wave base pressure.

The results obtained for a gap geometry of 3-cm depth and 2-cm width are presented in Figs. 4.45 to 4.47. One can note a substantial combined axial and radial wave development behind the first reflected shock front.

The interaction between the radial and axial waves is obvious even in front of the main reflected shock wave front. The big pressure dip resulting from a strong precursor reflected rarefaction wave, that can have values up to 100 kPa, undergoes an interaction with a follow-on precursor reflected shock wave. The pressure dip is an effect of the gap depth, generating the rarefaction pressure wave, while the precursor reflected shock wave is influenced more directly by the gap width. Depending on the available expansion volume for the incident shock wave, the pressure dip generated by the rarefaction wave can be quite substantial.

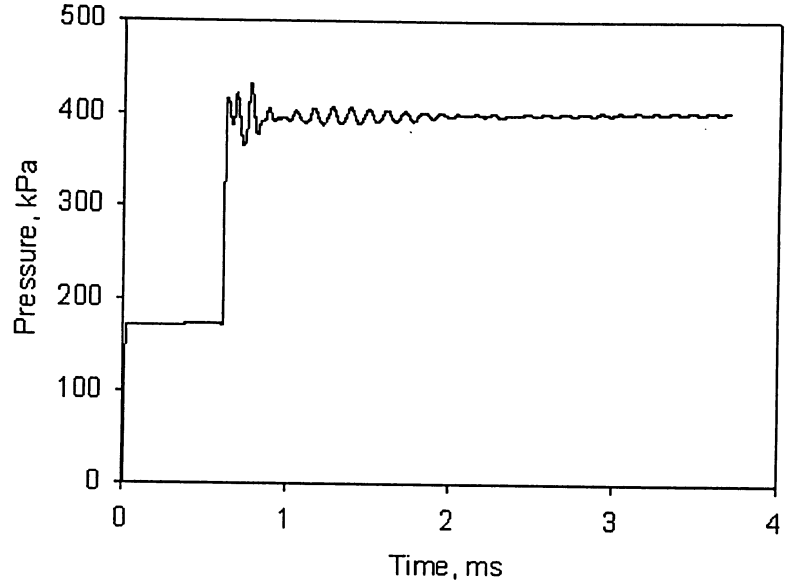

Figure 4.41. Numerical overpressure-time profile at the wall, 10 cm upstream (h.e. gap depth = 0.5 cm, width = 0.5 cm, p_1 = 375 kPa, p_4 = 850 kPa)

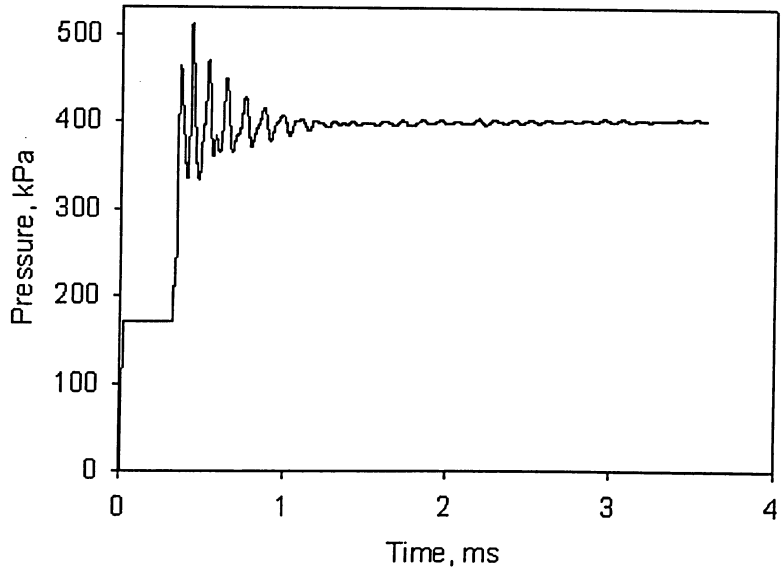

Figure 4.42. Numerical overpressure-time profile at the centre axis, 5 cm upstream (h.e. gap depth = 0.5 cm, width = 0.5 cm, p_1 = 375 kPa, p_4 = 850 kPa)

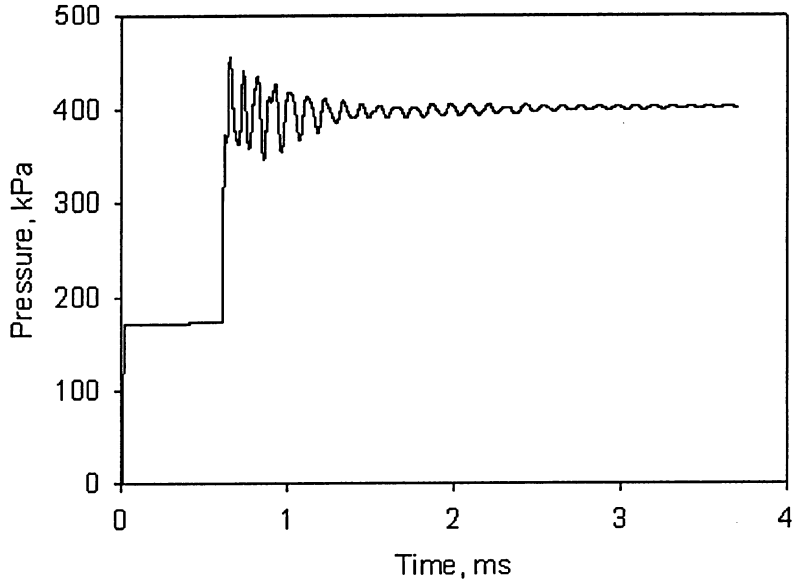

Figure 4.43. Numerical overpressure-time profile at the centre axis, 10 cm upstream (h.e. gap depth = 0.5 cm, width = 0.5 cm, p_1 = 375 kPa, p_4 = 850 kPa)

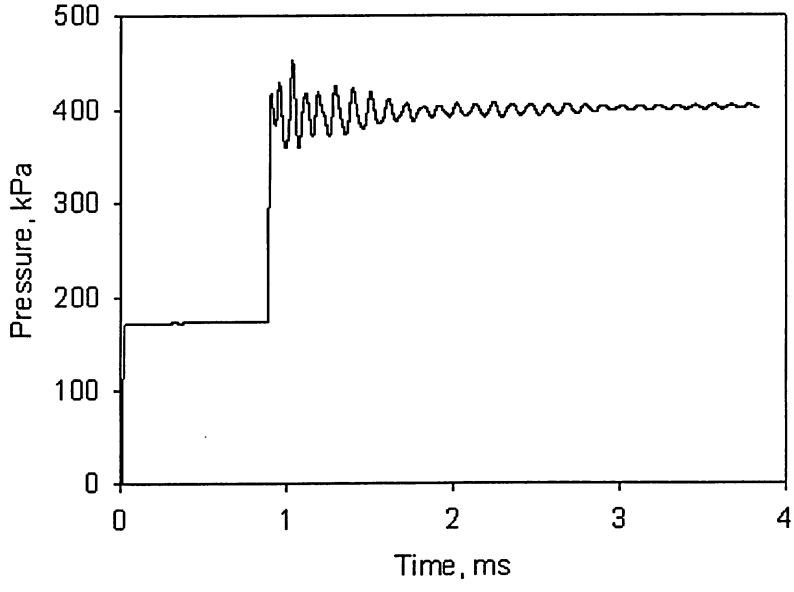

Figure 4.44. Numerical overpressure-time profile at the centre axis, 15 cm upstream (h.e. gap depth = 0.5 cm, width = 0.5 cm, p_1 = 375 kPa, p_4 = 850 kPa)

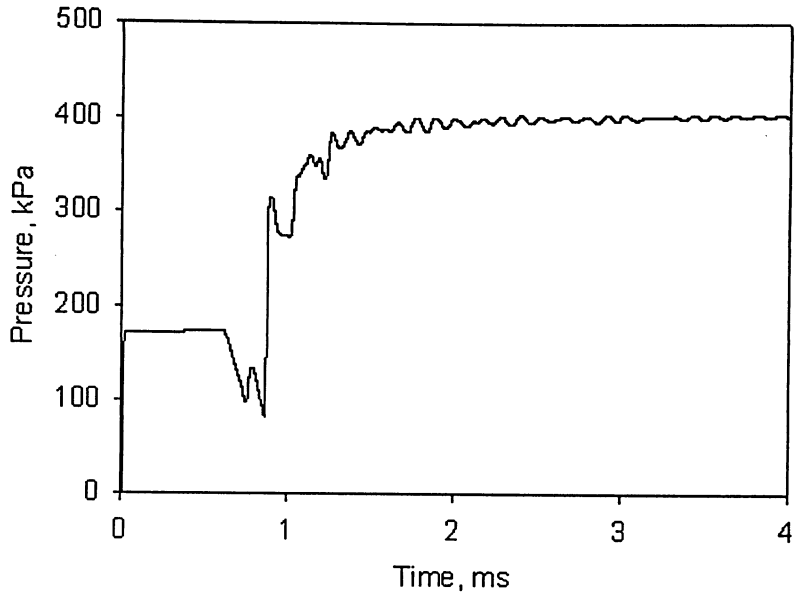

Figure 4.45. Numerical overpressure-time profile at the wall, 10 cm upstream (h.e. gap depth = 3 cm, width = 2 cm, p_1 = 375 kPa, p_4 = 850 kPa)

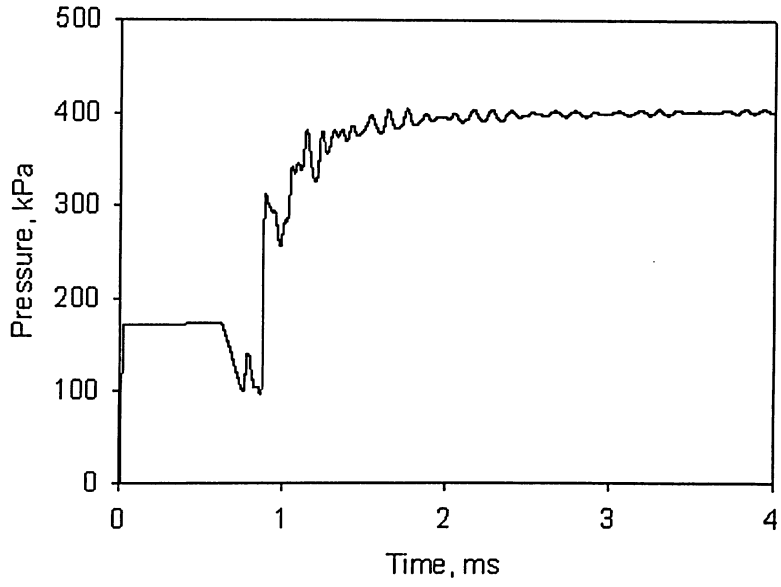

Figure 4.46. Numerical overpressure-time profile at the centre axis, 10 cm upstream (h.e. gap depth = 3 cm, width = 2 cm, p_1 = 375 kPa, p_4 = 850 kPa)

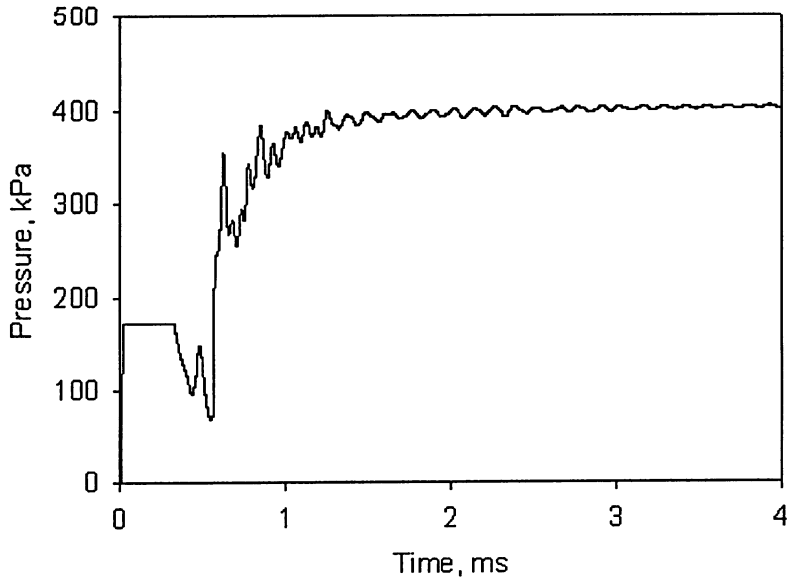

Figure 4.47. Numerical overpressure-time profile at the centre axis, 5 cm upstream (h.e. gap depth = 3 cm, width = 2 cm, p_1 = 375 kPa, p_4 = 850 kPa)

The overpressure-time results for the gap geometry of 3-cm depth by 3-cm width, 10-cm upstream, at the wall and the centre axis of the shock tube, are provided in Figs. 4.48 and 4.49. One can note a stronger axial-radial wave interaction than in the previous case (3-cm by 2-cm). After a period of time of approximately 1 ms, the mean pressure rises to the quasi-equilibrium value of 400 kPa. The radial oscillations after that moment of time have a very small amplitude, and the frequency is on the order of 8.4 kHz. The pressure dip ahead of the reflected shock wave front is present for a longer period of time in this case (compared to the previous one), this phenomenon being influenced by the increased gap width (i.e., there is no precursor low-amplitude reflected shock wave in the front of the main reflected shock wave).

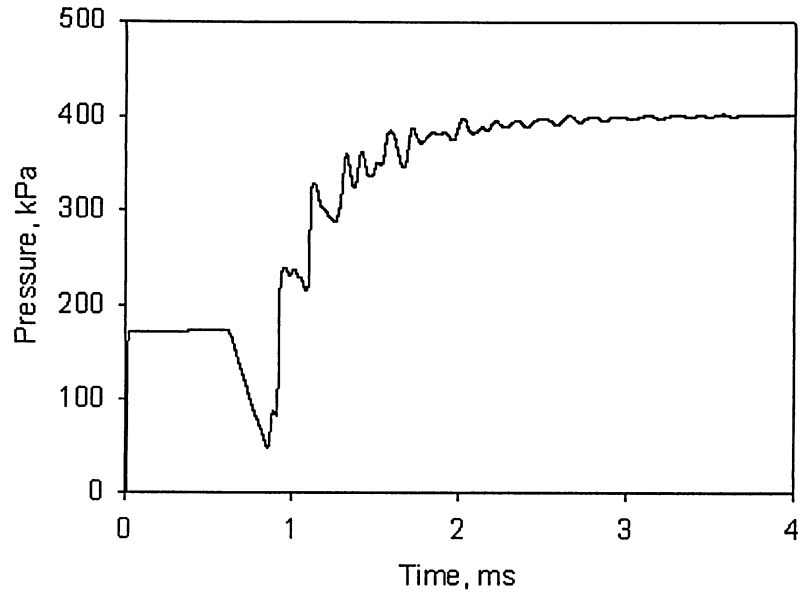

Figure 4.48. Numerical overpressure-time profile at the wall, 10 cm upstream (h.e. gap depth = 3 cm, width = 3 cm, p_1 = 375 kPa, p_4 = 850 kPa)

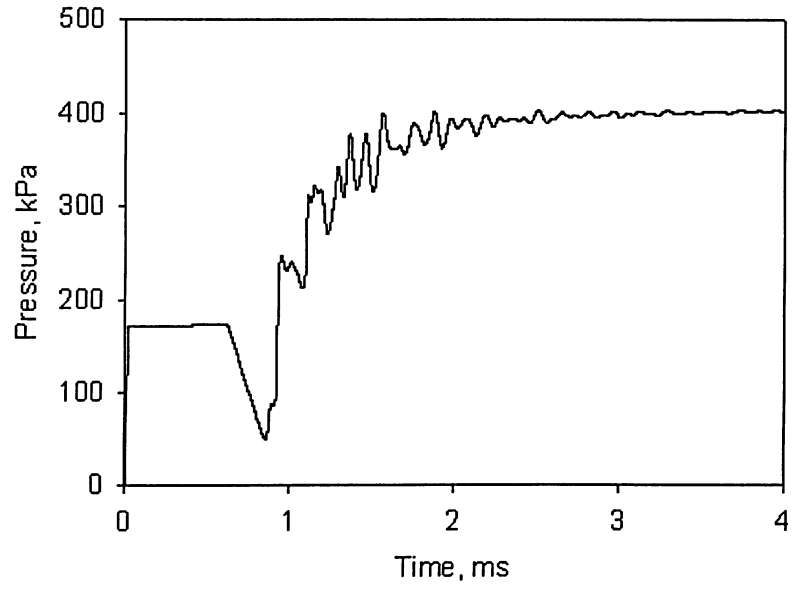

Figure 4.49. Numerical overpressure-time profile at the centre axis, 10 cm upstream (h.e. gap depth = 3 cm, width = 3 cm, p_1 = 375 kPa, p_4 = 850 kPa)

Generally speaking, these results suggest that beyond a certain width (and/or depth to some degree in conjunction) for the head-end gap, the severity of the reflected shock front's initial/principal spike is lessened (observed to be falling below the quasi-equilibrium base reflected shock pressure level, in the absolute reference frame). Additionally, the follow-on secondary axial/radial oscillations (observed to be of some magnitude, but less ordered with mixed axial and radial wave frequencies) are somewhat lessened in severity by the larger gap volume.

4.4 Increased Incident Shock Wave Strength

Another potentially important factor for consideration, in studying the interaction of a traveling shock wave with the rocket motor head-end, is the effect of incident shock wave strength on subsequent wave behaviour. This analysis was done for the reference gap geometry (i.e., 1 cm gap width by 1 cm gap depth), keeping the driven channel pressure constant at 375 kPa (same as in the reference case) and increasing the driver chamber pressure. The incident shock wave strength (that is a function of driver and driven channel pressure) is increased by increasing the initial pressure of the driver channel (the high-pressure section of the shock tube). Both experimental and numerical investigations were carried out.

The experimental study of the high-pressure cases for the wave interaction with the head-end region is limited by the shock tube installation's capabilities and its safety features/limits. In order to attain higher pressures for the incident shock, the pressure difference between the two chambers of the shock tube, before the diaphragm rupture, was increased by using two polyester film diaphragms, each having a thickness of 0.08 mm. For a standard driven channel pressure of 375 kPa, the maximum allowed driver channel pressure, provided by the two-stage compressor, was not able to passively (i.e., without mechanical means) burst the double diaphragm in order to generate the desired incident shock wave. Therefore, for the experimental firings, the driven channel pressure was lowered to 250 kPa. Having this set-up in place, the double-diaphragm was ruptured when the driver pressure reached the permissible 1000 kPa value.

The experimental overpressure-time profile, at the pressure transducer location (i.e., 10-cm upstream of the head-end, at the wall of the shock tube), is shown in Fig. 4.50. The incident shock wave's pressure is on the order of 240 kPa (overpressure) and the main reflected shock wave quasi-equilibrium base pressure is around 680 kPa. The increase in the incident shock wave generates an increase of the initial pressure spike superimposed on the main reflected shock wave from 40 kPa for the reference case to 75 kPa here, with more intense secondary oscillation activity.

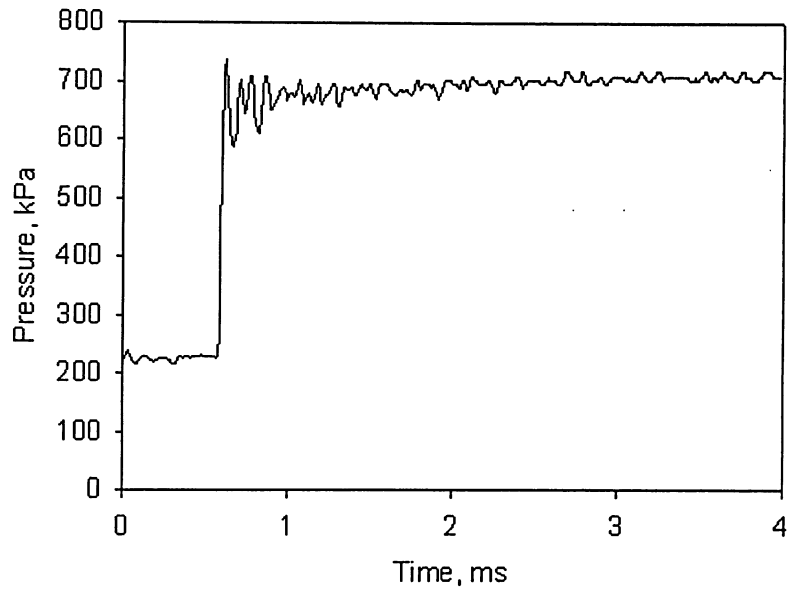

Figure 4.50. Experimental overpressure-time profile at the wall, 10 cm upstream (h.e. gap depth = 1 cm, width = 1 cm, p_1 = 250 kPa, p_4 = 1000 kPa)

A better understanding of the incident shock wave influence can be obtained by analyzing the numerical results. With no maximum-pressure constraints in place (unlike those noted for the experimental firings), the initial driver channel pressure was increased in the numerical cases to the following values: 1150 kPa, 1350 kPa, 2000 kPa, and 2500 kPa (the driven channel pressure being constant, at the reference value of 375 kPa for a more direct comparison to earlier reference results, as opposed to the experimental value of 250 kPa used for the high-pressure cases).

In Figs. 4.51 and 4.52 the pressure-time profiles for the driver channel pressure of 1150 kPa are presented. The incident shock wave overpressure is 275 kPa and the main reflected shock wave base is 680 kPa. At the 5-cm upstream location, at the centre axis, the initial pressure spike is 240 kPa, representing almost 35% of the reflected shock wave base pressure, while at the 10-cm location the pressure spike is 120 kPa, or 17% of the base pressure. The frequency of the secondary oscillations is 8.4 and 8.9 kHz, respectively.

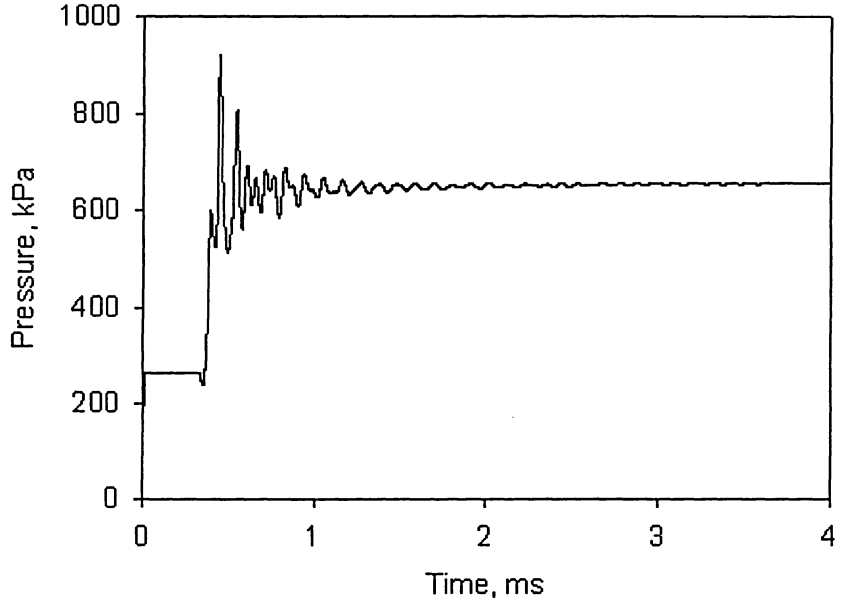

Figure 4.51. Numerical overpressure-time profile at the centre axis, 5 cm upstream (h.e. gap depth = 1 cm, width = 1 cm, p_1 = 375 kPa, p_4 = 1150 kPa)

The results for a driver pressure of 1350 kPa, both at the 5-cm and 10-cm locations upstream of the head-end gap, at the centre axis of the shock tube, are provided in Figs. 4.53 and 4.54. The incident shock wave overpressure is around 300 kPa and the main reflected shock wave base pressure is on the order of 800 kPa. The initial pressure spike varies from 380 kPa (47% of the reflected shock wave pressure) at the 5-cm location to 185 kPa (23 %) at the 10-cm location.

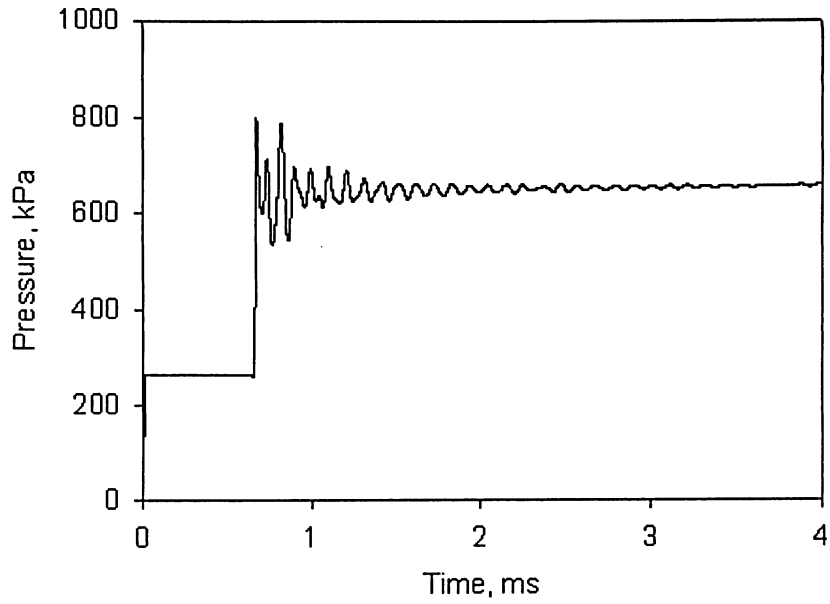

Figure 4.52. Numerical overpressure-time profile at the centre axis, 10 cm upstream (h.e. gap depth = 1 cm, width = 1 cm, p_1 = 375 kPa, p_4 = 1150 kPa)

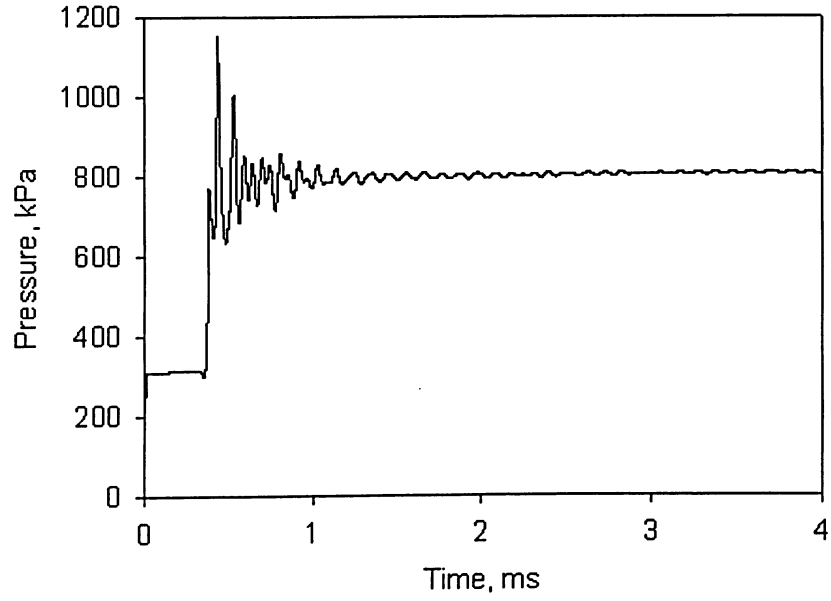

Figure 4.53. Numerical overpressure-time profile at the centre axis, 5 cm upstream (h.e. gap depth = 1 cm, width = 1 cm, p_1 = 375 kPa, p_4 = 1350 kPa)

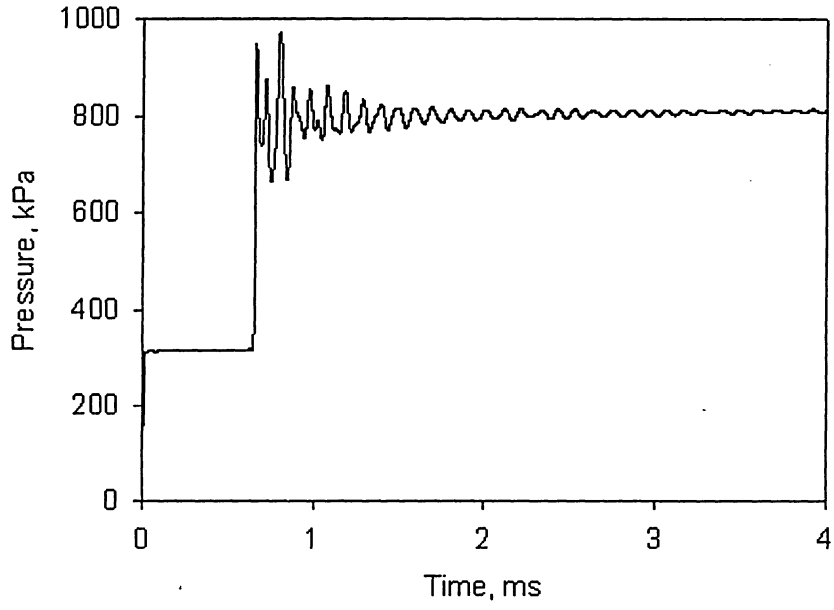

Figure 4.54. Numerical overpressure-time profile at the centre axis, 10 cm upstream (h.e. gap depth = 1 cm, width = 1 cm, p_1 = 375 kPa, p_4 = 1350 kPa)

Figs. 4.55 and 4.56 depict the overpressure-time profiles, at the centre axis of the shock tube, 5 cm and 10 cm upstream of the head-end gap, for a driver pressure of 2000 kPa. The incident shock wave's overpressure is 450 kPa and the quasi-equilibrium reflected shock wave's pressure is 1250 kPa. One can note that the initial pressure spike doesn't have the peak magnitude, the maximum here being reached in a subsequent radial oscillation cycle. The maximum pressure value increases from 250 kPa (20 % of the reflected shock base pressure) at the 10-cm location to 550 kPa (44%) at the 5-cm position. One can note that the percentage corresponding to the maximum pressure value remains comparable to the previous case (driver pressure of 1350 kPa). A further increase of the driver pressure will help in identifying a general trend regarding the relationship between the initial pressure spike and the incident shock wave pressure.

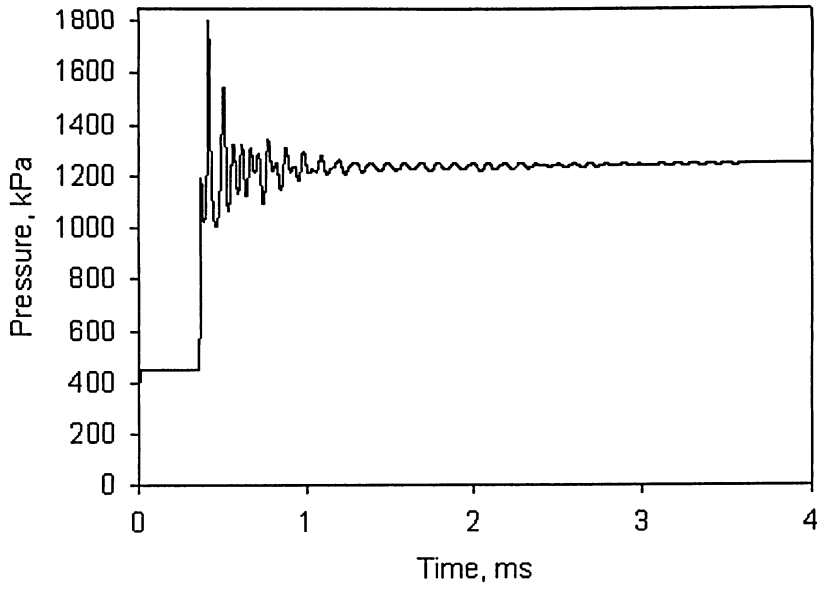

Figure 4.55. Numerical overpressure-time profile at the centre axis, 5 cm upstream (h.e. gap depth = 1 cm, width = 1 cm, p_1 = 375 kPa, p_4 = 2000 kPa)

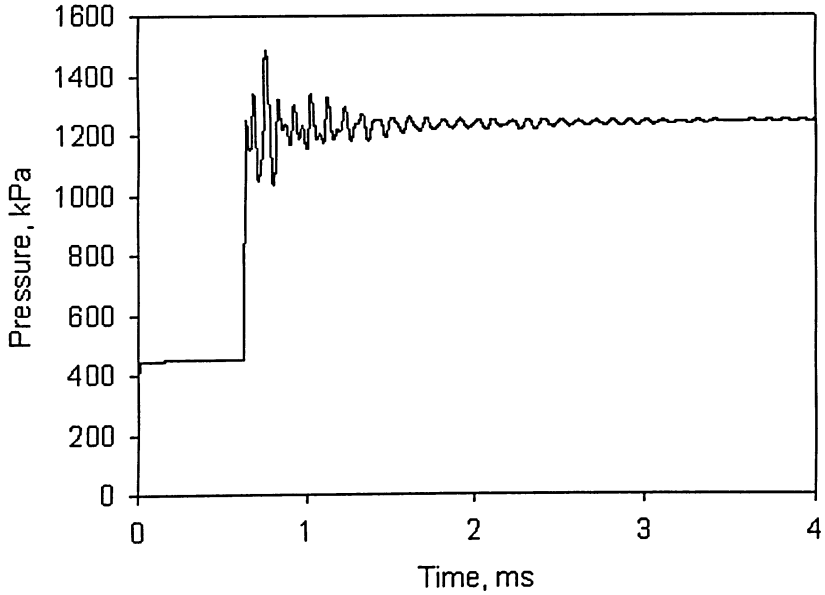

Figure 4.56. Numerical overpressure-time profile at the centre axis, 10 cm upstream (h.e. gap depth = 1 cm, width = 1 cm, p_1 = 375 kPa, p_4 = 2000 kPa)

The driver pressure was further increased to a value of 3000 kPa. The pressure time results are shown in Figs. 4.57 and 4.58 for the same location as in the previous case (i.e., 5-cm and 10-cm upstream positions at the centre axis of the shock tube, respectively). The incident shock wave overpressure observed is on the order of 520 kPa and the main reflected quasi-equilibrium base pressure is around 1550 kPa. The initial pressure spike at the 5-cm location is 650 kPa, corresponding to 42% of the main reflected base pressure. For the 10-cm location, the maximum pressure (recorded behind the initial pressure spike) is 250 kPa (corresponding to only 16%).

Overall, the latter augmentation effects for observed peak spike strength would indicate a direct proportionality relative to the incident shock strength.

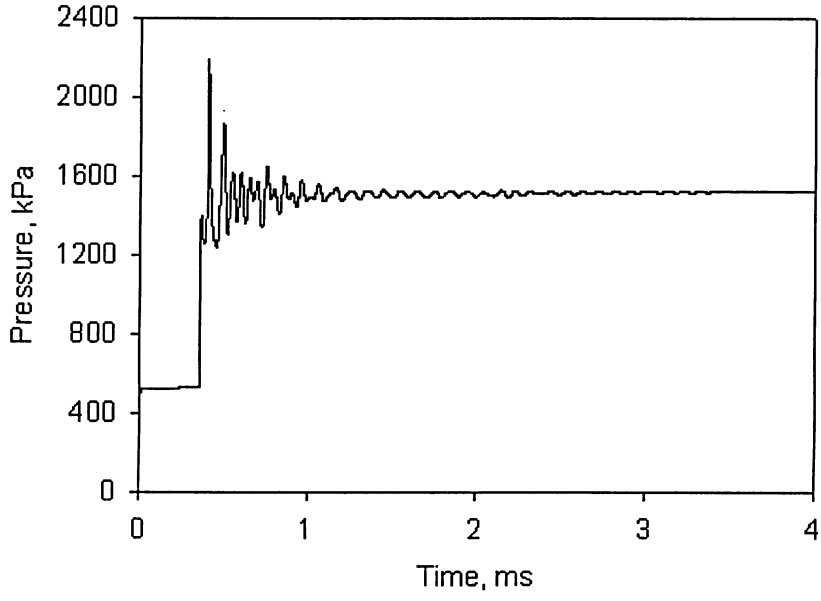

Figure 4.57. Numerical overpressure-time profile at the centre axis, 5 cm upstream (h.e. gap depth = 1 cm, width = 1 cm, p_1 = 375 kPa, p_4 = 3000 kPa)

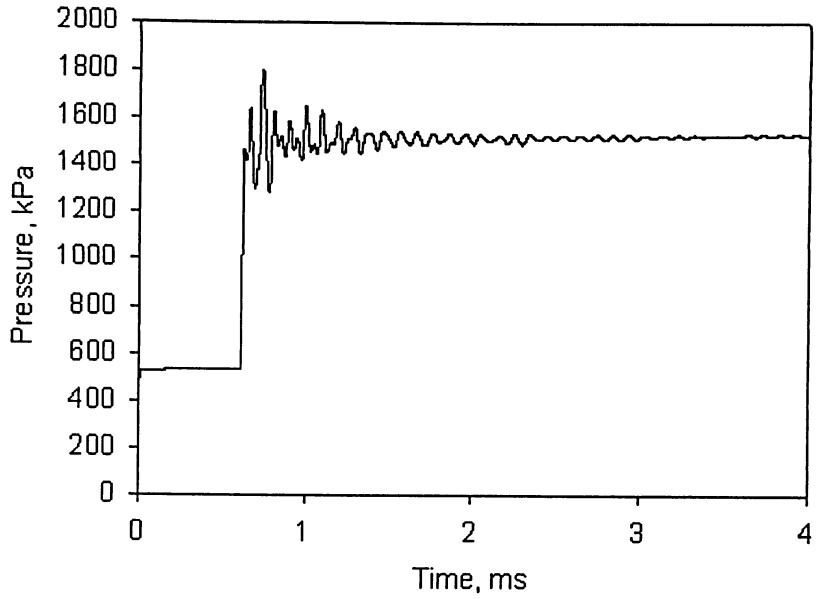

Figure 4.58. Numerical overpressure-time profile at the centre axis, 10 cm upstream (h.e. gap depth = 1 cm, width = 1 cm, p_1 = 375 kPa, p_4 = 3000 kPa)

Chapter 5. Summary and Conclusions

The current investigation deals with one of the primary symptoms of non-linear axial combustion instability in solid rocket motors, more precisely with a limited-amplitude axial compression wave moving back and forth along the combustion chamber of an SRM. On the basis of previous experimental observation of pressure-time profiles in the combustion chamber and propellant base burning rates, a potential driving mechanism for this symptom, which is gasdynamic in nature, involving reinforcement of a reflected shock wave in the rocket motor head-end region, was suggested. The particular mechanism in question was the main focus of the current thesis. Specifically, experiments and numerical simulations were employed to examine the various aspects surrounding the interaction of an incident traveling normal shock wave with the head-end of an SRM.

For the experimental component of this study, a customized shock tube apparatus, with air at room temperature as the working fluid, was used. A two-dimensional axisymmetric model of the shock tube was developed for computational fluid dynamics simulations. Various experimental and numerical overpressure-time profiles are presented in Chapter 4. Parameters of interest in this investigation included magnitude of the initial pressure spike superimposed on the main reflected wave's quasi-equilibrium base pressure, the mean radial wave frequency, and the strength and duration of the radial waves generated in each case.

For the reference head-end gap case (i.e., gap geometry of 1 cm depth and 1 cm width, driver and driven channel pressures of 850 kPa and 375 kPa, respectively), at each axial position, the secondary oscillations (associated with radial and secondary axial wave development) are generally of higher amplitude at the centre axis than at the wall of the shock tube, and they are present for a longer period of time. The mean radial wave frequency for the secondary oscillations was observed to decrease in general when one moves from the wall to the centre axis. Also, the oscillations' mean radial wave frequency along the centre axis of the shock tube appeared to decrease as the axial position increased from the 5-cm position to the 15-cm position upstream of the shock tube head-end gap region. Generally, as one might expect, the radial waves strengthen as

one moves radially from the wall to the centre axis of the shock tube and, axially, as one moves closer to the head-end gap location.

The inviscid-flow overpressure-time profiles obtained for the reference case imply that the interaction between the traveling shock wave and the head-end of the shock tube have a very similar behaviour with that noted in the viscous reference case. The mean radial wave frequency remains the same at all monitored locations, and the overpressure-time profiles show a similar pressure distribution (although the inviscid profile is shifted in the positive direction of the pressure axis, given the lack of boundary-layer induced viscous losses).

An objective of the current thesis was to determine the influence of the gap geometry on the initial pressure spike and on the secondary radial oscillations superimposed on the quasi-equilibrium reflected shock wave base pressure. Various experimental and numerical simulations were done to evaluate the head-end gap width influence, head-end gap depth influence, and the combined effect of varying both the depth and the width of the head-end gap region.

The analysis of the head-end gap width influence on the shock wave interaction with the rocket motor head-end shows that an increase in gap width (while keeping a constant depth and the same incident shock wave strength) will decrease the initial pressure spike of the reflected shock wave and will increase the pressure dip generated by the rarefaction pressure wave compared to the reference case. However, the secondary radial oscillations are present in all cases involving a gap in the head-end region (excepting the "no gap" case) and their frequency is comparable with the one observed in the reference case. The amplitude of the radial oscillations is decreasing as the head-end gap width is increased relative to the value of the head-end gap depth. One should note that when the gap width is decreased relative to the gap depth, both the initial spike magnitude and the amplitude of the secondary oscillations increase. In general, the head-end gap depth has a stronger direct influence on the radial oscillation behaviour, while the head-end gap width has a more important influence on the axial shock wave behaviour.

For the combined variation of the width and the depth of the head-end gap, the obtained results suggest that beyond a certain width (and/or depth to some degree in conjunction) for the head-end gap, the severity of the reflected shock front's

initial/principal spike is lessened (observed to be falling below the quasi-equilibrium base reflected shock pressure level, in the absolute reference frame). Additionally, the follow-on secondary axial/radial oscillations (observed to be of some magnitude, but less ordered with mixed axial and radial wave frequencies) are somewhat lessened in severity by the larger gap volume.

Another important factor examined in the present study was the effect of the incident normal shock wave strength on subsequent wave behaviour. The analysis of this factor involved the assumptions that the head-end gap geometry remains the same as in the reference case (i.e., the head-end gap width is 1 cm and the head-end gap depth is 1 cm); as well, the driver channel pressure is kept constant at 375 kPa in all numerical simulations. The increase in the shock wave strength results in an increase in the reflected shock wave's pressure, and subsequently of the initial pressure spike, with more intense secondary oscillation activity. The latter augmentation effects would indicate some direct proportionality relative to the incident shock strength.

The various experimental and numerical overpressure-time profiles, at different driven channel pressures and at different axial and radial locations, confirm the appearance of substantial radial wave activity following the initial reflection of the incident shock wave from the shock tube head-end gap. In an analogous case of an SRM encountering non-linear axial combustion instability, the transient radial wave action superimposed on the main reflected wave front of a traveling axial compression wave could potentially instigate an augmentation of the local propellant burning rate in the head-end region, which in turn might act to reinforce the axial wave, possibly leading to sustained non-steady combustion behaviour inside the combustion chamber of an SRM. Also, other potential combustion-related driving mechanisms might be supported or enhanced by the radial wave activity observed in the present study.

As a final recommendation coming out of the present investigation, it is to be noted that a shock tube apparatus able to operate at higher channel pressures would be of use in future studies. Bringing the cold-flow experiment closer to actual rocket motor conditions, i.e., higher operating pressures, may better highlight the influence of the gasdynamic factors observed in this study, or possibly demonstrate the existence of new effects not observed at lower pressures (e.g., boundary layer separation). In this regard,

higher pressure air, or various combinations of monatomic or diatomic gases, could be used in the driver and driven channels of the shock tube. Such an experimental study would entail utilizing a pressure transducer having a higher operating range, and would depend on the structural limits of the experimental apparatus (the present structure may require substantial strengthening).

REFERENCES

1. Kuo, K.K., and Summerfield, M. (ed.), *"Fundamentals of Solid-Propellant Combustion,"* Progress in Astronautics and Aeronautics, Vol. 90, AIAA Publications, 1984.

2. Karnesky, A.L., and Colucci, S.E., *"Recent Occurrences of Combustion Instability in Solid Rocket Motors,"* Journal of Spacecraft and Rockets, Vol. 12, No. 1, January 1975, pp. 33-38.

3. Sutton, G.P., and Biblarz, O., *Rocket Propulsion Elements*, 7th ed., John Wiley & Sons, Inc., New York, 2001.

4. .Culick, F.E.C., *"Combustion Instabilities: Mating Dance of Chemical, Combustion, and Combustor Dynamics,"* 36th AIAA/ASME/SAE/ASEE Joint Propulsion Conference, AIAA Paper No. 2000-3178, Huntsville, July 16-19, 2000.

5. Greatrix, D.R., *"Structural Vibration and Solid Rocket Combustion Instability,"* Canadian Aeronautics and Space Journal, Vol. 44, No. 1, March 1998, pp. 9-24.

6. Greatrix, D.R., *"Combined Structural Oscillation Effects on Solid Rocket Internal Ballistics,"* 35th AIAA/ASME/SAE/ASEE Joint Propulsion Conference, AIAA Paper No. 99-2509, Los Angeles, June 20-24, 1999.

7. Greatrix, D.R., and Harris, P.G., *"Structural Vibration Considerations for Solid Rocket Internal Ballistics Modelling,"* 36th AIAA/ASME/SAE/ASEE Joint Propulsion Conference, AIAA Paper No. 2000-3804, Huntsville, July 17-19, 2000.

8. Harris, P.G., Wong, F.C., and de Champlain, A., *"The Influence of Structural Vibrations on Pulse-Triggered Nonlinear Instability in Solid Rocket Motors: An Experimental Study,"* 32nd AIAA/ASME/SAE/ASEE Joint Propulsion Conference, AIAA Paper No. 96-3250, Florida, July 1-3, 1996.

9. Greatrix, D.R., *"Numerical Study of Axial Motor Oscillation Effects on Solid Rocket Internal Ballistics,"* Canadian Aeronautics and Space Journal, Vol. 40, No. 4, December 1994, pp. 178-186.

10. Blomshield, F.S., and Beiter, C.A., *"Nonlinear Stability Testing and Pulsing of Full Scale Tactical Motors,"* 27th AIAA/ASME/SAE/ASEE Joint Propulsion Conference, AIAA Paper No. 91-1953, Sacramento, June 22-26, 1991.

11. Solanki, N., Greatrix, D.R., Gottlieb, J.J., *"Externally Generated Pressure Pulse in Rocket Chamber,"* Canadian Aeronautics and Space Journal, Vol. 47, No. 2, March 2001, pp. 345-355.

12. Solanki, N., Greatrix, D.R., and Gottlieb, J.J., *"External Pulse Effects on Solid Rocket Internal Ballistics,"* 36th AIAA/ASME/SAE/ASEE Joint Propulsion Conference, AIAA Paper No. 2000-3188, Huntsville, July 17-19, 2000.

13. Blomshield, F.S. and Stalnaker, R.A., *"Pulsed Motor Firing: Pulse Amplitude, Formulation, and Enhanced Instrumentation,"* 34th AIAA/ASME/SAE/ASEE Joint Propulsion Conference, AIAA Paper No. 98-3557, Cleveland, July 12-15, 1998.

14. Baum, J.D., Levine, J.N., and Lovine, R.L., *"Pulsed Instability in Rocket Motors: A Comparison Between Predictions and Experiments,"* Journal of Propulsion and Power, Vol. 4, No. 4, July-Aug., 1988, pp. 308-316.

15. Price, E.W., *"Review of Experimental Research on Combustion Instability of Solid Propellants,"* Progress in Astronautics & Aeronautics, Vol. 1, AIAA Publications, 1960.

16. Gottlieb, J.J., and Greatrix, D.R., *"Numerical Study of the Effects of Longitudinal Acceleration on Solid Rocket Motor Internal Ballistics,"* Journal of Fluids Engineering (ASME), Vol. 114, No. 3, September 1992, pp. 404-410.

17. *"Solid Propellant Selection and Characterization,"* National Aeronautics and Space Administration NASA SP-8064, Washington, D.C., 1971.

18. Harrje, D.T., *"Liquid Propellant Rocket Combustion Instability,"* National Aeronautics and Space Administration, NASA SP-194, Washington, D.C., 1972.

19. Brownlee, W.G., *"Nonlinear Axial Combustion Instability in Solid Propellant Motors,"* AIAA Journal, Vol. 2, No. 2, February 1964, pp. 275-284.

20. Greatrix, D.R., *"Axial Motor Vibration and Associated Internal Ballistics,"* 33rd AIAA/ASME/SAE/ASEE Joint Propulsion Conference, AIAA Paper No. 97-3337, Seattle, July 7-9, 1997.

21. Levine, J.D., and Baum, J.D., *"Modeling of Nonlinear Combustion Instability in Solid Propellant Rocket Motors,"* Nineteenth International Symposium on Combustion, pp. 769-776, 1982.

22. Greatrix, D.R., *"Transverse Vibration and Rocket Combustor Internal Ballistics,"* 33rd AIAA/ASME/SAE/ASEE Joint Propulsion Conference, AIAA Paper No. 97-3338, Seattle, July 7-9, 1997.

23. Yang, V., Brill, T.B., and Ren, W.Z. (ed.), *"Solid Propellant Chemistry, Combustion, and Motor Interior Ballistics,"* Progress in Astronautics and Aeronautics, Vol. 185, AIAA Publications, 2000.

24. Shafer, J.I., *Solid Rocket Propulsion*, John Wiley & Sons, Inc., New York, 1939.

25. Hugget, C., Bartley, C.E., and Mills, M.M., *Solid Propellant Rockets*, Princeton University Press, New Jersey, 1960.

26. Chopra, H.S., Greatrix, D.R., and Kawall, J.G., *"Transient Shock Wave Interaction with Rocket Nozzle–Cold-Flow Study"*, 39th AIAA/ASME/SAE/ASEE Joint Propulsion Conference, AIAA Paper No. 2003-4669, Huntsville, July 20-23, 2003.

27. Prevost, M., Godon, J.C., and Innegraeve, O., *"Thrust Oscillations in Reduced Scale Solid Rocket Motors – Part I: Experimental Investigations"*, 41st AIAA/ASME/SAE/ASEE Joint Propulsion Conference, AIAA Paper No. 2005-4003, Tucson, July 10-13, 2005.

28. French, J.C., *"Analytic Evaluation of a Tangential Mode Instability in a Solid Rocket Motor"*, 36th AIAA/ASME/SAE/ASEE Joint Propulsion Conference, AIAA Paper No. 2000-3698, Huntsville, July 16-19, 2000.

29. Ben-Dor, G., Igra, O., and Elperin, T., *Handbook of Shock Waves: Theoretical, Experimental, and Numerical Techniques,* Vol. 1, Academic Press, San Diego, 2001.

30. Glass, I.I., *"Shock Tubes,"* Proceedings of the Seventh International Shock Tube Symposium, pp. 751-759, 1969.

31. Anderson, J.D.Jr., *Fundamentals of Aerodynamics*, 3rd ed., McGraw-Hill Publishing Company, U.S.A., 2001.

32. Anderson, J.D.Jr., *Modern Compressible Flow with Historical Perspective*, 2nd ed., McGraw-Hill Publishing Company, U.S.A., 1990.

33. Emanuel, G., *Gasdynamics: Theory and Applications*, AIAA Education Series, New York, 1986.

34. Zucrow, M.J., Hoffman, J.D., *Gas Dynamics Volume 1,"* John Wiley & Sons, Inc., New York, 1976.

35. Liepmann, H.W., Roshko, A., *Elements of Gasdynamics,* John Wiley & Sons, Inc., New York, 1957.

36. John, J.E.A., *Gas Dynamics,* 2nd ed., ALLYN AND BACON, INC., Massachusetts, 1933.

37. *"Pressure Catalog,"* by Pressure and Force Sensors (PFS) Division, PCB PIEZOELECTRONICS Inc., Printed in U.S.A., 1998.

38. *"WaveBook User's Manual,"* by IOtech, Inc., Printed in U.S.A., 1999.

39. *"FLUENT User's Manual,"* by Fluent, Inc., Lebanon, 2001.

Appendix A

EXPERIMENTAL FIRING PROCEDURES

Laboratory Safety Considerations

While designing and conducting experimental analysis, safety is the most important issue; the equipment used should pose minimum risk to human health. In the present study, the independent variables of the overall system (i.e., the experimental apparatus) that may cause concerns are identified and discussed below. The basic safety requirements and rules that should be taken into considerations are as follows:

1. Various safety messages are posted at the entrance to the laboratory and at the location where the experiment is being conducted. Hence, it is advised to follow these instructions carefully before entering the laboratory or conducting the experiment, to avoid any damage to human health.
2. Around the experimental apparatus, a yellow and black caution line has been drawn. While conducting the experiment, one should stay behind this safety line. In other words, do not cross the yellow line.
3. The apparatus includes piping, fittings, couplings, small valves, etc., so due to high operating pressures and long, continuous operation of the apparatus, this may then lead to loosening of some joints. Hence, it may happen that some parts may fly off, although extra care had been taken during the assembly of the apparatus. Therefore, eye protection must be worn. If possible, head protection, like a workshop helmet, should also be worn.
4. As described in the shut down procedures, one should switch off all the lights in the laboratory and cut down the power supply to the equipment, so as to avoid any kind of short circuit or electrical damage to the apparatus. Short circuits may cause fire hazards.

Procedure 1:

Testing Procedure for Data Acquisition Equipment

Initially, before the data acquisition equipment was installed on the shock tube apparatus, it was tested in the Propulsion Research Facility (PRF at KHE-128A, Ryerson University) to gain familiarity with the use of the data acquisition system (i.e., WaveBook and the associated software, WaveView) and the process of saving the data. The testing proved to be useful; all the parameters to be inputted in the data acquisition software were known in advance. A step-by-step testing procedure is given below:

1. Turn "ON" the toggle valve connected to the compressed air supply.
2. Adjust the pressure regulator at some suitable value like 10 psig to achieve pressure calibration. One may turn the regulator in clockwise direction to increase the pressure and vice-versa.
3. Attach the pressure transducer to the air supply coming from the compressor.
4. Connect the transducer output to in-line charge amplifier.
5. Connect the output of charge amplifier to the input "XDRC" of sensor signal conditioner.
6. Connect the output to oscilloscope or high-speed data acquisition.
7. Turn "ON" the sensor signal conditioner.
8. Switch "ON" the computer.
9. Switch "ON" the WaveBook.
10. Double click the WaveView icon on the desktop.
11. The WaveView Configuration window appears which provides information about the various channels, etc.
12. In order to begin acquiring data with WaveView, turn "ON" only those channels that have signal connections (e.g., Channel 1).

    This can be done by:

    a. Double click on the channel's "ON/OFF" cell to select the proper status.

b. Click once on the channel's "ON/OFF" cell, then select "ON" or "OFF" from the list box above the spreadsheet. In our case, we have only one channel working, i.e., CH01.

13. Select the appropriate parameters for each channel.
14. Select Acquisition Configuration from the view pull down menu. When the acquisition configuration window is displayed, enter values for pre-trigger and post-trigger (scans or time periods) as desired. The time base for the acquisition can be set to frequency or period. The desired trigger source and parameters are selected in the trigger selection box.

The various set-up values for the acquisition configuration window are as follows:

DURATION:

1. Pre-trigger: 5 Scans
2. Post-trigger: 10,000 Scans
3. Convection: Scans

RATE:

1. Internal
2. Pre-trigger: 20 kHz
3. Post-trigger: 500 kHz
4. Convection: Frequency

TRIGGERING TYPE: Channel 1 Analog

EDGE: Rising

THRESHOLD: 0.1 V

15. Make sure that all the acquisition configuration settings are correct.
16. Click on "SCOPE" located in the menu bar. A WaveView scope window appears which enables to read data from WaveBook.

17. The initial readings that appear on the WaveView scope window are as follows:
    a. Status: Idle
    b. Scans: 0 / 0 % Complete
    c. Scans in View: 10
    d. Pre-trigger Time Base: 25.000 ms/div
    e. Post-trigger Time Base: 1.000 ms/div
18. Click the arm button (Green colour) from the Menu Bar.

    Now, the scope window reads:
    a. Status: Waiting for Trigger
    b. Scans: 5 / 0% Complete
    c. Scans in View: 0
19. After clicking the arm, look at the status. It should read "WAITING FOR TRIGGER". At this time supply a manual trigger from air supply.

    Now, the scope window reads:
    a. Status: Idle
    b. Scans: 10,005 / 100% Complete
    c. Scans in view: 10,000
    d. Pre-trigger Time Base: 25.000 ms/div
    e. Post-trigger Time Base: 1.000 ms/div
20. After a manual trigger is given, a waveform appears in the WaveView scope window.
21. Save this waveform by clicking on the File Menu, then click on "SAVE DATA FILES AS". A dialog box will open asking for the filename. Give any filename with ". TXT" as an extension. Click "OK".

    For e.g.: TEST.txt
22. Exit WaveView by clicking on "EXIT" in the File Menu.
23. Switch "OFF" the WaveBook.
24. The saved file will be stored in:

    C:\Program Files\DaqX\Applications\ASCII
25. Open the file in "Microsoft Excel".
26. Select only the pressure and time values that appear in the spreadsheet.

27. Copy the selected values from the Excel spreadsheet.
28. Open the SigmaPlot program and paste those values into the SigmaPlot's spreadsheet.
29. Use Quick Transform to adjust data (if necessary).
30. Click on the Chart Wizard button in the Menu Bar.
31. Select a suitable chart type, which best depicts the nature of your graph. After selecting the chart type, press and hold to view the preview of the graph. If found satisfactory then click on next or choose some other type of chart. Click "NEXT".
32. Provide a title, gridlines, legend, etc. to your graph.
33. Export the graph as a JPEG picture.
34. Save the spreadsheet along with the graph at a desired location and close SigmaPlot and Excel.
35. Switch "OFF" your computer.

Procedure 2:

Procedure for Determining Conversion Factor

This procedure is carried out to determine a conversion factor that allows converting the voltage reading obtained from the data acquisition system to a pressure reading (in Pa). The equipment consists of a pressure transducer, a sensor signal conditioner, an in-line charge amplifier, a data acquisition system (i.e., WaveBook), and a computer.

1. Using quick-release connectors, a pressure gauge and a push-button valve (i.e., toggle valve) are connected to the air reservoir tank.
2. Pressure transducer, sensor signal conditioner, and WaveBook are connected to the air supply from the compressor through a push-button valve. Ensure that the sensor signal conditioner gain is set to 1 so as to minimize the noise.
3. Switch "ON" the compressor.
4. WaveBook is initialized by setting the pre-trigger to 100 readings/scans and the post-trigger to 9900 readings/scans. The triggering voltage is set at 0.002 mV.

5. The push-button valve is pressed to supply a trigger (i.e., a short burst of air to escape from the reservoir) at different pressures ranging from maximum of 100 psig to minimum of 10 psig.
6. Each time, a graph is plotted from the collected data, and the mean measured voltage is recorded.
7. Another graph of voltage versus pressure is plotted. A best-fitting line approach is used to find an equation representing these points. This is used to obtain a conversion factor, which allows the measurements in mV to be converted to Pa.
8. Another measurement is taken, but this time the factor found in the previous measurement is used to produce the reading in psig.
9. If the reading produced the same pressure that is displayed on the pressure gauge attached to the air reservoir, then this conversion factor is recorded. If the factor is slightly off, an adjustment in the factor is done and another trial is conducted to ensure its accuracy.
10. Step 8 is repeated for as many times as needed to determine an accurate conversion factor.
11. Steps 3-9 are repeated for different pressure values (as stated in step 5) at decreasing intervals of 10 000 Pa.
12. The final conversion factors are recorded and graphed.

Procedure 3:

Preliminary Test Procedure

Before conducting actual experimental firings, a preliminary test is performed to check for air leakage through pipe, coupling, and fittings and to verify proper mechanical working of the apparatus. This particular test is conducted without a diaphragm (i.e., the diaphragm holder is empty) and in the absence of data acquisition equipment. The procedure for such a test is given below. While conducting the test, one should make sure that all the safety requirements are met and safety gear is worn.

1. Open the water tap so that water is filled in the cooling jacket of the compressor.

2. Switch "ON" the compressor by shifting the red switch located on the switchboard to "AUTO" position.
3. Make sure that the isolation ball valve is closed so that high-pressure air does not pass through the shock tube. Once, the maximum pressure in the reservoir tank is attained, the compressor will automatically shut down.
4. Open the air supply to the driver and driven chamber and check for air leakages; if any are found, try to eliminate them.
5. Check that there is no water or there are no dust particles in the separator, as moisture in the air might get condensed. Take out the water by opening the valve at the bottom of the separator. Don't forget to close this valve.
6. Pass some air through the shock tube so that there are no dust particles in the shock tube.

Procedure 4:

Procedure for Connecting the Pressure Transducer with the Shock Tube and the Data Acquisition System

1. Place the transducer in the pressure transducer tap and snug it (with extra care) with the help of a wrench. One should not apply excess pressure while tightening the transducer. Make sure that the transducer is mounted properly.
2. Connect one end of the co-axial cable along with the charge amplifier to the transducer mounted on the shock tube and the other end to the sensor signal conditioner (Model No.: 480E09). This end is connected to a socket named as "XDCR" on the Signal Conditioner.
3. Adjust the gain of the sensor signal conditioner to 1. This completes the connection of the transducer with the shock tube.
4. The data acquisition system (i.e., WaveBook) provides a number of channels so that number of devices can be connected to collect data. For the present experimentation, only sensor signal conditioner is connected to the system. Another co-axial cable is used to connect "CH1–ANALOG TRIGGER" of the

system with "SCOPE" on the sensor signal conditioner. This completes the connection of the WaveBook with the sensor signal conditioner.

5. After all the connections are done, one should make sure that the battery in the sensor signal conditioner is charged, otherwise replace the battery. This can be done by shifting or pressing the red switch on the sensor signal conditioner to the "BATT TEST". As soon as the switch is pressed, the needle should move to the yellow region, which indicates that the battery is "OK" or has enough power. Within few seconds, the needle will automatically move to the green region, which indicates that the sensor signal conditioner is ready for use.
6. Once the data are being collected, switch "OFF" the red button on the sensor signal conditioner.

Procedure 5:

Procedure for Connecting the Data Acquisition System with the Computer

1. Place the data acquisition system (i.e., WaveBook) in a convenient position near the computer so that the connections with the computer can be done easily.
2. Connect the WaveBook to the required parallel port of the CPU with the help of a communication cable supplied with the WaveBook. The other end is connected to the WaveBook in the socket named as "TO COMPUTER".
3. Power supply is given to the WaveBook with the help of an adapter, which is connected to the socket named as "POWER IN". The power that can be supplied to the WaveBook is in the range of +10 V D.C. to +30 V D.C. This completes the connection of WaveBook with the computer. The details of the adapter are:
    a) Company Name: GlobTek Inc.
    b) Serial No.: TR9CG2700N05-A1.
    c) Model No.: AD-740U-1150.
    d) Input: 100 V-240 V, 1 A, 50-60 Hz.
    e) Output: 15 V, 2.7 A.

Procedure 6:

Procedure for Initializing the Data Acquisition System

Once all the connections are done for the data acquisition equipment, it is necessary to initialize the data acquisition system (i.e., WaveBook) so as to collect the data.

1. Position the Data Acquisition equipment in such a way that the user has an unobstructed view of the monitor.
2. Switch "ON" the computer.
3. Once the computer is switched ON, then switch "ON" the WaveBook by pressing the black power switch to position "1" (provided at the back of the WaveBook).
4. Double click the WaveView icon on the desktop of the computer so that the data acquisition software (i.e., WaveView) is started and one can see a window titled as WAVEVIEW.CFG (WaveBook 0) having information about the number of channels in the channel configuration frame.
5. Click on the Edit Menu. Select the suitable options like Show All Channels, Hide Inactive Channels, etc.
6. Click on the View Menu. Set the Acquisition and Module Configuration separately. Both of the configuration set-ups are described in detail in the procedure 1.
7. Click on the System Menu. Click on the Select Device, after clicking a Select Device dialog box will be opened. Make sure you select the WaveBook 0 option otherwise the software will run in the Simulated Device mode and will not capture data. After selecting WaveBook 0, click "OK".
8. At this stage, all the settings in the software have been done. The system is ready for collecting the data.
9. Open the Scope window. Click the Arm (green arrow in the Menu Bar). After 5 scans, perform the actual experimental firing.
10. Save the data.
11. Click the cross button in the upper right corner so as to close the Scope window.
12. Exit the data acquisition software by clicking Exit in the File Menu.

Procedure 7:

Actual Firing Procedure

Once the preliminary test is carried out, connect the data acquisition equipment to the shock tube. In this test, place a diaphragm in the diaphragm holder. Again all the safety requirements should be met and the safety gear must be worn. Steps listed below must be followed to obtain results from the apparatus.

1. Open the water tap so that water is filled in the cooling jacket of the compressor.
2. Switch "ON" the compressor by shifting the red switch located on the switchboard to "AUTO" position.
3. Make sure that the isolation ball valve is closed. Once, the maximum pressure is attained in the air reservoir tank, the compressor will automatically shut down.
4. Load the diaphragm and set-up the desired head-end gap geometry (as firings are conducted with different head-end gap widths) at the end of the driven chamber, make sure all the pressure gauges and thermocouples are mounted properly, and the data acquisition system is initialized to capture the data.
5. Open the air supply to the driven (primary) chamber and add air until the desired pressure level is attained (as firings are conducted at 375 kPa for the reference case and 250 kPa for the double diaphragm case).
6. Simultaneously, pressurize the driver (secondary) chamber and note the pressure from the pressure gauge at which the diaphragm is ruptured.
7. As soon as the diaphragm is ruptured, one should get a number of peaks in the scope window of WaveView (i.e., data acquisition software). This means that data have been collected. One has to verify whether the data is correct or not.
8. Save the data.
9. If some more experiments are to be conducted then place a new diaphragm in the holder and repeat steps 5 to 8.
10. Once all the firings are conducted, follow the shutdown procedure.

Procedure 8:

Shutdown Procedure

After performing the actual experimental firing, shut down procedure should be followed as a part of safety requirement.

1. As soon as the diaphragm is ruptured, cut-off the air supply to the (driven) primary and (driver) secondary pressure chambers by closing the respective valves.
2. Switch "OFF" the compressor. Close the running water supply to the cooling jacket of the compressor.
3. Shutdown the power of WaveBook. Shutdown the computer.
4. Disconnect the transducer from the WaveBook and the shock tube. Switch "OFF" the sensor signal conditioner. Keep the transducer in a safe place so as to avoid any damage.
5. Remove the ruptured diaphragm from the diaphragm holder.
6. Gather all the tools used while conducting the experiment and keep them in the toolbox. If necessary, one should clean the tools.
7. Make sure all the electrical plugs, and switches are disconnected.
8. Clean the place near the apparatus.
9. Switch "OFF" the lights in the laboratory where the experiment was conducted.
10. Lock and shut the door while leaving the laboratory.

Appendix B PARTS LIST FOR EXPERIMENT

Part Name	Manufacturer	Model Number	Serial Number	Range
Pressure Gauges: *On driven chamber* *On driver chamber* *On reservoir tank*	 Wika Wika Weksler Inc.		 8032 435 2089	 0-100 psig 0-200 psig 0-300 psig
Reservoir Tank:	Ferro Metal Ltd.	QM-40-12C	6995	Max Pres. 170 psig
2-Stage Compressor:	Ingersol Rand	15TX type 30	18520	48 cu. ft.
Regulator:	Schrader Bellows		3566-2000	5-125 psig
Filter:	Schrader Bellows		3536-1000	Max Pres. 150 psig
Diaphragm:				Polyester film having thickness of 0.0000889 m
Diaphragm Holder:	Pro-Quip			Diameter of 0.0508 m
Nozzle:				0.0508mX0.007870mX0.0203m
Pressure Transducer	PCB PIEZOELEC-TRONICS Inc.	112A02	17993	0-1000 psig
Charge Amplifier	PCB	422 D02	6245	
Sensor Signal Conditioner	PCB	480 E09	24568	
DAQ System	IOtech	Wavebook/516	201727	
DAQ Software	IOtech	WaveView V7.8.104		
Thermocouple:	Decktronic	10-K1		

Appendix C STARTING FLUENT ON A UNIX SYSTEM

The numerical simulations are generated on Sun Microsystems computer machines installed in the Aerospace Computational Laboratory (i.e., ATOP/ACL Lab at Ryerson University). These machines consist of fast processors having sufficient memory for conducting CFD analysis, and run on UNIX Operating System. FLUENT Version 6.1 is pre-installed on these machines.

The following section describes how to start FLUENT on a UNIX system and also provides a step-by-step procedure of how to select various menus given in FLUENT to run a simulation.

One has to supply a login name and password (provided by network administrator at the ATOP Lab) to use any of the computer machines in the ATOP Lab. Once login name and password is provided, open a terminal window so that commands can be executed at the command line of the terminal window. There are several ways to start FLUENT on a UNIX Operating System:

1. Start FLUENT by supplying the appropriate version at the command line.
2. Start the solver from the command line without specifying a version, and then use the "Select Solver panel" to choose the appropriate version.
3. Start the solver from the command line without specifying a version, and then read a case file (or a case file and data file) to start the appropriate version.

Among the various ways, the simplest way to start FLUENT is by providing the appropriate version at the command line. FLUENT consists of single-precision and double-precision solvers. Along with it one can define the dimensionality, i.e., 2D and 3D of the problem. In order to generate simulations for the present case, "FLUENT 2d" command is executed at the command line. This command runs a 2-dimensional, single-precision solver. After initializing the solver, read the grid/mesh file in FLUENT and apply the various input parameters (discussed in Chapter 3).

A step-by-step procedure is prepared which describes the various menus used to input various parameters and solve a problem.

1. Read the grid/mesh file.

   File→Read→Case

2. Check the grid and grid scale.

   Grid→Check

   Grid→Scale

   Display→Grid

3. Define units for the problem.

   Define→Units

4. Define the various models used to solve the problem.

   Define→Models→Solver

   Define→Models→Viscous

   Define→Models→Energy

5. Define physical properties of materials and operating conditions.

   Define→Materials

   Define→Operating Conditions

6. Define boundary conditions.

   Define→Boundary Conditions

7. Define custom field functions to apply specific values to different regions/zones defined in the geometry.

   Define→Custom Field Function

8. Provide controlling parameters for solution.

   Solve→Controls→Solution

9. Initialize the solution.

   Solve→Initialize→Initialize

10. Patch custom field functions.

    Solve→Initialize→Patch

11. Plot residuals.

    Solve→Monitors→Residual

12. Create surface points to collect static pressure.

    Surface→Point

13. Define surface monitors.

    Solve→Monitors→Surface

14. Save the input file.

    File→Write→Case and Data

15. Iterate the solution.

    Solve→Iterate

16. Save the solution.

    File→Write→Data

17. Displaying the solution.

    Display→Contours

    Display→Velocity Vectors

    Plot→XY Plot

18. After saving the input and output files, exit/close the solver.

    File→Exit

19. Once the simulation is completed, close the terminal window and don't forget to logout.

Appendix D INPUT CONDITIONS FOR FLUENT

Boundary conditions:

The various boundary conditions discussed in Chapter 3 are listed below:

1. **DIAPHRAGM** ("right-half tube" model, used only to identify the optimum grid density for the subsequent main series of simulations to be completed for a full shock tube model)

   Boundary Type: mass-flow-inlet

   Mass flow Specification Method: mass flow rate

   Mass flow rate: 1.2 kg/s

   Total Temperature: 307.86 K (to reproduce the incident shock wave parameters)

   Supersonic/Initial gauge pressure: 557 625 Pa

   Direction Specification Method: Direction Vector

   Axial-Component of flow direction: 1

   Radial-Component of flow direction: 0

   Turbulence Specification Method: Intensity & Viscosity Ratio

   Turbulence Intensity (%): 5 (common value for fully-developed, internal flow)

   Turbulence Viscosity: 2

2. **WALL** (used for all solid boundary surfaces, excepting the diaphragm after rupture – in that case, set to Internal Boundary Type)

   Thermal Condition: Heat flux

   Heat flux: 0 W/m^2

   Wall thickness: 0

   Heat Generation Rate: 0

   Roughness Height: 0.0001 m

   Roughness Constant: 0.5

Custom field functions:

The various custom field functions applied to different regions in the model flow geometry are listed below:

1. **For Driver Region:**

   p_0 = 850 000 Pa

   u_0 = 0 m/s

   T_0 = 294 K

2. **For Driven and Head End Region:**

   p_1 = 375 000 Pa

   u_1 = 0 m/s

   T_1 = 294 K

Solution Control Parameters:

1. **Under-Relaxation Factors:**

   Solid: 1

   Turbulence Kinetic Energy: 0.8

   Turbulence Dissipation Rate: 0.8

   Viscosity: 1

2. **Discretization:**

   Flow: Second Order Upwind

   Turbulence Kinetic Energy: Second Order Upwind

   Turbulence Dissipation Rate: Second Order Upwind

3. **Solve Parameters:**

   Courant number: 0.75

Variables to be monitored and checked for convergence:

1. Normalization Scheme: Scaled Residuals
2. Print and Plot residuals
3. Continuity: Monitoring, check for convergence with criteria of 0.001
4. X-Velocity: Monitoring, check for convergence with criteria of 0.001
5. Y-Velocity: Monitoring, check for convergence with criteria of 0.001
6. Energy: Monitoring, check for convergence with criteria of 0.001
7. Thermal Conductivity: Monitoring, check for convergence with criteria of 0.001
8. Epsilon: Monitoring, check for convergence with criteria of 0.001

Appendix E RESULTS SUMMARY

The summary of various results discussed in Chapter 4 is provided in Table E.1. One should note that the gap dimensions are given in the "depth x width" format, in centimetres. All pressure values are in kPa, while the frequency is given in kHz. The last column of the table represents the figure number corresponding to the pressure-time profile.

Table E.1. Results Summary

Gap Geometry (depth x width)	Monitor location	p_1 (kPa)	p_4 (kPa)	Pressure Spike (kPa)	Frequency (kHz)	Figure number
1 x 1	10 cm @ wall	375	850	+40	8.9	4.2
1 x 1	5 cm @ wall	375	850	+50	8.8	4.3
1 x 1	15 cm @ wall	375	850	+30	9.5	4.4
1 x 1	10 cm @ centre axis	375	850	+85	8.5	4.5
1 x 1	5 cm @ centre axis	375	850	+140	9.2	4.6
1 x 1	15 cm @ centre axis	375	850	+50	8.1	4.7
0 x 0	All locations	375	850	0	0	4.17
1 x 0.5	10 cm @ wall	375	850	+50	9	4.21
1 x 0.5	10 cm @ centre axis	375	850	+95	8.7	4.22
1 x 0.5	5 cm @ centre axis	375	850	+120	9	4.23
1 x 0.5	15 cm @ centre axis	375	850	+60	8.2	4.24
1 x 1.5	10 cm @ wall	375	850	+15	8.1	4.25
1 x 1.5	5 cm @ centre axis	375	850	+80	8.5	4.26
1 x 1.5	10 cm @ centre axis	375	850	+30	8.8	4.27
1 x 1.5	15 cm @ centre axis	375	850	+15	9.2	4.28
1 x 3	10 cm @ wall	375	850	-90	9.5	4.29
1 x 3	5 cm @ centre axis	375	850	-65	9	4.30
1 x 3	10 cm @ centre axis	375	850	-50	9.3	4.31
1 x 3	15 cm @ centre axis	375	850	-90	9.9	4.32
0.5 x 1	10 cm @ wall	375	850	+25	9.2	4.33
0.5 x 1	5 cm @ centre axis	375	850	+90	9	4.34

Gap Geometry (depth x width)	Monitor location	p_1 (kPa)	p_4 (kPa)	Pressure Spike (kPa)	Frequency (kHz)	Figure number
0.5 x 1	10 cm @ centre axis	375	850	+40	8.5	4.35
0.5 x 1	15 cm @ centre axis	375	850	+25	8.5	4.36
3 x 1	10 cm @ wall	375	850	+25	8.4	4.37
3 x 1	5 cm @ centre axis	375	850	+100	8.7	4.38
3 x 1	10 cm @ centre axis	375	850	+40	9.1	4.39
3 x 1	15 cm @ centre axis	375	850	+15	9.3	4.40
0.5 x 0.5	10 cm @ wall	375	850	+25	9	4.41
0.5 x 0.5	5 cm @ centre axis	375	850	+60	9.3	4.42
0.5 x 0.5	10 cm @ centre axis	375	850	+55	9.7	4.43
0.5 x 0.5	15 cm @ centre axis	375	850	+30	9.9	4.44
3 x 2	10 cm @ wall	375	850	-85	8.1	4.45
3 x 2	10 cm @ centre axis	375	850	-90	8.5	4.46
3 x 2	5 cm @ centre axis	375	850	-40	8.8	4.47
3 x 3	10 cm @ wall	375	850	-160	8.4	4.48
3 x 3	10 @ centre axis	375	850	-155	8.6	4.49
1 x 1	5 cm @ centre axis	375	1150	+240	8.4	4.51
1 x 1	10 cm @ centre axis	375	1150	+120	8.9	4.52
1 x 1	5 cm @ centre axis	375	1350	+380	8.7	4.53
1 x 1	10 cm @ centre axis	375	1350	+185	8.8	4.54
1 x 1	5 cm @ centre axis	375	2000	+550	8.6	4.55
1 x 1	10 cm @ centre axis	375	2000	+250	8.9	4.56
1 x 1	5 cm @ centre axis	375	3000	+650	8.9	4.57
1 x 1	10 cm @ centre axis	375	3000	+250	8.5	4.58